Performance Improvement and Applications of Biomimetic Electrically Small Antenna Arrays

By

Mohammad Ranjbarnikkhah

A dissertation submitted in partial fulfillment of

the requirements for the degree of

Doctor of Philosophy

(Electrical Engineering)

at the

UNIVERSITY OF WISCONSIN-MADISON

2019

Date of final oral examination: 10/09/2019

The dissertation is approved by the following members of the Final Oral Committee:

Nader Behdad, Professor, Electrical and Computer Engineering

Susan C. Hagness, Professor, Electrical and Computer Engineering

Hongrui Jiang, Professor, Electrical and Computer Engineering

Alan McMillan, Assistant Professor, Department of Radiology and Medical Physics

Acknowledgements

I would like to express my deepest gratitude to my advisor, Professor Nader Behdad, for his strong support and invaluable guidance in my PhD life. He provided me opportunities and challenges to pursue my passion in research that I love.

I would like to thank Prof. Susan C. Hagness, Prof. Hongrui Jiang, and Prof. Alan McMillan for their support and advice as my dissertation committee members.

I would like to thank my colleagues and my friends at University of Wisconsin-Madison, Dr. Amin Momeni, Dr. Kasra Ghaemi, Dr. Yahya Mohtashami, Dr. Elham Mohammadi, Dr. Amirhossein Davoody, Dr. Hung Luyen, Dr. Kai Ren, Dr. Mirhamed Mirmozafari, Sirous Nourgostar, Alireza Shahsafi and Ruyu Ma for their kind support during the past few years.

Last but not least, I would like to thank my family, my wife and my daughter, Nafiseh and Zahra, for their never ending encouragement.

Abstract

Recently a class of biologically-inspired electrically-small antenna arrays have been reported. Referred to as biomimetic antenna arrays (BMAAs), these antennas mimic the hyperacute senses of directional hearing of small animals. First we present a two-element tunable biomimetic antenna array (BMAA) that uses a single varactor to achieve tunability over a relatively wide band. The ECN is designed to allow for tuning the response of the BMAA. Over this frequency range, the proposed BMAA can enhance the phase difference between the output signals compared to a conventional array while extracting the maximum available power from the incoming wave. Then, we present a three-element biomimetic antenna array (BMAA) with an electrically-small triangular lattice. The proposed array consists of three identical quarter-wavelength-long monopoles each positioned at a corner of an equilateral triangle. It will allow for resolving ambiguities problem when such BMAAs are used in small-aperture direction finding systems. The three strongly-coupled antennas are connected to an external coupling network with three inputs and three outputs. This network augments the mutual coupling between the strongly-coupled antennas and is designed to maximize the output phase difference between each two antenna elements without sacrificing the output power level of the array compared to a conventional array occupying the same aperture. Then, we present the performance of multi-input-multi-output (MIMO) communications systems that exploit biomimetic antenna arrays (BMAAs) with electrically-small aperture dimensions. By exploiting the mutual coupling between closely-spaced radiating

elements and extracting the maximum available power from all excitation modes of the array, BMAAs can significantly outperform conventional antenna arrays with similar aperture sizes. The capacity of MIMO systems using such BMAAs are compared with those that use conventional antenna arrays with the same element types and spacing. Finally we present a design strategy for platform-based antennas operating on electrically-small platforms such as unmanned ground vehicles (UGVs). Specifically, we report the design of a platform-based antenna operating at the lower end of the VHF band for an electrically small UGV. The antenna is mounted on the bottom of the platform resulting in an extremely low profile design and generating vertically-polarized, monopole-like radiation patterns. The design of this low-profile antenna is extended to a two-element antenna array mounted on the same platform and the performance of this array as part of a two-element direction-finding system was investigated through computer simulations.

Contents

List of Figures

List of Tables

Chapter 1

Introduction and Background

1.1 Motivation

Over the past few decades, a significant body of research has been devoted to examining compact and electrically-small antenna arrays. Generally, these arrays are used in low-frequency applications where the electromagnetic wavelength is very large or in applications where sufficient space is not available to accommodate a large array aperture. One application that uses such arrays is small-aperture direction finding systems operating at the HF, VHF, or UHF parts of the electromagnetic spectrum. Recently, biomimetic antenna arrays (BMAAs) that mimic the hyperacute auditory system of the parasitoid fly Ormia Ochracea were reported as a promising means of increasing the sensitivity of a small-aperture direction finding system. While the first designs of BMAAs provided higher angular sensitivities compared to conventional arrays with the same aperture sizes, this capability was achieved at the expense of sacrificing the output power of the antenna. Then, a new coupled antenna array topology was proposed that could achieve a moderate output phase sensitivity without sacrificing the available power of the array. This array provided the maximum, theoretically-achievable phase sensitivity while extracting the maximum power available from the array. All of these designs, however, demonstrate the enhanced phase sensitivity and angular resolutions over very narrow bandwidths.

Precise direction of arrival (DoA) estimation of an electromagnetic wave is essential for many commercial and military applications. Over the past few decades, a significant body of research has been conducted in this area. However, most of the reported structures use electrically-large antenna apertures, which makes them not suitable for applications that do not have sufficient area to accommodate such arrays. Recently, biomimetic antenna arrays (BMAAs) that mimic the hyperacute hearing characteristics of the parasitoid fly Ormia Ochracea were reported as a possible means of miniaturizing the aperture size of an accurate direction finding system. BMAAs use an external-passive coupling network, which significantly enhances the phase difference between the output signals of the array compared

to those received at the antenna terminals. A linear, three-element BMAA was reported. In this design, however, the phase enhancement obtained between the outer elements of the array is obtained at the price of sacrificing the output power levels of these two elements. So far, most of the BMAAs reported in the literature have used either two elements or three elements located along a linear baseline. Therefore, when used in direction finding applications, such arrays will have a 180 degrees ambiguity in detecting the direction of arrival of the wave. Additionally, most of these arrays do not extract the maximum available power from an incoming electromagnetic wave. Therefore, a new technique for designing multi-element BMAAs that are not located on a single, linear baseline is required.

Precise direction of arrival (DoA) estimation of an electromagnetic wave has many commercial and military applications including collaborative localization of autonomous agents and tracking of dismounted soldiers. In many HF/VHF direction-finding systems, antennas are mounted on vehicular platforms and the platform is a part of the antenna, whether intentional or not. Recently, various research groups have investigated platform-mounted antennas and proposed different techniques that exploit the presence of the large metallic platform to enhance the performance of such antennas. In one approach, the natural resonant modes of the platform were excited using electrically-small antennas to improve the overall bandwidth of an otherwise narrowband HF antenna. However, in this and most previous platform-based antennas, the underlying platform was an electrically large structure at the frequency of operation.

1.2 Literature Review on Electrically Small Antenna Arrays

1.2.1 Superdirectivity

Small antenna arrays have been investigated for more than 70 years. Early research in this field examined the concept of superdirectivity in arrays with electrically-small spacing between the antenna elements [1]- [3]. These research demonstrated that achieving superdirectivity is possible in theory, however implementing the superdirectivity in practice is challenging due to the precision with which excitation coefficient of the array must be synthesized, the strong mutual coupling between adjacent elements, and the losses in the feed network. In other words, superdirective antennas can not be realized as supergaion antennas. Then, other research investigated different attributes of superdirective arrays including the bandwidth and loss issues in such arrays [4], the use of active elements to increase the bandwidth [5], and innovative superdirective array designs [6]. The impact of mutual coupling between the closely-spaced elements of electrically-small arrays have also been extensively investigated [7]- [8]. In [9]- [12], techniques for compensating the mutual coupling effects in such arrays were proposed including orthogonal eigenmode method [9], multiple input multiple output antenna decoupling networks [10], and wideband decoupling of coupled closely-spaced antenna arrays using resistive lossy elements.

1.2.2 Small-aperture direction finding

Small-aperture direction finding is another application where electrically-small antennas or antenna arrays have been used [13]- [14]. Partly motivated by the requirements of this application, recently a class of biologically-inspired electrically-small antenna arrays have been reported [15]- [16]. Referred to as biomimetic antenna arrays (BMAAs), these antennas mimic the hyperacute senses of directional hearing of small animals [17]. A BMAA consists

of a number of closely-spaced receiving antenna elements coupled together using an external coupling network (ECN). The role of the ECN is to convert the small phase differences between the received signals at its input (antenna terminals) to larger phase differences at its outputs. In the biological systems that BMAAs mimic, this phase enhancing capability is the main mechanism that allows the small animals to perform precise direction finding using an acoustically-small receiving aperture [18]. In [15]- [16], two-element BMAAs that directly mimic the sense of auditory hearing a parasitoid fly were introduced. This concept was later expanded to a three-element BMAA with a linear baseline [19]. More recently, a two-element BMAA was reported, which uses a non-Foster external coupling network to increase the antenna's operating bandwidth [20]. While these antennas achieve a phase enhancement capability, they do this at the expense of sacrificing the available output power level of the array compared to a conventional array. This is a major drawback, since reduction of the output power level reduces the output signal-to-noise ratio of the array in situations where the primary noise source is that of the receiver. In [21], it was theoretically and experimentally demonstrated that in a two-element BMAA, an upper bound for the maximum phase enhancement factor exists that can be achieved without sacrificing the output power level of the array compared to a conventional array.

1.2.3 MIMO Communication systems

Beamforming using directional antenna arrays can improve the capacity of multi-input multi-output (MIMO) communication systems by increasing the gain and reducing the cross correlation of wireless channel links. However, the performance of conventional antenna arrays is limited by the physical dimensions of the array elements, especially when the element spacing is reduced below $\lambda_0/2$, where λ_0 is the free-space wavelength. It is well known that for a beamformer to provide an acceptable spatial filtering, the antenna spacing should be in the order of $\lambda_0/2$ [22, 23]. The reliance on large antenna spacing results in large array sizes, especially at frequencies below 5 GHz where the propagation conditions are most suit-

able for achieving wide-area coverage that many mobile wireless communication systems rely on. Over the years, a number of studies have examined the performance of MIMO systems that use electrically-small or compact antenna arrays at the transmitter and/or the receiver [24, 25]. The impact of antenna correlation in small receiving terminals on the capacity of MIMO systems is studied theoretically and experimentally [24]. The theory of characteristic modes has been used to design MIMO antennas that exploit the resonant modes of the platform to obtain different radiation patterns [25]. A reconfigurable antenna array based on electronically-steerable parasitic array radiator technique was used in [26] to increase the MIMO channel capacity of the conventional array. Eventually, a number of theoretical studies have examined the role that superdirectivity can play in enhancing the capacity of MIMO systems employing superdirective antenna arrays [27–29]. In [12], a matrix method was reported to compensate the mutual coupling effects on array radiation patterns utilizing a modification matrix obtained from measured element patterns. The application of electrically-small antenna arrays in two-element MIMO system is examined in [30]. Mode-based methods for beam-forming in such arrays are also examined in [31].

1.3 Thesis overview

1.3.1 Chapter 2: An Electronically Tunable Biomimetic Antenna Array

In this chapter, a two-element biomimetic antenna array, which is tunable over a wide frequency band is presented. To achieve this wideband tunability, a new coupling network for this tunable-BMAA is proposed. The device uses a tunable external coupling network, capable of tuning to different frequencies over the frequency range of 580-700 MHz. Using an equivalent-circuit model, a comprehensive synthesis procedure is developed that allows for designing and optimizing the proposed antenna. A prototype of the proposed tunable

BMAA is also designed. The array consists of two identical elements separated from each other by 0.050 and the coupling network is a four-port passive external network that uses a single varactor to achieve tunability. The antenna prototype is fabricated and experimentally characterized. The measurement results show that the proposed BMAA can achieve a phase enhancement factor in the range of 1.8-2.1 over the frequency band of 580-700 MHz. This phase enhancement factor is achieved without sacrificing the available output power of the antenna array. The proposed BMAA can potentially be beneficial in applications such as small-aperture direction finding and radar systems.

1.3.2 Chapter 3: A Three-Element Biomimetic Antenna Array with an Electrically-Small Triangular Lattice

In this chapter, we present a three-element biomimetic antenna array architecture designed based on decomposing the incoming wave received by the antennas to three linearly-independent orthogonal modes. In this architecture, the antenna elements are placed on three corners of an equilateral triangle and are connected to each other through a symmetric external coupling network. Similar to the other BMAA designs, the estimation of the DoA is achieved by enhancing the phases of the incoming waves at the output of the external coupling network. In sharp contrast with the previous works, however, each element of the proposed array extracts the maximum available power from the incoming EM wave. A prototype of this system consisting of three quarter wavelength monopole antennas operating at 600 MHz and separated from each other by 0.05 is designed, fabricated, and characterized. Details of the design procedure and experimental measurement results of the proposed antenna array will be discussed and presented at the chapter 3.

1.3.3 Chapter 4: Capacity-Enhancement in MIMO Systems Using Biomimetic Electrically-Small Antenna Arrays

In this chapter, we investigate the performance of multi-input-multi-output (MIMO) communications systems that exploit biomimetic antenna arrays (BMAAs) with electrically-small aperture dimensions. By exploiting the mutual coupling between closely-spaced radiating elements and extracting the maximum available power from all excitation modes of the array, BMAAs can significantly outperform conventional antenna arrays with similar aperture sizes. As a proof of concept demonstration, we examine the use of two-element BMAAs consisting of two $\lambda/4$ monopole antennas with variable element spacing in a MIMO system. The capacity of MIMO systems using such BMAAs are compared with those that use conventional antenna arrays with the same element types and spacing. Our simulation results demonstrate that using BMAAs can offer considerable capacity enhancements in a MIMO system. To experimentally verify these results, a prototype of a two-element BMAA operating at 615 MHz with element spacing of $\lambda/10$ and a regular array prototype with similar antenna elements and dimensions are fabricated and characterized. The performance of MIMO systems using these two antennas are modeled using numerical channel modeling using the measured antenna responses. These results are found to be in good agreement with theoretical predictions and quantify the capacity enhancements that two-element BMAAs can provide in a MIMO communication system.

1.3.4 Chapter 5: Electrically-Small Platform-Based Antennas for an Unmanned Ground Vehicle

In this chapter, we investigate the applicability of this concept for platform-based antennas that operate on electrically-small platforms such as small unmanned ground vehicles (UGVs) operating at the VHF band. Specifically, we report the design of platform-based antennas operating at the lower end of the VHF band for a small UGV (0.13 x 0.09* x 0.05 at 40 MHz).

We use the characteristic mode theory (CMT) to evaluate the performance of two different antennas designed for operation on this platform. Using CMT, performance metrics of the antennas including the maximum antenna bandwidth and its radiation characteristics can be investigated. Both antennas are designed to generate vertically-polarized, monopole-like radiation patterns. The performances of these antennas when operating in a realistic operational environment are simulated using numerical simulations in FEKO. We also investigate the use of the radiating elements as part of a two-element, small-aperture direction finding system designed for operation at the VHF frequency band. Due to the small-spacing between the two antennas and the significant coupling between them through the platform, these two elements are used in conjunction with an external coupling network. The coupling network is used to both decouple the antennas from each other and create enhanced contrast between the amplitudes and phases of the two output signals. The direction finding performance of this small-aperture antenna array is evaluated by examining the Cramer-Rao lower bound (CRLB) of the array over the entire frequency range of operation with and without the coupling network. The simulation and preliminary measurement results of this system will be presented and discussed at the chapter 5.

Chapter 2

An Electronically Tunable Biomimetic Antenna Array

The full manuscript was published as:

M. Ranjbar Nikkhah, K. Ghaemi and N. Behdad, "An Electronically Tunable Biomimetic Antenna Array," *IEEE Transactions on Antennas and Propagation*, vol. 66, no. 3, pp. 1248-1257, March 2018.

2.1 Introduction

Miniaturization of sub-systems and components of wireless systems has been a growing trend in recent years in great part due to the advancements in integrated circuit technology. Antennas, however, have not followed this trend due to the fundamental laws of physics that govern the performance of electrically-small antennas. For example, in a single-element radiator, as size decreases, so do the antenna bandwidth and efficiency [1]- [4]. Similar limitations relating the aperture size of antenna arrays or continuous sources to their bandwidth, gain, and directivity have also been shown to exist. Despite these fundamental limitations, development of electrically-small antennas and arrays has been a long lasting need. This is particularly the case in applications where a large physical area is not available to accommodate the antenna or the array such as low-frequency communications systems or small-aperture direction finding systems.

Over the past few decades, a number of studies have examined the theoretical aspects and design challenges of antenna arrays with electrically-small spacing between the elements [2]- [8]. In [2], it was demonstrated that an electrically-small antenna array can be designed to demonstrate superdirectivity. However, there are significant practical challenges that make this rather impractical [5]. In practice, only moderate levels of superdirectivity can be achieved in an electrically-small antenna array [3], [7]. Compact antenna arrays have also been used in multiple-input-multiple-output (MIMO) communications systems [10], [30]. In MIMO applications, the mutual coupling between the closely spaced elements can deteriorate the performance of the system [35]. To address this problem, several studies have examined various techniques for decoupling the elements of the array using multi-port impedance matching networks [11], [32]. Arrays with small element spacing have also been developed for direction finding applications at relatively low frequencies (e.g. HF and VHF bands) [39], [40]. More recently, biologically-inspired antenna arrays that mimic the hyperacute senses of directional hearing of small animals were reported [15], [44]. Referred to as biomimetic

antenna arrays (BMAAs), these arrays enhance the phase differences between the output signals compared to the phase differences between the voltages induced on the antenna terminals. This phase enhancement capability increases the sensitivity of these arrays to the direction of arrival of an electromagnetic wave and can be useful in designing small-aperture direction finding systems. One of the common features of all of these compact or electrically-small antenna arrays is that they are narrowband structures whose bandwidths dramatically decrease with decreasing aperture sizes (element spacings). This trend is also observed in arrays designed for small aperture direction finding (e.g. [41] and [42]) as well as all of the biomimetic antenna arrays reported in [15], [43].

The narrowband nature of these arrays limits their applications to specific systems or frequencies. The narrowband behavior can be attributed to the high quality factor of the higher-order modes excited in such arrays. For example, in the two-element BMAA of the type reported in [21], the desired phase enhancement factor and output power level are obtained by extracting the maximum available power from the two linearly-independent excitation modes of the array (i.e., the common and the differential modes). When the elements are closely-spaced, the differential mode has a very high Q resulting in a narrow bandwidth over which the BMAA shows considerable phase enhancement factors. The bandwidth of such a two-element BMAA can be enhanced by introducing mismatch loss into the system. In such a situation, the power of the differential mode (which contains useful information about the direction of arrival of the wave) is extracted efficiently while the common mode power is not. This approach, however, results in sacrificing the output power level of the array and reduces the output signal-to-noise ratio as discussed in [21], [43]. Non-Foster impedance matching networks have also been proposed for increasing the bandwidth of a BMAA [20], [45]. In [20], a two-element non-Foster BMAA was reported that achieved enhanced bandwidth by using a negative reactance. However, in this design the output power level of the array is still slightly sacrificed and the output signal-to-noise ratio (SNR) is degraded by approximately 7 dB [20]. The design and simulation results of another non-

Foster BMAA, which extracts power efficiently from both modes, was reported in [45] but no measurement data were reported. One potential issue with using non-Foster impedance matching networks to enhance the bandwidth of BMAAs is the potential deterioration of the output SNR of the system due to the use of active elements in the ECNs of the arrays [46].

In this paper, we present a technique for enhancing the bandwidth of a two-element biomimetic antenna array by making its response electronically tunable. This technique addresses the major shortcomings of the previous BMAAs reported in the literature. Namely, the narrow bandwidth of passive BMAAs [15], [44] or significant sacrificing of the output SNR in case of non-Foster BMAAs [20]. While the proposed antenna has an instantaneously narrow bandwidth, its frequency of operation can be tuned over a relatively wide bandwidth thereby alleviating some of the bandwidth limitations of conventional biomimetic antenna arrays. The proposed antenna consists of two 13.5 cm long monopole antennas spaced at a distance of 2.5 cm. The two antennas are coupled together using a two-input-two-output ECN. A single varactor is used to tune the response of the ECN and change the frequency of operation of the BMAA. An equivalent circuit model for the antenna and its coupling network is proposed and used to design the BMAA and optimize its response. The device is designed to provide the maximum theoretically achievable phase enhancement factor without sacrificing the available output power of the array. A prototype of the device was fabricated and characterized experimentally. Measurement results show that the antenna can operate over the frequency band of 580 MHz to 700 MHz while providing a phase enhancement factor in the range of 1.8-2.1. In what follows, we will first present the design process and theoretical analysis of the proposed antenna followed by the measurement results of the fabricated prototype.

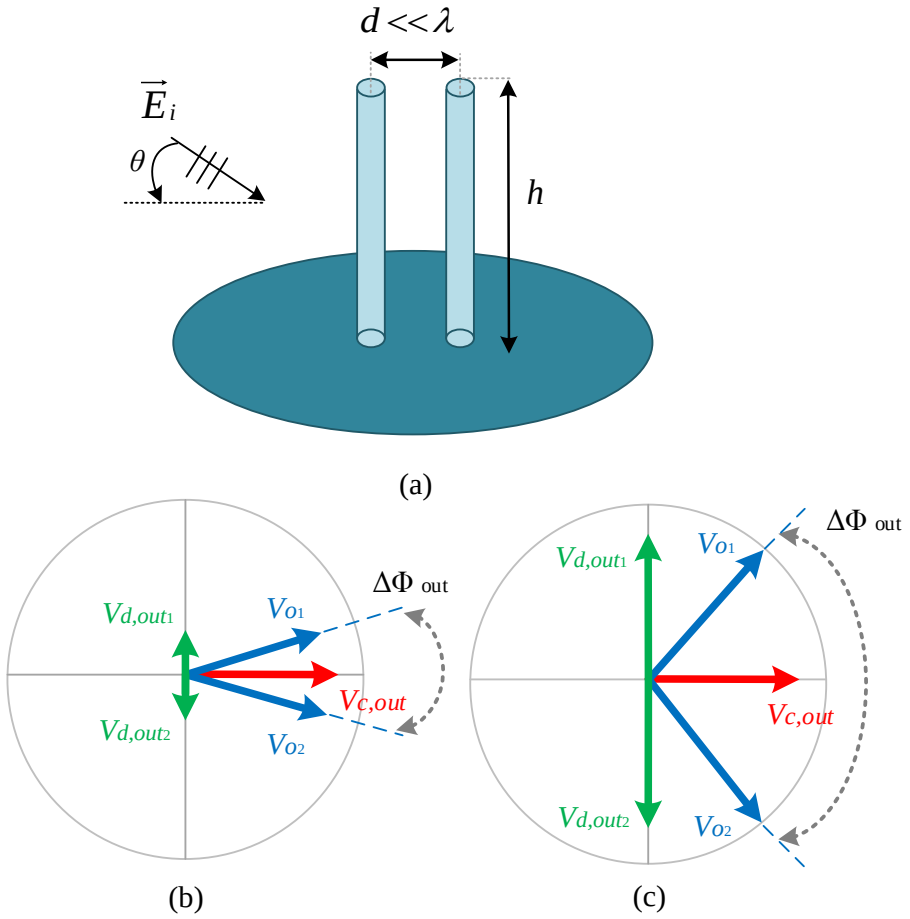

Figure 2.1: (a) A two-element antenna array with two closely-spaced elements. (b) In conventional impedance matching, the signal from the common mode excitation is extracted efficiently but that from the differential mode is not. In the best case, if $V_{c,out}$ and $V_{d,out}$ are orthogonal, a small phase difference exists between the two output signals. (c) In a two-element BMAA of the type discussed in [21], both the common mode and the differential mode powers are extracted efficiently and $\angle V_{d,out} - \angle V_{c,out} = 90°$. This results in a larger phase difference between the two outputs. V_{o1} and V_{o2} are defined as output voltages of the external coupling network (the voltage at the terminals of the 50 Ω loads).

2.2 Tunable BMAA Design and Principles of Operation

2.2.1 Bandwidth Limitations of a Two-Element Biomimetic Antenna Array

In a two-element biomimetic antenna array (or a generic two-element array for that matter) two linearly-independent modes of excitation exist. These include the common mode (CM) and the differential mode (DM). The array is excited in the common mode when both antennas are excited with the same magnitude and phase and in the differential mode when the two antennas are excited with the same magnitude but a 180° phase difference between them. When a two-element array is used in the receiving mode, the voltages induced on the two terminals of the antenna are a linear superposition of the CM and DM with coefficients that are determined based on the angle of incidence of the wave with respect to the boresight, θ. In a two-element BMAA of the type reported in [15], [44], the antennas are connected to a two-input-two-output ECN and the outputs of the array are obtained from the outputs of the ECN. The role of the ECN is to process the CM and DM of excitation differently and in the process, enhance the phase difference between the two signals at the outputs of the ECN compared to that of the signals induced at the antenna terminals. In early designs, however, this phase enhancement factor was obtained by sacrificing the power extracted from the array in the CM compared to that of the DM. This was performed by designing the ECN to be a more efficient impedance matching network for the DM of excitation compared to the CM (e.g. in [15], [16] and [20]). This, however, is not desirable as it reduces the total power available at the output of the array and results in reducing the output signal-to-noise ratio of the array. To address this problem, in [21], it was demonstrated that for a BMAA to extract the maximum available power from an incoming wave and offer phase enhancement factor, its ECN must be designed to impedance match the CM and the DM simultaneously.

This results in the maximum theoretically achievable phase enhancement factor without sacrificing the available power at the output of the array.

Fig. 2.1(a) shows the topology of a two-element antenna array with two closely-spaced monopoles. In conventional impedance matching, each antenna is individually impedance matched to extract the maximum available power from an incoming wave. In such an array, if the element spacing is small (i.e., $d << \lambda$), such an impedance matching network efficiently extracts the power from the CM but not from the DM. Fig. 2.1(b) shows the output signals at the two outputs of such an array. As can be observed, the phase difference between the two output signals is small because of the very small energy extracted from the DM of excitation. In a two-element BMAA, however, the ECN is designed to efficiently extract the power from both the CM and the DM of excitation. As a result, the extracted power from the DM will be significantly larger resulting in a larger phase difference between the two output signals while not sacrificing the total available power at the output as shown in Fig. 2.1(c). Indeed, based on the direction of arrival of the wave, such a two-element BMAA extracts more power from an incoming wave compared to its conventional array counterpart shown in Fig. 2.1(b).

The CM and DM of excitation of the array shown in Fig. 2.1(a) have different quality factors (Q). Specifically, as the spacing between the elements of this array decreases, the Q of the DM increases rapidly due to the oppositely directed currents on the two monopoles but the CM will maintain its low Q. As a result, the impedance matched bandwidth for these two modes is different. Fig. 2.2(a) shows the input reflection coefficients for the CM and the DM of the two-element BMAA reported in [21]. In this case, two quarter-wavelength monopoles with element spacing of $\lambda/20$ were used. Observe that the DM has a 10 dB return loss bandwidth of 2% in comparison with the 30% bandwidth of the CM. In this design, the bandwidth of the DM is the main factor limiting the bandwidth over which a considerable phase enhancement factor can be achieved.

To allow this two-element BMAA to operate over a larger bandwidth, the concept shown

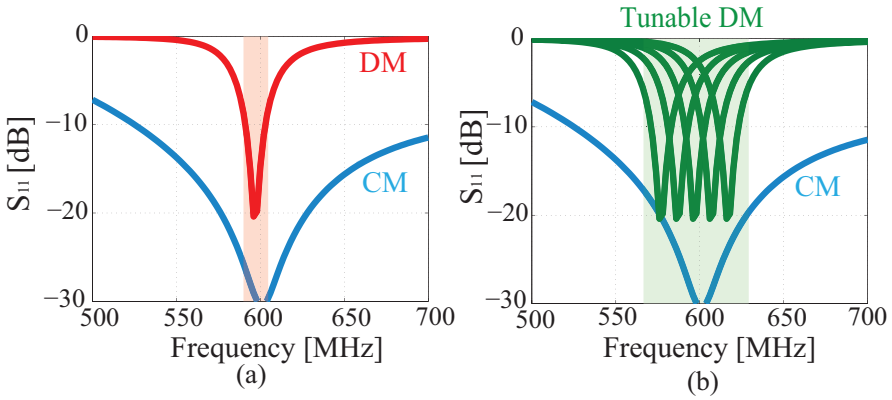

Figure 2.2: (a) S_{11} of a two-element BMAA reported in [21] for the differential and common modes of excitation. (b) To enhance the bandwidth of the BMAA, the center frequency of operation of the DM can be tuned.

in Fig. 2.2(b) can be exploited. Realizing that the main bandwidth limitation factor is the bandwidth of the DM, the response of the ECN can be tuned to change the frequency at which the DM is best impedance matched. This will move the frequency of operation of the BMAA (the frequency where the maximum phase enhancement factor can be achieved) over a relatively wide frequency range. Since the CM is already well impedance matched over a wide frequency range, in this scheme one only needs to tune the response of the DM. This simplifies the design of the ECN and reduces the number of actively tunable elements required to achieve tunability.

2.2.2 Design Procedure for an Ideal Tunable BMAA

Fig. 2.3 shows the equivalent circuit model of a two-element BMAA that uses symmetric antenna types and ECN. Each receiving antenna is modeled with its Norton equivalent circuit model and the mutual coupling between the two is taken into account using voltage dependent current sources. To simplify the design and optimization of the array, identical receiving elements and a symmetric coupling network is chosen. The symmetric ECN, has six independent reactive elements (B_1 to B_6) placed between the two antenna elements and connected to two load impedances of 50 Ω. The ECN of a general two-element BMAA is

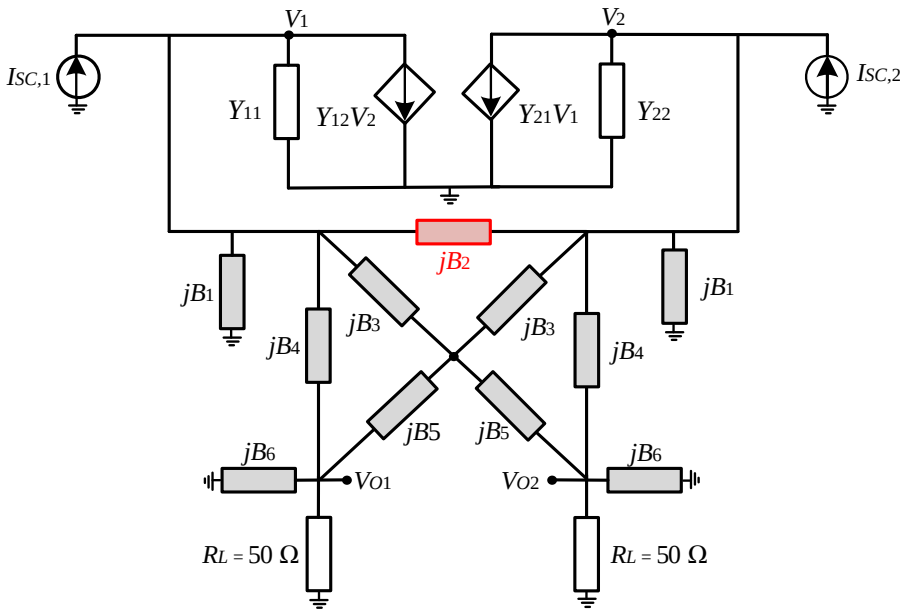

Figure 2.3: Equivalent circuit model of the proposed two-element tunable biomimetic antenna array. The ECN consists of six independent variables including $B_1 - B_6$. $I_{sc1}(\theta) = e^{j\alpha}$ and $I_{sc2}(\theta) = e^{-j\alpha}$ where $\alpha = \pi d \sin(\theta)/\lambda$. The coupling network elements are shown in gray color and tuned element is shown in red. V_1 and V_2 are defined as the voltages at the inputs of the external coupling network.

a four-port network, which can be represented with a $[S]_{4\times4}$ matrix. Assuming a lossless, reciprocal, and symmetric network, this $[S]_{4\times4}$ matrix has six degrees of freedom. The ECN architecture used in this design has six degrees of freedom (B_1 to B_6), which is sufficient for synthesizing a general two-element BMAA. However, other coupling network architectures can also be envisioned that will perform the same task.

The ECN should be designed to impedance match both the CM and DM and allow for continuously tuning the frequency at which the DM is impedance matched. To find the proper element to be tuned, the DM equivalent circuit model, shown in Fig. 2.4, is investigated. Electrical tuning of an element requires using biasing networks and DC block capacitors and RF chokes for RF/DC isolation. To simplify the design of the circuit and to minimize the losses associated with these components and with the active tunable element, the number of tunable elements should be kept at a minimum. Comparing the equivalent circuit models shown in Figs. 2.4(a) and 2.4(b), it is seen that B_2 is the only element that

Table 2.1: Element Values of The Ideal ECN for the Proposed Tunable-BMAA (Units in mS). B_2 is Selected as a Tuned Element.

Element	B_1	B_3	B_4	B_5	B_6
Value	4.02	-15.84	-3.54	-19.45	11.52

Table 2.2: Element Values for B_2 Required to Tune The Response of The Ideal BMAA to The Specified Frequency (Units in mS).

Freq. (MHz)	560	600	640	680	700
Value	21.80	14.02	9.72	6.62	5.42

appears only in the DM equivalent circuit and not in the CM. Thus, it is chosen to be the tunable element. Increasing the number of tunable elements in the ECN shown in Fig. 2.3 may offer some additional degrees of flexibility (e.g. enhancing the bandwidth) but it will come at the cost of added complexity and loss, which may offset some of the gains offered by this approach. This, however, needs to be examined further and is left for a future study.

Fig. 2.5 shows the self and mutual admittance of the two element antenna array shown in Fig. 2.1. In this case, the two monopoles are 13.5 cm long ($\lambda/4$ at 600 MHz) and their spacing

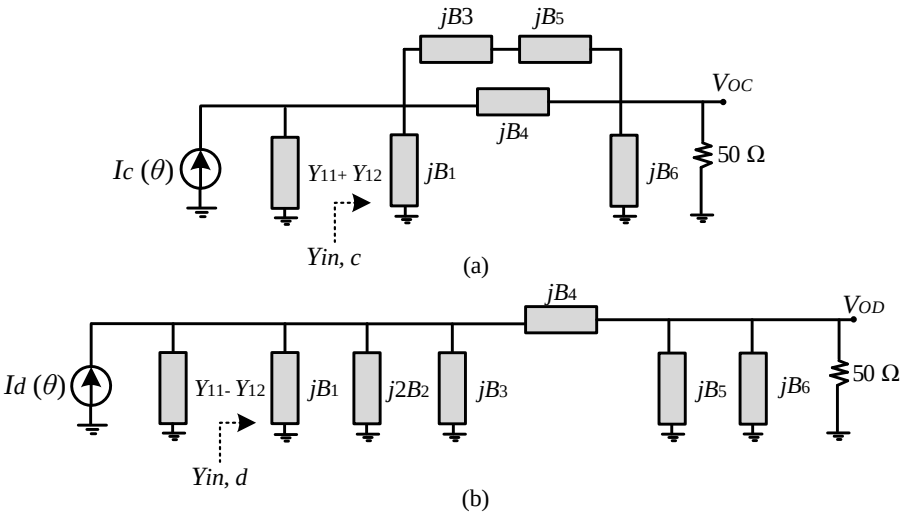

Figure 2.4: The equivalent circuit model of the tunable BMAA shown in Fig. 2.3 in (a) the common mode and (b) the differential mode of excitation. ($I_c(\theta) = \frac{I_{sc1(\theta)}+I_{sc2(\theta)}}{2}$, $I_d(\theta) = \frac{I_{sc1(\theta)}-I_{sc2(\theta)}}{2}$, $\Gamma_e = \frac{(Y_{11}+Y_{12})^\star - Y_{in,c}}{(Y_{11}+Y_{12})+Y_{in,c}}$ and $\Gamma_o = \frac{(Y_{11}-Y_{12})^\star - Y_{in,d}}{(Y_{11}-Y_{12})+Y_{in,d}}$).

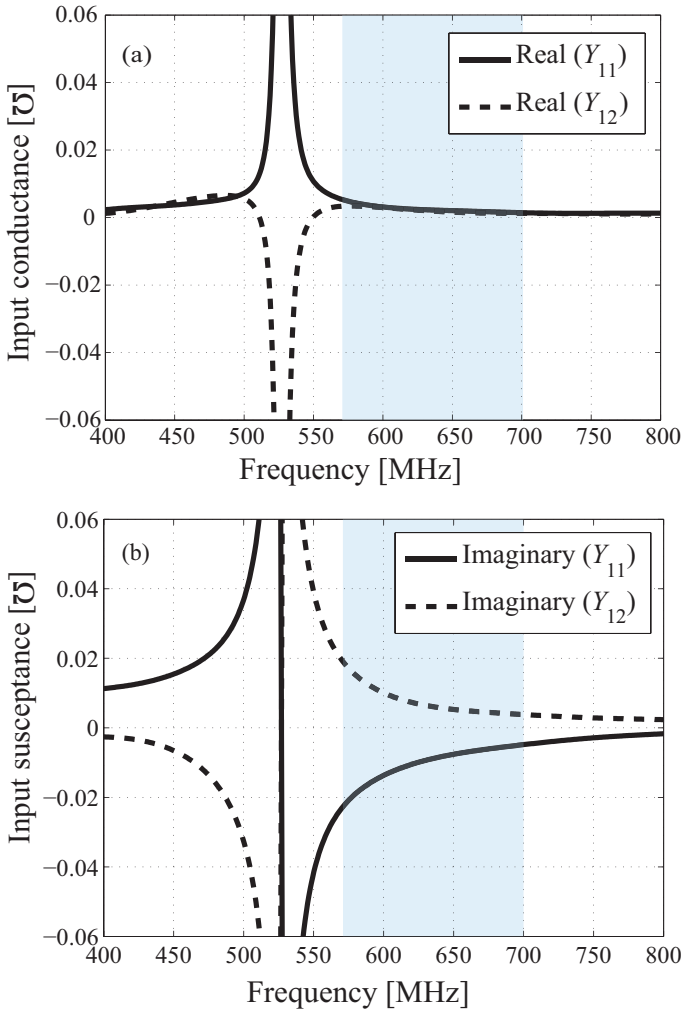

Figure 2.5: Input admittance of the two monopole antennas shown in Fig. 2.1 where their spacing is 2.5 cm and each monopole is 13.5 cm long. The results are obtained using full-wave EM simulations in CST Studio. (a) Real part. (b) Imaginary part. The desired frequency bandwidth of proposed tunable BMAA is highlighted in the figure.

is 2.5 cm ($\lambda/20$ at 600 MHz). The results are obtained using full-wave EM simulations in CST Studio. The highlighted region was chosen as the tuning frequency range, since the spectral variations of the admittance are smaller within this range. This directly impacts the range for which the value of B_2 needs to be tuned to match the DM at different frequencies and ensures that a tunable response can be achieved using a practical range for the value of B_2.

The ECN was designed to impedance match the CM at 600 MHz. This ensures that the

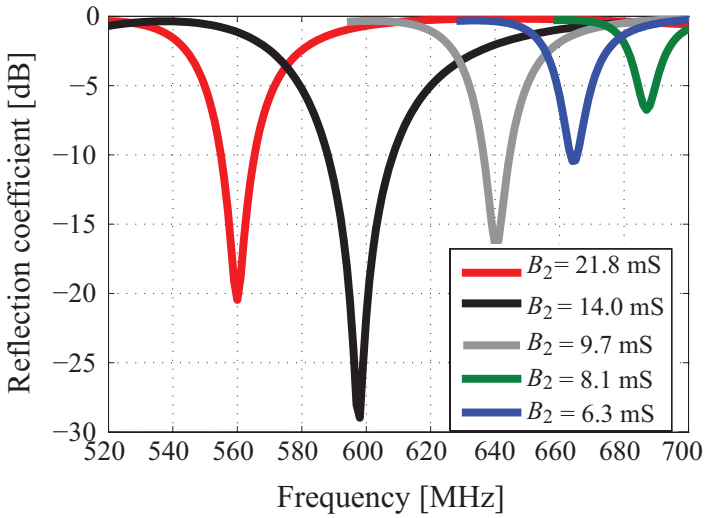

Figure 2.6: Simulated input reflection coefficients of the antenna in the differential mode of excitation. The results are shown for the different values of B_2.

maximum available power can be extracted from a plane wave incident on the array from boresight. Fig. 2.4(a) shows the antenna's equivalent circuit network in the CM. The values of B_1, B_3, B_4, B_5, and B_6 were chosen to impedance match the CM at 600 MHz and are reported in Table 2.1. Then, DM is impedance matched with the aid of the tunable reactive element, B_2.

To achieve optimum performance from the BMAA, the DM of the antenna array (with the equivalent circuit model shown in Fig. 2.4(b)) needs to be impedance matched and the output phase difference between $V_{c,out}$ and $V_{d,out}$ (see Fig. 2.1) should be 90°. To accomplish this at 600 MHz, a numerical optimization procedure is used to determine the element values of the ECN of the BMAA. This optimization procedure is carried out using the built-in optimization engine of the circuit simulation software Keysight Advance Design System (ADS). Three goals are defined in ADS optimization engine. The first and second goal are defined to satisfy the common mode and differential mode impedance matching conditions. The third goal is that the phase difference between the output voltages of the common and differential mode must be equal to 90°. To tune the response of the BMAA over the frequency range of 560-700 MHz, the value of B_2 must be changed. This has to be done in a

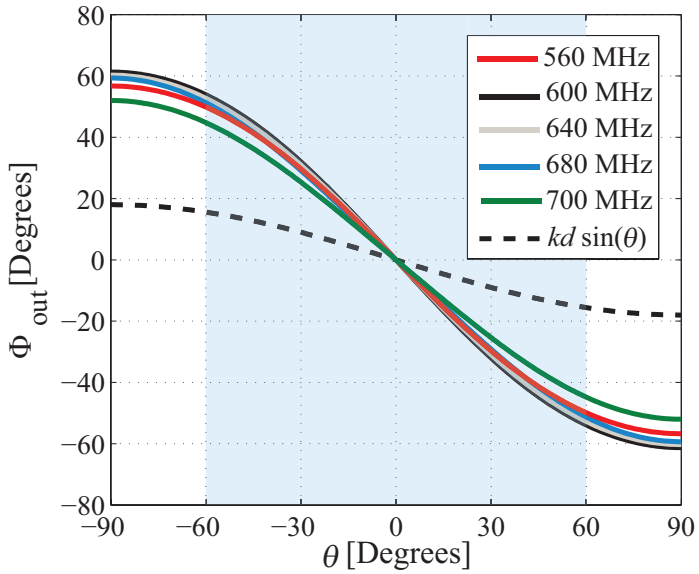

Figure 2.7: Phase responses of the ideal two-element tunable BMAA whose equivalent circuit model is shown in Fig. 2.3 at different frequencies. The obtained values of ECN elements: $B_1 = 4.02$, $B_3 =$ -15.84, $B_4 =$ -3.54, $B_5 =$ -19.45, and $B_6 = 11.52$. B_2 is considered as tuned element and its values are shown in Table 2.2. Units are in mS. The output phase difference of the BMAA has a higher rate of change for $|\theta| < 60°$ compared to $60° < |\theta| < 90°$ as it is highlighted in the figure.

manner to ensure that the DM is impedance matched *and* the phase difference between the DM and CM outputs is at 90°. Following this process, the required values of B_2 are obtained and are listed in Table 2.2. Observe that these values are all capacitive. This indicates that a varactor can be used to implement the reactive element B_2. By changing B_2 values in this manner, a tunable DM impedance-matching network can be achieved. Since the CM is impedance matched over the entire frequency band as well, the BMAA has the potential to operate in an optimum manner. Fig. 2.6 shows the input reflection coefficient of the antenna in the differential mode, seen from the output, for different values of B_2 reported in Table 2.2. For most of the band, the input reflection coefficient of the DM remains below -10 dB. At 690 MHz and above, the DM matching deteriorates. However, as discussed in Section 2.2-C (see the discussions on the Figure or Merit of the BMAA), this does not significantly impact the overall performance of the BMAA.

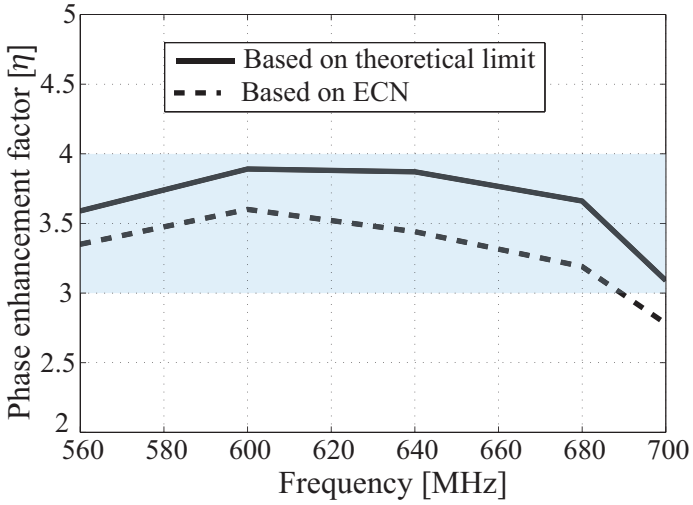

Figure 2.8: Phase enhancement factor of the proposed tunable-BMAA based on theoretical limit presented in (2.1) and also the ideal design of the ECN shown in Fig. 2.3.

Fig. 2.7 shows the output phase difference of the tunable BMAA using an ideal tunable coupling network. As seen, the output phase difference is compared to that of a regular antenna array. The output phase difference of the BMAA has a higher rate of change for $|\theta| < 60^\circ$ compared to $60^\circ < |\theta| < 90^\circ$ as it is highlighted in Fig. 2.7. The maximum phase enhancement factor achievable from the two element antenna array considered in this work is shown to be $\eta = 3.7$. This is calculated using the following equation derived in [21]:

$$\eta_{max} = \sqrt{\frac{\mathrm{Re}(Y_{11}) + \mathrm{Re}(Y_{12})}{\mathrm{Re}(Y_{11}) - \mathrm{Re}(Y_{12})}} \tag{2.1}$$

This bound is a function of the antenna admittance parameters and specifies the maximum theoretical phase enhancement factor that can be achieved without any sacrifice of the available power at the outputs of the array. Fig. 2.8 compares the achieved phase enhancement factor values with the maximum theoretical bound derived from (2.1). As observed, the achieved phase enhancement factor values are very close to this theoretical bound. The

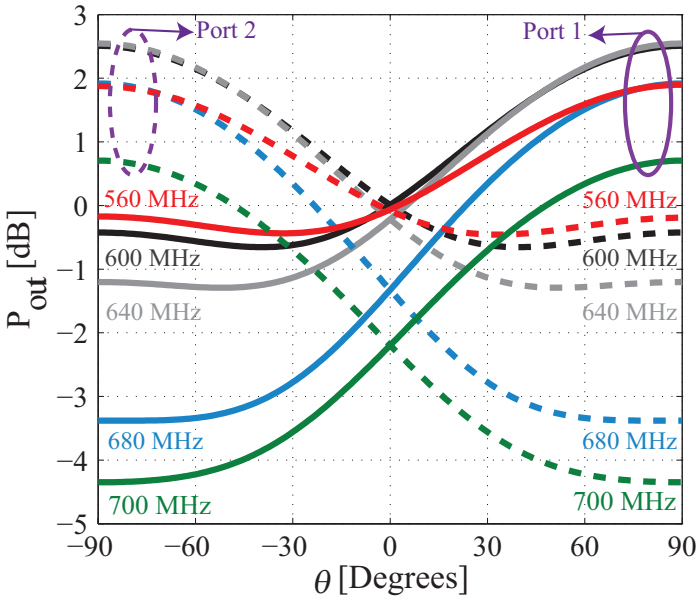

Figure 2.9: Amplitude responses of the ideal two-element BMAA at different frequencies. Power levels at the two BMAA outputs are normalized to the output power level achieved from a regular antenna array (i.e., BMAA without the coupling network).

available output power from a regular two-element antenna array is

$$P_0 = \frac{1}{8(\mathrm{Re}(Y_{11}) + \mathrm{Re}(Y_{12}))} \tag{2.2}$$

This can be calculated easily for the two-element antenna array considered in this work (see Fig. 2.1) using the antenna admittances shown in Fig. 2.5. To make sure that the designed BMAA extracts the maximum power from an incident wave, the output power of the coupling network is normalized to this P_0 at each frequency. Fig. 2.9 shows the normalized output power of the BMAA for various different frequencies versus the incidence angle. As observed, over most of the band, the tunable BMAA has the same available output power level compared to that of the regular array at boresight. At off boresight angles, the BMAA extracts more power as expected because of the significantly more efficient impedance matching of the DM of excitation of the array.

2.3 Prototype Design and Practical Implementation Issues

2.3.1 Rigorous Modeling of Varactor and RF Choke

In Section 2.2, the values of the tunable element, B_2, were calculated without considering the effects of its physical implementation. This tunable element should be realized using an appropriate varactor capable of providing the required range of capacitance values. Furthermore, the parasitics of the varactor may impact the performance of the tunable BMAA. Therefore, realistic models for the chosen varactor must be used in the design process of the proposed antenna. Fig. 2.10 shows the equivalent circuit model of the proposed tunable BMAA, which includes a realistic model for the varactor, the DC bias capacitors, and RF/DC isolation chokes (filters). The methodology used for selecting the varactor is outlined in the flowchart shown in Fig. 2.11. Following this process, we chose the commercially available device SMV 1408 from Skyworks.

The varactors is biased using two low pass filters (LPF) that act as RF chokes placed between the DC bias source and the varactor terminals. The LPFs provide better than 20 dB attenuation within the entire band of operation of the proposed tunable BMAA. Two 100 pF capacitors with finite quality factor of 80 are used to provide DC isolation as shown in Fig. 2.10. Due to the parasitic effects of the varactor, RF chokes and the DC blockers, slight modifications were made to B_1, and B_3 to B_6 values compared to the values reported in Table 2.1.

2.3.2 Detailed Modeling of the Proposed Tunable BMAA

In practice, parasitic effects of the inductors and capacitors used in the ECN of the BMAA should be taken into account in the design of the device. Therefore, the accurate model of all elements, are obtained from the manufacturer and used in the equivalent-circuit model

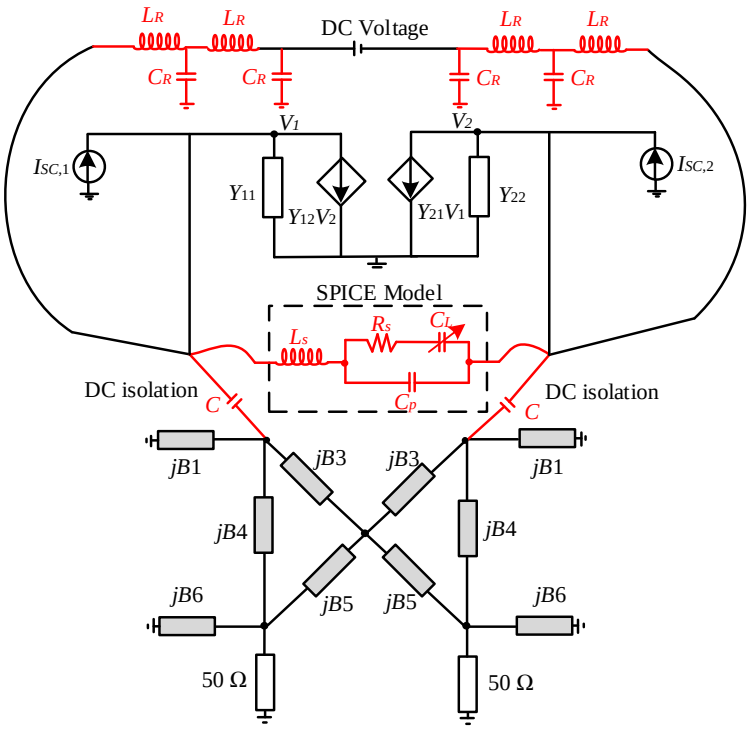

Figure 2.10: Equivalent circuit of the proposed tunable BMAA including the varactor SPICE model, the low pass filters used as wideband RF chokes including L_R and C_R, and capacitors that are used for DC isolation.

simulations in Keysight ADS [47]. In this stage, to improve the performance of the tunable BMAA and also considering the availability of commercial inductors and capacitors, the

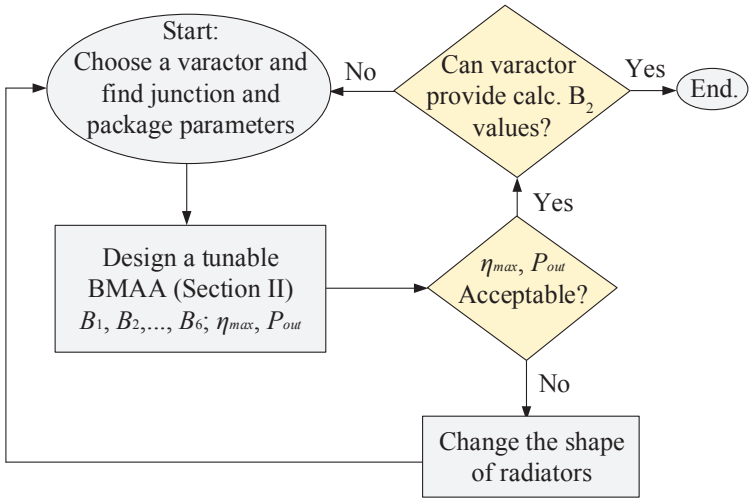

Figure 2.11: Simplified flowchart showing the process that was followed to select a suitable varactor for the proposed two-element tunable BMAA.

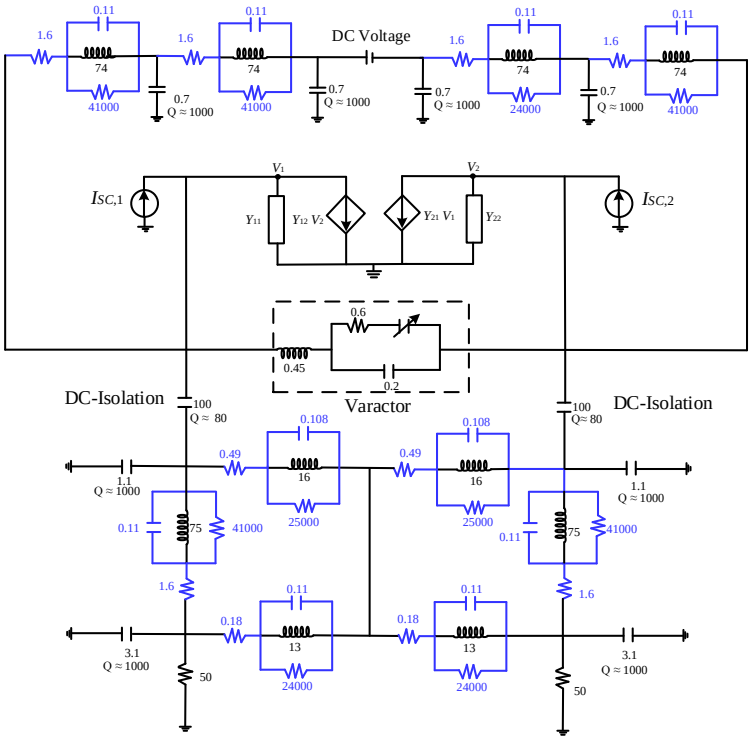

Figure 2.12: The circuit model of the proposed tunable BMAA including all the parasitic effects of the designed ECN. The element values are in nH, pF, and Ω.

obtained values for the ECN in Section 2.2, were changed slightly. Fig. 2.12 illustrates the circuit model of the finalized tunable BMAA. The normalized output power of the proposed tunable BMAA, taking into account all of the nonidealities in its ECN, are shown in Fig. 2.13. As can be observed the output power level of the BMAA at boresight is at most 0.7 dB lower than the available output power from an ideal conventional antenna array. Notice that in this calculation, the losses in the impedance matching network of the conventional array are not taken into account. Therefore, this represents a worst case scenario. Based on Fig. 2.12 and considering all the parasitic effects, the output phase difference of the proposed tunable BMAA is also calculated and is shown in Fig. 2.14. As seen, a phase enhancement factor of 2.3 is expected to be achieved over the entire frequency range of operation.

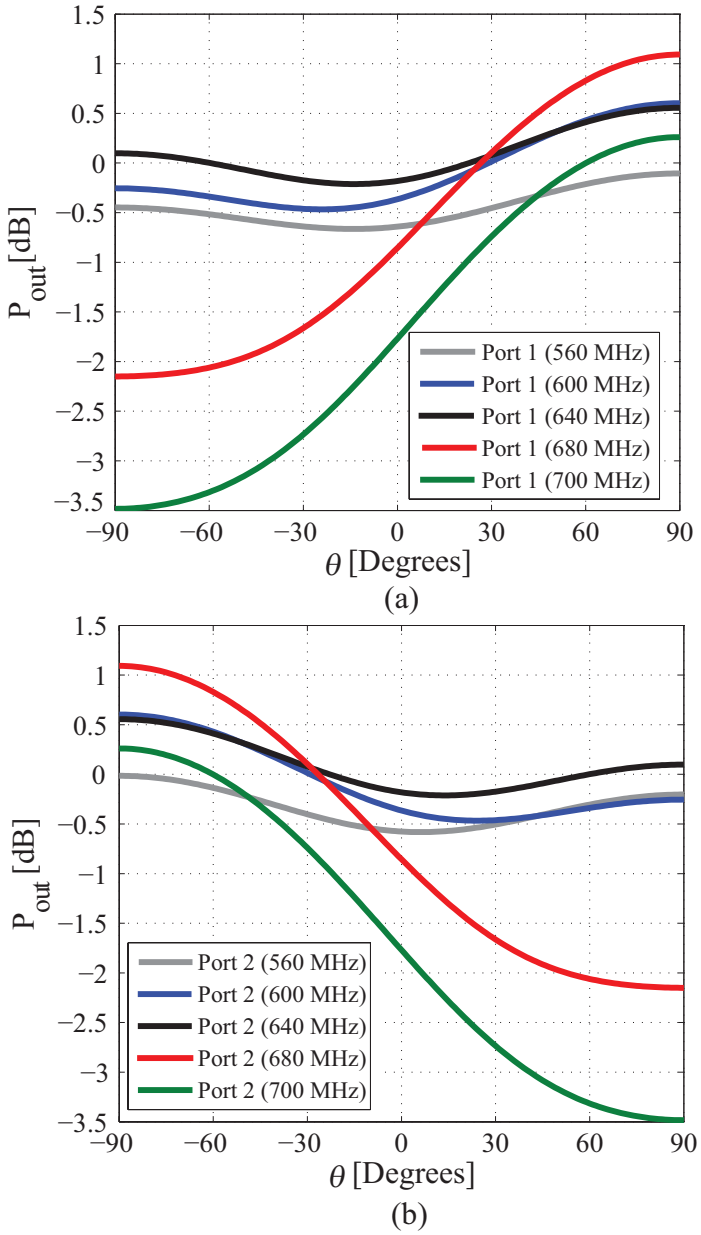

Figure 2.13: Simulated amplitude responses of the proposed two-element BMAA discussed in Section 2.3 at different frequencies. Power levels at the two BMAA outputs are normalized to the output power level achieved from a regular antenna array (i.e., BMAA without the coupling network) with an ideal impedance matching network. (a) Port 1, and (b) port 2.

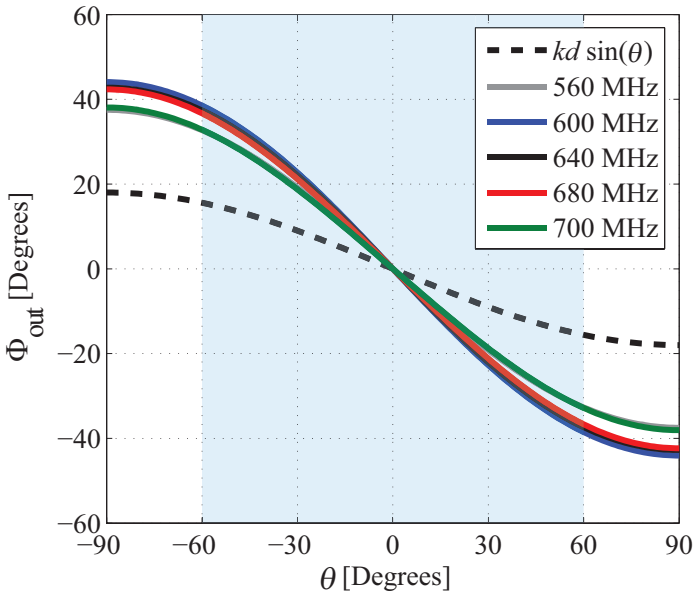

Figure 2.14: Simulated output phase responses of the two-element tunable BMAA shown in Fig. 2.12 and discussed in Section 2.3 as well as the phase response corresponding to the propagation of an electromagnetic wave over a distance of d at an angle of θ. The output phase difference of the BMAA has a higher rate of change for $|\theta| < 60°$ compared to $60° < |\theta| < 90°$ as it is highlighted in the figure.

2.3.3 Figure of Merit for Quantifying the Performance of a Two-Element BMAA

To judge the performance of a two-element BMAA in a quantifiable manner, we propose a figure of merit (FoM) that takes into account the achieved phase enhancement factor and the sacrifice in power (if any) that has been made to achieve it. These two parameters are important if such a BMAA is to be used in a direction finding application. In fact, based on the analysis presented in [13] (Chapter 9), it can be shown that the direction finding accuracy of a two-element BMAA is proportional to $\propto \eta\sqrt{\text{SNR}}$. Based on this, we define the following FoM for a two-element BMAA:

$$FoM = \eta_{max}.\sqrt{\text{sacrificed power}} \tag{2.3}$$

This FoM can be used to compare the performance of a two-element BMAA with that of

Table 2.3: Calculated Phase Enhancement Factor, Relative Output Power, and The Figure of Merit of The Proposed Tunable BMAA [Freq.: Frequency [MHz], B_2: Tuned Element].

Freq. [MHz]	B_2 [Siemens]	η	Sacrificed Power(dB)	FoM
560	21.1	2.14	-0.63	1.99
580	16.72	2.4	-0.57	2.24
600	13.4	2.6	-0.4	2.48
640	9.02	2.5	-0.2	2.44
680	5.52	2.35	-0.85	2.13
700	4.12	2.1	-1.7	1.72

a conventional array as part of a small-aperture direction finding system[1]. The FoM of the proposed tunable BMAA is calculated at a number of different frequencies using the the simulation results presented in Fig. 2.12 and the results are presented in Table 2.3. Observe that the structure is expected to provide a FoM better than 1.7 over the frequency range of 560 MHz-700 MHz that corresponds to $\sim$ a 22% bandwidth. In comparison, the non-tunable BMAA reported in [21] has a $FoM = 1.7$ over a 2.5% bandwidth.

2.4 Fabrication and Measurement Results

To experimentally verify this design, a prototype of the proposed BMAA was fabricated. The ECN was fabricated on a Rogers RO4003C substrate with the relative dielectric constant of 3.55 and a thickness of 0.76 mm. The two monopole antennas are made out of hollow copper tubes with a circular cross section with inner and outer radii of 1.8 mm and 2.4 mm, respectively. The two monopoles are mounted on a brass ground plane with physical dimensions of 60 cm $\times$ 60 cm. To minimize the impact of the scattering and diffraction from the edges of the finite ground plane on the BMAA response, the edges of the ground plane are covered with thin absorbers (6.35 mm thick ECCOSORB LS-30/SS-3 absorbers manufactured by Emerson and Cuming). The varactor is biased by an external voltage

[1]In this case, we are assuming that the impedance matching network of the regular array and the ECN of the BMAA are both lossless and do not add any additional noise to the system. This is done for simplicity but the definition can be extended to include the noise generated by the matching networks as well.

source. The applied voltage varies from 0.5 to 30 V corresponding to a capacitance range of 4.08-0.95 pF.

The response of the fabricated BMAA was measured using a calibrated vector network analyzer. The antennas were characterized by illuminating them with a vertically polarized plane wave from various incidence angles in the azimuth plane and measuring the two output signals. The plane wave was generated by a vertical standard dipole antenna tuned to operate at the desired frequency range and located in the far field of the receiver. The measurement system consists of the transmitting dipole antenna and the receiving BMAA placed in the far-field of the dipole. One port of the VNA was connected to the transmitter and two of its ports were connected to the outputs of the BMAA. The S_{21} and S_{31} scattering parameters were measured and compared to characterize the fabricated BMAA performance. Range gating in the vector network analyzer was used to minimize the impact of reflections of the transmitted wave from the ground and surrounding objects. Furthermore, RF absorbers were placed on the ground at the specular reflection point and absorbers were used to cover the edges of the ground plane of the BMAA to ensure that the measurement is dominated by the direct path between the transmit and receive antennas. Fig. 2.15 shows the measured output phase differences of the proposed BMAA for different angles of incidence and compares them with those of a regular array with the same elements and dimensions without an ECN. As observed, there is a good agreement between the measured and simulated results. In Section 2.2, we demonstrated that an average phase enhancement factor of 3.6 can be achieved from an ideal tunable BMAA over this entire frequency range (See Section 2.2-B, Figs. 2.3 and 2.7). However, due to the loss and parasitic effects of the varactor, LPFs and all the reactive elements used in the ECN of the BMAA, the achievable average phase enhancement factor was reduced to 2.3 (see Section 2.3, Figs. 2.10, 2.12 and 2.14). The measurement results shown in Fig. 2.15 demonstrate that an average phase enhancement factor of 2 is achieved from the fabricated prototype.

As shown in Fig. 2.15, the output power level of the BMAA is not sacrificed compared to

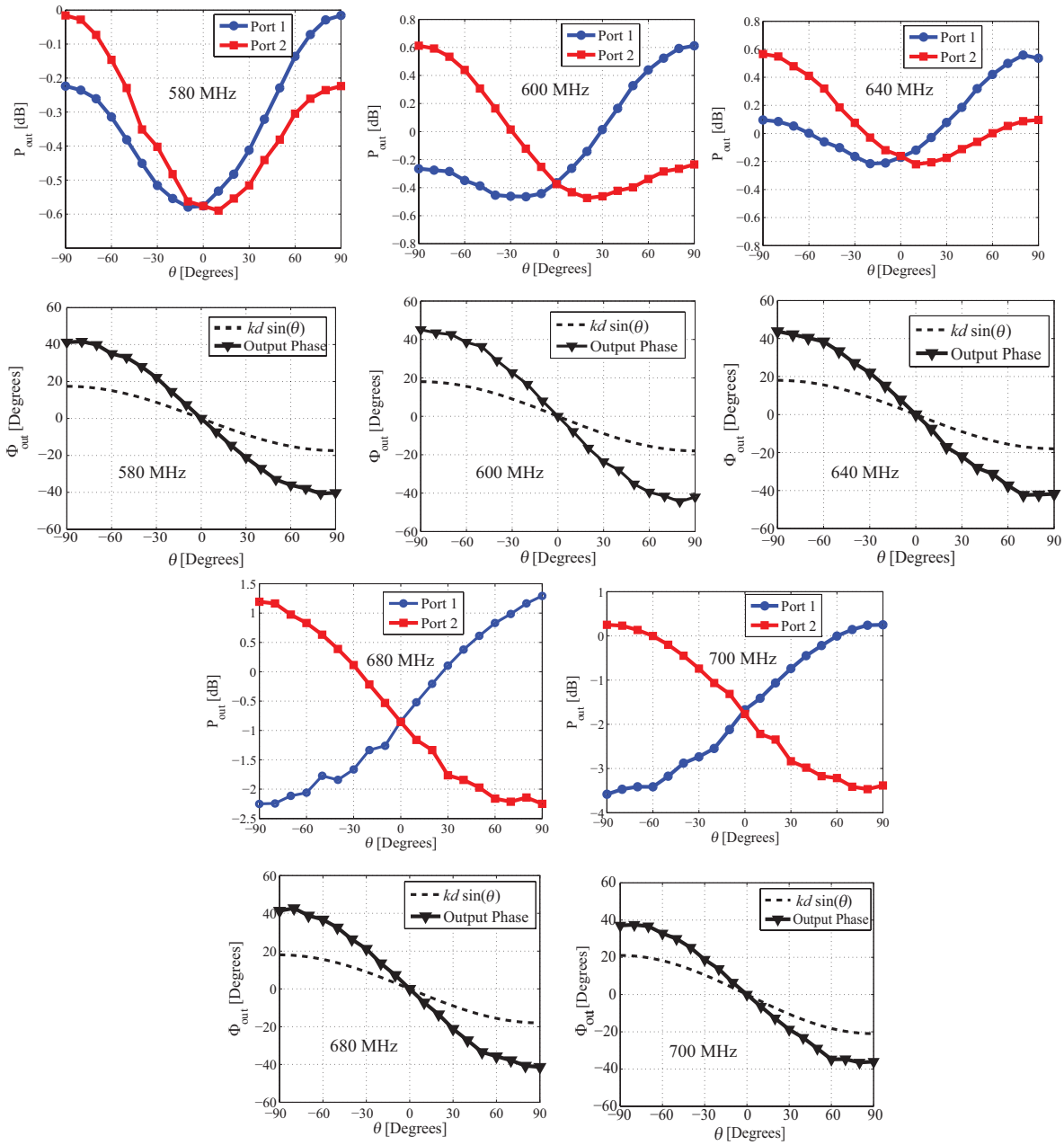

Figure 2.15: Measured output phase and amplitude responses of the two-element BMAA at different frequencies. Power levels at the two BMAA outputs are normalized to the output power level achieved from a regular antenna array (i.e., BMAA without the coupling network) that uses an ideal impedance matching network without any losses.

the available output power from a regular two-element antenna array, $P_0 = \frac{1}{8(\mathrm{Re}(Y_{11})+\mathrm{Re}(Y_{12}))}$. As observed, the tunable BMAA sacrifices at most 1 dB of the available power at boresight over the frequency range of 580 MHz- 680 MHz. At 700 MHz, this increases to 1.8 dB and the phase enhancement factor of the BMAA also reduces. The factors contributing to the discrepancies observed between the measured and the simulated results include the tolerances and losses of the component values of the capacitors and inductors, slight asymmetries existing in the fabricated antenna array and its ECN, potential measurement uncertainties, and the finite dimensions of the ground plane, which was assumed to be infinite in the simulations. Nevertheless, the measurement results are in good agreement with simulations. The tuning range of 560-700 MHz mentioned in Section II-B (based on the values provided in Table 2.1), is what was expected to be achieved based on simulation results. The measurement results shown in Section 2.3 demonstrate that the tuning range achieved covers the range of 580-700 MHz. This difference is primarily attributed to the tolerances and the losses of the lumped elements used in the construction of the proposed tunable BMAA.

2.5 Conclusions

The architecture and the design procedure of a tunable two-element biomimetic antenna array was presented. The BMAA was designed to have a tunable response over the frequency range of 560 MHz to 700 MHz. It was demonstrated that the response of a two-element BMAA can be tuned by designing its ECN to provide a tunable impedance match for the high-Q differential mode of excitation of the array while providing a constant impedance matching for its common mode of excitation. A simple architecture for the ECN of this tunable BMAA, which uses only a single varactor to achieve tunability, was also proposed. A prototype of the antenna was designed and simulated. The impact of the nonidealities of the varactors, lumped element reactive components, RF/DC isolation chokes, and the DC isolation capacitors were all taken into account in the design process of the antenna.

A prototype of the proposed device was also fabricated and experimentally characterized in the lab. A tuning range of 580-700 MHz were obtained in the measurements and the measurement results were shown to be in good agreement with the simulations.

In this work, we focused on enhancing the bandwidth of the tunable BMAA by using only a single tunable element. One can envision that the tuning range can be extended using a number of different techniques. One technique is to use antenna elements (other than the monopoles used here) that have a lower differential mode Q. In such a case, using a coupling network with a similar architecture, we expect that a larger tuning bandwidth can be obtained. Another technique is to use a more complicated coupling network architecture that has more than one tuning element. In this case, it is possible to tune the frequency of the best impedance match for the common mode and that of the differential mode simultaneously. This will allow for significantly increasing the bandwidth of the device. However, this will come with the added complexity of having more actively tunable elements and the additional lumped elements that are needed to bias them. In predicting the performance or usefulness of any such design, one can use the figure of merit defined in Section 2.3-C.

Chapter 3

A Three-Element Biomimetic Antenna Array with an Electrically-Small Triangular Lattice

The full manuscript was published as:

M. Ranjbar Nikkhah, K. Ghaemi and N. Behdad, "A Three-Element Biomimetic Antenna Array with an Electrically-Small Triangular Lattice," *IEEE Transactions on Antennas and Propagation*, vol. 65, no. 8, pp. 4007-4016, Aug. 2017.

3.1 Introduction

In many wireless applications, antenna size is one of the biggest obstacles in the path of miniaturizing the system dimensions. Major advancements in electronics industry and integrated circuit technology have resulted in significant miniaturization of the sub-systems and components used in a typical radio transceiver. However, due to fundamental physical limitations, a similar level of reduction in the dimensions of antenna apertures have not been, and may not ever be, achieved. Nevertheless, reduction of antenna size is an important problem particularly in applications that operate at low RF/microwave frequencies where the wavelength of the electromagnetic wave is large or in applications where the available real estate simply does not allow for placement of antennas with large apertures. These problems are drastically exacerbated in applications where an antenna array must be used to perform tasks that cannot be accomplished efficiently using a single-element radiator (e.g. beam forming, direction finding, etc.). In such applications, antenna arrays with electrically-small aperture dimensions are needed.

Compact and small antenna arrays have been studied for more than 70 years. Early works in this area examined the concept of superdirectivity in arrays with electrically-small spacing between the elements [1]- [3]. These works demonstrated that achieving superdirectivity from an electrically-small array is possible in theory but implementing it in practice is challenging due to the precision with which excitation coefficient of the array must be synthesized, the strong mutual coupling between adjacent elements, and the losses in the feed network. Subsequently, other studies examined various other attributes of superdirective arrays including examination of the bandwidth and loss issues in such arrays [4], the use of active elements to increase the bandwidth [5], and innovative superdirective array designs [6]. The impact of mutual coupling between the closely-spaced elements of electrically-small arrays have also been extensively studied [7]- [8]. In [9]- [12], techniques for compensating the mutual coupling effects in such arrays were proposed including orthogonal eigenmode

method [9], multiple input multiple output antenna decoupling networks [10], and wideband isolation of coupled closely-spaced antenna arrays using resistive elements [11]. In [12], a matrix method was reported to compensate the mutual coupling effects on array radiation patterns utilizing a modification matrix obtained from measured element patterns. The application of electrically-small antenna arrays in two-element MIMO system is examined in [30]. Mode-based methods for beam-forming in such arrays are also examined in [31].

Small-aperture direction finding is another application where electrically-small antennas or antenna arrays have been used [13]- [14]. Partly motivated by the requirements of this application, recently a class of biologically-inspired electrically-small antenna arrays have been reported [15]- [16]. Referred to as biomimetic antenna arrays (BMAAs), these antennas mimic the hyperacute senses of directional hearing of small animals [17]. A BMAA consists of a number of closely-spaced receiving antenna elements coupled together using an external coupling network (ECN). The role of the ECN is to convert the small phase differences between the received signals at its input (antenna terminals) to larger phase differences at its outputs. In the biological systems that BMAAs mimic, this phase enhancing capability is the main mechanism that allows the small animals to perform precise direction finding using an acoustically-small receiving aperture [18]. In [15]- [16], two-element BMAAs that directly mimic the sense of auditory hearing a parasitoid fly were introduced. This concept was later expanded to a three-element BMAA with a linear baseline [19]. More recently, a two-element BMAA was reported, which uses a non-Foster external coupling network to increase the antenna's operating bandwidth [20]. While these antennas achieve a phase enhancement capability, they do this at the expense of sacrificing the available output power level of the array compared to a conventional array. This is a major drawback, since reduction of the output power level reduces the output signal-to-noise ratio of the array in situations where the primary noise source is that of the receiver. In [21], it was theoretically and experimentally demonstrated that in a two-element BMAA, an upper bound for the maximum phase enhancement factor exists that can be achieved without sacrificing the output power level of

the array compared to a conventional array.

In this paper, we present a three-element biomimetic antenna array with a triangular-shaped electrically-small lattice. The motivation for proposing this new BMAA architecture is to address three of the shortcomings of previously-reported two- or three-element BMAAs. First, any array whose elements are placed along a linear baseline and has identical antenna elements has an inherent 180° ambiguity in its phase response. Secondly, in BMAAs with linear baselines, the maximum phase sensitivity is generally obtained over a limited field of view along the boresight direction. For example, in the two- and three-element BMAAs reported in [16] and [19], the array's phase sensitivity deteriorates as the incidence angle is increased beyond $|\theta| > 60°$. Finally, in most two- or multi-element BMAAs reported previously [15]- [16], [19]- [20], and [48], the output power level of the array is sacrificed to achieve the desired output phase sensitivity (the only notable exception is the two-element BMAA reported in [21]). These factors limit the performances of the systems that use such BMAAs and in some applications (such as small-aperture direction finding), they represent serious limitations. The proposed three-element BMAA, however, simultaneously addresses all of these challenges. In this antenna, each element of the array is coupled to the other two elements using a rotationally symmetric external coupling network. A modal-based technique for analyzing the proposed BMAA, based on its equivalent circuit model, is presented and is used to obtain an upper bound limit on its phase enhancement factor. Using this technique, a BMAA prototype operating at 600 MHz is designed, fabricated, and experimentally characterized. Measurement results are found to be in good agreement with the theory and verify the underlying hypotheses.

3.2 Principles of Operation and Analysis Methods

3.2.1 Modal Analysis of a Generic Three-Element BMAA

A two-element biomimetic antenna array (e.g. in [16] and [21]), used as a receiver, can be considered to have two linearly independent modes of excitation. These include the common mode and the differential mode. The array is excited in the common (differential) mode when the open circuit voltage at the terminals of the receiving antennas have the same magnitude and a 0° (180°) phase difference between them. In a general case where the array is receiving a plane wave arriving from a direction making an angle θ with respect to the boresight direction, the voltages induced at the input terminals of the antennas are a linear combination of the common and the differential modes of excitation [16]. The relative weights of these components are determined by the angle of arrival of the wave, θ, and the spacing between the two elements of the array, d. For instance, for $\theta = 0°$, the array is excited in the common mode and for $\theta = 90°$ and $d = \lambda/2$, the array is excited purely in the differential mode.

The block diagram of a generic three-element BMAA is shown in Fig. 3.1(a). This BMAA is assumed to have three receiving elements (antennas) and a three-input-three-output external coupling network, which takes the input signals received at the antenna terminals (labeled as V_{i1}, V_{i2}, and V_{i3} in Fig. 3.1(a)) and converts them to the output signals measured at the outputs of the external coupling network (labeled as V_{o1}, V_{o2}, and V_{o3}). Such a network with three independent inputs has three linearly-independent modes of excitation, which form a set of orthogonal basis functions. For an arbitrary excitation, the response of the circuit can be represented in terms of a linear combination of the responses of the circuit for each basis function. For example, $(V_{i1}, V_{i2}, V_{i3}) = (1, 0, 0), (0, 1, 0)$, and $(0, 0, 1)$ form such an orthogonal basis function. In this analysis, however, we choose the following independent modes of excitations: $(V_{i1}, V_{i2}, V_{i3}) = (1, 1, 1), (-1, 0, 1), (-1/2, 1, -1/2)$ to simplify the subsequent circuit analysis steps. Based on this assumption for these orthogonal

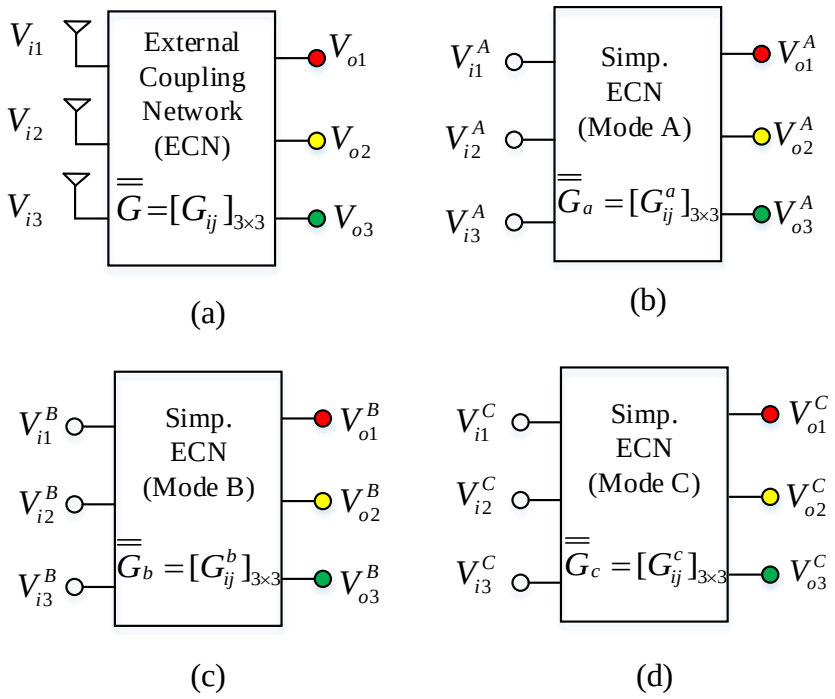

Figure 3.1: (a) Generic model of a three-element biomimetic antenna array with a 3×3 external coupling network (ECN). This array has three linearly independent modes of excitation identified here as Modes A, B, and C. (b)-(d) The equivalent circuit model of the BMAA and its external coupling network can be simplified for each specific mode of excitation. Depending on the architecture of the coupling network, modes B and C can be chosen to simplify the architectures of their equivalent circuit models and simplify the BMAA analysis.

vectors, the response of the array for a general incoming wave in terms of (V_{i1}, V_{i2}, V_{i3}) can be decomposed as shown in Figs. 3.1(a)-3.1(d). Depending on the specific architecture for the external coupling network used, it may be possible to simplify the coupling network topology for the excitations shown in Figs. 3.1(b)-3.1(d). In this work, since an array with a triangular lattice and identical receiving elements is chosen, a rotationally symmetric coupling network will be used to simplify the design and optimization of the array. Considering such a symmetric BMAA topology allows for simplifying the architecture of the system for the three linearly-independent modes of excitation considered here. Specifically, for each linearly-independent mode of excitation, the architecture of the coupling network can be simplified and its response can be expressed with a 3×3 tensor ($\overline{\overline{G_a}}$, $\overline{\overline{G_b}}$, and $\overline{\overline{G_c}}$) as shown

in Figs. 3.1(b)-3.1(d). Based on this, the output of the system can be represented as:

$$\begin{aligned}\overline{V_O} = [&\frac{V_{i1}+V_{i2}+V_{i3}}{3}, \frac{V_{i1}+V_{i2}+V_{i3}}{3}, \frac{V_{i1}+V_{i2}+V_{i3}}{3}]\overline{\overline{G_a}} \\ &+[\frac{V_{i1}-V_{i3}}{2}, 0, \frac{V_{i1}+V_{i3}}{2}]\overline{\overline{G_b}} + [(\frac{V_{i1}}{6}+\frac{V_{i3}}{6}-\frac{V_{i2}}{3}), \\ &(-\frac{V_{i1}}{3}-\frac{V_{i3}}{3}+\frac{2V_{i2}}{3}), (\frac{V_{i1}}{6}+\frac{V_{i3}}{6}-\frac{V_{i2}}{3})]\overline{\overline{G_c}}\end{aligned} \tag{3.1}$$

There are two primary objectives in the design of the BMAA shown in Fig. 3.1(a). The first aim is to design the external coupling network to ensure that the maximum available power is extracted from each antenna element. In other words, the power at the outputs $O_1 - O_3$ should be as high as the maximum available power from each individual antenna element in the array (obtained when each antenna is impedance matched individually for maximum power transfer). The second objective is to maximize the phase difference between each two output (e.g., $\angle V_{o1} - \angle V_{o2}$ or $\angle V_{o1} - \angle V_{o3}$ of the array compared to the input phase difference (e.g. $\angle V_{i1} - \angle V_{i2}$ or $\angle V_{i1} - \angle V_{i3}$). To accomplish this, however, a specific architecture for the external coupling network must first be chosen.

3.2.2 Proposed Three-Element BMAA Architecture

The proposed BMAA consists of three monopole antennas placed on the three corners of an equilateral triangle as shown in Fig. 3.2. Each monopole is connected to one input of a symmetric external coupling network having three inputs and three outputs. Fig. 3 shows the equivalent circuit model of the entire BMAA in which the monopole antennas are modeled with their Thevenin equivalent circuit models. The external coupling network is implemented entirely using passive reactive components (i.e., inductors and capacitors). Mutual coupling between the different antenna elements is taken into account using current dependent voltage sources. The proposed array is illuminated with a plane wave with an angle-of-incidence of θ as shown in Fig. 3.2(b). Considering reciprocity and symmetry, the

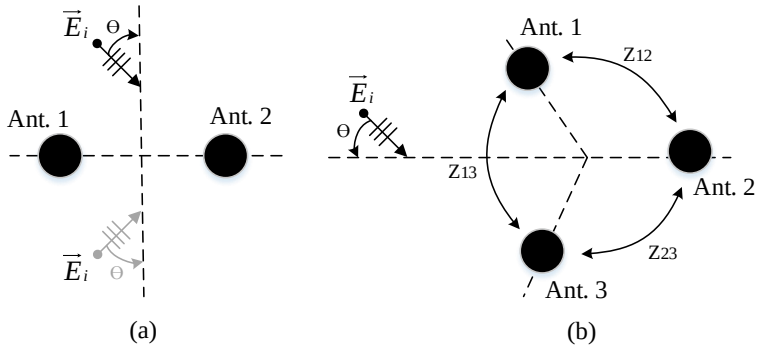

Figure 3.2: (a) A two-element antenna array has an inherent 180° ambiguity in its response as shown in the figure. (b) A three-element array with a triangular lattice solves this problem. This grid is used for the three-element BMAA considered in this work. In this work, the element spacing between the elements, d, is electrically small. i.e., $d << \lambda_0$.

Z parameters of the monopole antennas can be represented as

$$Z_a = \begin{bmatrix} Z_{11} & Z_{12} & Z_{12} \\ Z_{12} & Z_{11} & Z_{12} \\ Z_{12} & Z_{12} & Z_{11} \end{bmatrix} \tag{3.2}$$

Because of symmetry, $Z_{11}= Z_{22}= Z_{33}$ and $Z_{12}= Z_{23}= Z_{13}$ [49]. The circuit shown in Fig. 3.3 can be simplified for each linearly-independent mode of excitation of the array (Modes A, B, and C discussed in Section II-A) as shown in Fig. 3.4. This simplification is possible because of the rotationally symmetric architecture of the antenna elements and the external coupling network selected here. For these three simplified circuits, the network response can be represented as:

$$\begin{bmatrix} V_{o1}^A \\ V_{o2}^A \\ V_{o3}^A \end{bmatrix} = \begin{bmatrix} G_a & 0 & 0 \\ 0 & G_a & 0 \\ 0 & 0 & G_a \end{bmatrix} \cdot \begin{bmatrix} V_{i1}^A \\ V_{i2}^A \\ V_{i3}^A \end{bmatrix} \tag{3.3}$$

$$\begin{bmatrix} V_{o1}^B \\ V_{o2}^B \\ V_{o3}^B \end{bmatrix} = \begin{bmatrix} G_b & 0 & 0 \\ 0 & G_b & 0 \\ 0 & 0 & G_b \end{bmatrix} \cdot \begin{bmatrix} V_{i1}^B \\ 0 \\ V_{i3}^B \end{bmatrix} \tag{3.4}$$

$$\begin{bmatrix} V_{o1}^C \\ V_{o2}^C \\ V_{o3}^C \end{bmatrix} = \begin{bmatrix} G_{c11} & G_{c12} & 0 \\ G_{c12} & G_{c22} & G_{c12} \\ 0 & G_{c12} & G_{c11} \end{bmatrix} \cdot \begin{bmatrix} V_{i1}^C \\ V_{i2}^C \\ V_{i3}^C \end{bmatrix} \tag{3.5}$$

Based on the equations above and considering the principle of linear superposition, we can write:

$$\begin{aligned} V_{O1} = V_{o1}^A + V_{o1}^B + V_{o1}^C = (\frac{V_{i1} + V_{i2} + V_{i3}}{3})G^a + \\ (\frac{V_{i1} - V_{i3}}{2})G^b + (\frac{-V_{i2}}{3} + \frac{V_{i1} + V_{i3}}{6})G_{11}^c \\ +(\frac{2V_{i2}}{3} + \frac{V_{i1} + V_{i3}}{3})G_{12}^c \end{aligned} \tag{3.6}$$

$$\begin{aligned} V_{O2} = V_{o2}^A + V_{o2}^B + V_{o2}^C = (\frac{V_{i1} + V_{i2} + V_{i3}}{3})G^a + \\ (\frac{-V_{i2}}{3} + \frac{V_{i1}}{6} + \frac{V_{i3}}{6})G_{11}^c + (\frac{2V_{i2}}{3} - \frac{V_{i1} + V_{i3}}{3})G_{12}^c \end{aligned} \tag{3.7}$$

$$\begin{aligned} V_{O3} = V_{o3}^A + V_{o3}^B + V_{o3}^C = (\frac{V_{i1} + V_{i2} + V_{i3}}{3})G^a \\ +(\frac{-V_{i1} + V_{i3}}{2})G^b + (\frac{-V_{i2}}{3} + \frac{V_{i1} + V_{i3}}{6})G_{11}^c \\ +(\frac{2V_{i2}}{3} + \frac{V_{i1} + V_{i3}}{3})G_{12}^c \end{aligned} \tag{3.8}$$

Assuming that the three output ports of the BMAA are connected to 50 Ω loads, (6)-(8) can be used to calculate the output power of the BMAA. G^a, G^b, G_{11}^c and G_{12}^c can be easily calculated by analyzing the circuits shown in Figs. 3.4(a)-3.4(c). Explicit expressions for

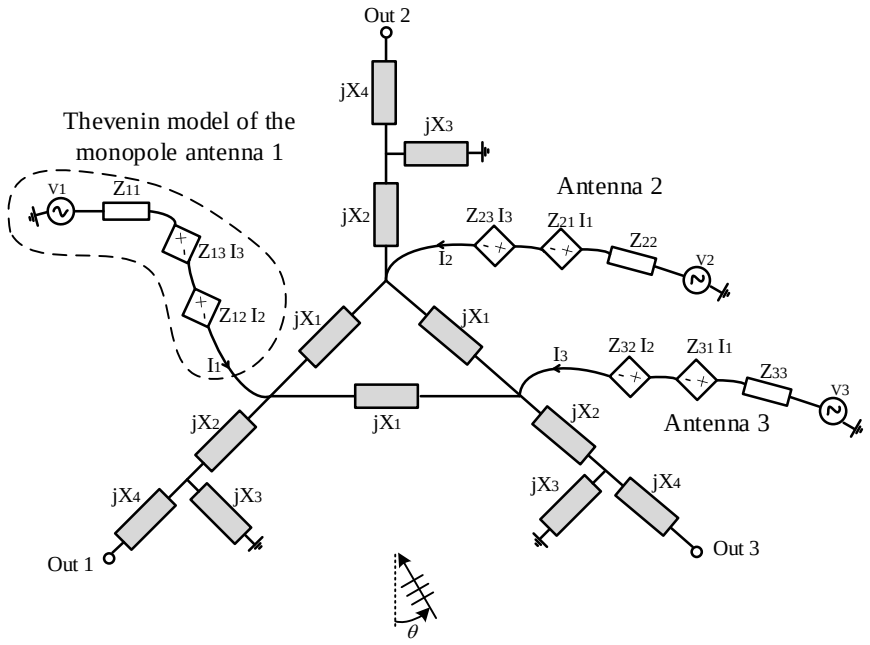

Figure 3.3: Equivalent circuit model of a three-element BMAA using a symmetrical architecture for its external coupling network. The antennas are modeled with their Thevenin circuit model (shown in white) and the external coupling network is shown in gray.

them are provided in Appendix A.

The second important output parameter of the BMAA is its phase enhancement factor. For a two-element BMAA, the phase enhancement factor is defined as $\eta = s/s_0$ where s_0 is considered as the slope of the output phase difference of a regular array (without coupling network) with respect to the angle of incidence at boresight and s is the slope of the output phase difference of the biomimetic array:

$$\eta = \frac{s}{s_0} = \lim_{\theta \to\ 0} \left(\frac{d\Phi_{out}}{d\Phi_{in}}\right) \tag{3.9}$$

where Φ_{out} is the output phase difference of the BMAA and $\Phi_{in} = kd\sin(\theta)$ is the phase difference that the EM wave experiences as it propagates between the two antenna elements with an incidence angle of θ from the boresight. In the present work, we expand this definition of the phase enhancement factor to the proposed three-element BMAA with a triangular lattice. Specifically, the slope of the output phase difference between elements 1

and 3, s_{13}, is defined as:

$$s_{13} = \lim_{\theta \to 0} (\frac{\angle V_{o1} - \angle V_{o3}}{\theta}) \tag{3.10}$$

Using the expressions for V_{o1} and V_{o3}, s_{13} can be written as:

$$s_{13} = \lim_{\theta \to 0} (\frac{1}{\theta}) \angle (\frac{V_{o1}^A + V_{o1}^B + V_{o1}^C}{V_{o3}^A + V_{o3}^B + V_{o3}^C}) \tag{3.11}$$

The slope of the output phase difference between the other two pairs of elements, s_{12} and s_{23}, are also defined in a similar way. Due to symmetry in the coupling network, we have:

$$\begin{aligned} V_{o1}^A &= V_{o3}^A = V_o^A \\ V_{o1}^B &= -V_{o3}^B = V_o^B \\ V_{o1}^C &= V_{o3}^C = V_o^C \end{aligned} \tag{3.12}$$

By substituting (12) in (11), s_{13} can be expressed as:

$$s_{13} = \lim_{\theta \to 0} (\frac{1}{\theta}) \angle (\frac{V_o^A + V_o^B + V_o^C}{V_o^A - V_o^B + V_o^C}) \tag{3.13}$$

Following the derivation provided in Appendix B, we have:

$$s_{13} = \lim_{\theta \to 0} (\frac{1}{\theta}) (\frac{2 \operatorname{Im}(\frac{V_o^B}{V_o^A})}{1 + \operatorname{Re}(\frac{V_o^C}{V_o^A})}) \tag{3.14}$$

$$s_{13} \approx \lim_{\theta \to 0} (\frac{2}{\theta}) |\frac{V_o^B}{V_o^A}| \sin(\alpha) \tag{3.15}$$

where

$$\alpha = \angle V_o^B - \angle V_o^A \tag{3.16}$$

Therefore, for a constant $|V_o^A|$, to have the maximum possible phase enhancement between

the outputs 1 and 3, s_{13}, two conditions should be considered. First, the output amplitude for the excitation mode B should be maximized and secondly, the phasors V_o^A and V_o^B should be 90° out of phase at broadside. Notice that maximizing s_{13} can also be done by minimizing V_o^A. However, this is not desirable since that is equivalent to sacrificing the output power level of the antenna. In fact, in BMAAs that do not extract maximum available power from an incoming wave such as those reported in [16] and [20], this is the main method of achieving a phase enhancement factor values larger than one.

Following the derivation provided in Section II-B of [21], the theoretical upper bound value for the phase enhancement factor between antenna elements 1 and 3 in terms of the [Y] parameters of the three-element antenna array is derived as:

$$\eta_{max_{13}} = \sqrt{\frac{\mathrm{Re}(Y_{11}) + \mathrm{Re}(Y_{13})}{\mathrm{Re}(Y_{11}) - \mathrm{Re}(Y_{13})}} \tag{3.17}$$

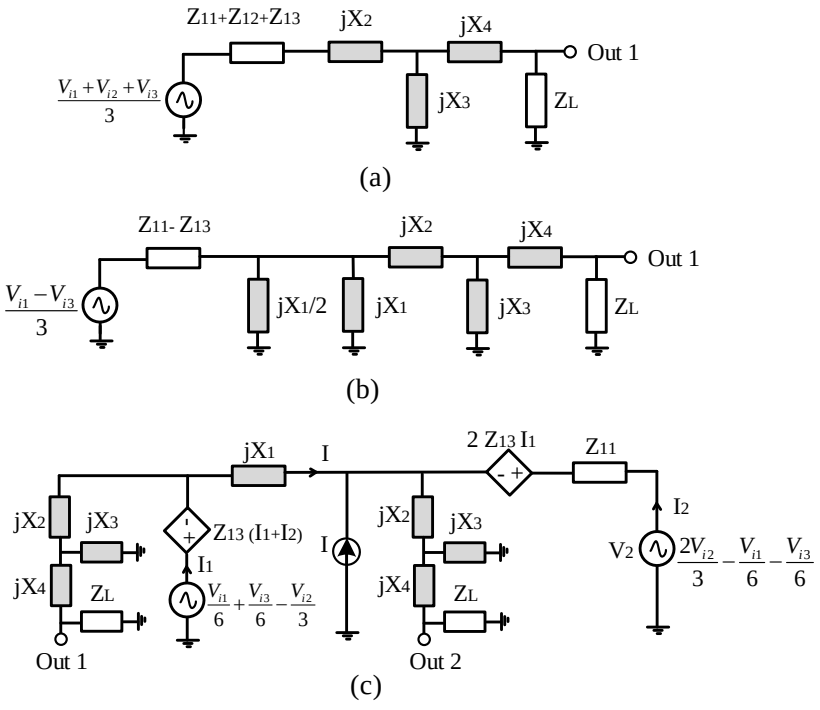

Figure 3.4: Simplified equivalent circuit models of the three-element BMAA shown in Fig. 3.3 for its three linearly-independent modes of excitation. (a) Mode A. (b) Mode B. (c) Mode C.

Table 3.1: The Y-parameters of the Three-Element Array of Monopoles with a Triangular Lattice Examined in Section III.

$G_{ii} = \mathrm{Re}(Y_{ii})$	1.79 $m\mho$
$G_{ij} = \mathrm{Re}(Y_{ij})$	1.16 $m\mho$
$B_{ii} = \mathrm{Im}(Y_{ii})$	-15.5 $m\mho$
$B_{ij} = \mathrm{Im}(Y_{ij})$	8.10 $m\mho$

This expression is only a function of the self and the mutual impedances between the elements of the array and does not depend on the architecture, type, or element values of the external coupling network. Therefore, the maximum possible phase enhancement factor achievable from any array (without sacrificing the output power level) can be easily calculated using a simple full-wave EM simulation of the array to determine its [Y] parameters. Based on (17) and the antenna admittance parameters reported in Table (I), $\eta_{max_{13}} = 4.68$ is obtained for the three-element monopole array considered in this paper. To achieve this phase enhancement factor in practice, however, a suitable external coupling network must be designed that can meet the aforementioned conditions on V_o^B and α.

3.3 Design Example and Experimental Results

To demonstrate the design procedure of the proposed three-element BMAA, an example is presented in this section. The BMAA is designed to operate at 600 MHz and consists of three, approximately quarter-wavelength monopole antennas placed on the corners of an equilateral triangle with side lengths of $0.05\lambda_0$. Each monopole is 13.5 cm long and separated from the other monopoles by 2.5 cm. In the simulations, the monopoles are assumed to be placed on an infinitely large ground plane. The three-port Y-parameters of the antennas, at the operating frequency of 600 MHz, are obtained from full-wave EM simulations in CST Studio and the results are presented in Table I. The element values of the external coupling network must be determined such that they satisfy the conditions discussed in Section II. To extract maximum power from an incoming wave incident from the boresight directions of any of the three pairs

(i.e. 0°, 120°, or 240°), mode A must be impedance-matched. As discussed in the previous section, the output voltage of mode B needs to be as large as possible to get the highest phase enhancement factor possible. The orthogonality between the outputs of mode A and mode B is another critical condition, which needs to be met. To satisfy these three conditions using the equivalent circuit models shown in Fig. 3.4, five nonlinear equations are obtained. These equations are provided in Appendix C. Four equations ((27)-(30) in Appendix C) correspond to the impedance-matching of the modes A and B. These equations are derived from the equivalent circuit models shown in Figs. 3.4(a) and 3.4(b). The fifth equation ((31) in Appendix C) corresponds to the orthogonality of the output voltages of modes A and B as labeled in Figs. 3.4(a) and 3.4(b). There is no guarantee that the nonlinear system of equations has a globally-optimum solution, or whether the solution results in practical values for the components of the coupling network. Therefore, a numerical optimization procedure was used to find an acceptable sub-optimal solution for component values which result in a practically implementable coupling network. This optimization procedure was carried out in Keysight Advanced Design System (ADS) to find the element values of the coupling network. To make sure that the optimization process results in component values that can be practically implemented[1], limitations on the range of component values of the external coupling network were set in the optimization procedure. These limitations span both negative and positive reactance values meaning that each component can be either an inductor or a capacitor. The optimization procedure was a random optimization with 15000 iterations. The element values for the external coupling network obtained using this process are listed in Table II.

To experimentally verify this design, a prototype of the proposed BMAA was fabricated. The three monopole antennas are made out of hollow copper tubes with circular cross sections with inner and outer radii of respectively 1.8 mm and 2.4 mm. The antennas are mounted on

[1]For example, an external coupling network that uses very large capacitors and inductors is not a desirable one. Generally, these reactive components have large tolerances and low quality factors that can deteriorate the response of the overall system.

Table 3.2: The Component Values of the External Coupling Network of the Three-Element BMAA Discussed in Section III. Reactance Values of X_1, X_2, X_3 and X_4 Are Implemented by Reactive Loads of 2.21 pF, 37.36 nH, 1.43 pF, and 37.36 nH.

Element	Value (Ω)
X_1	-120.02
X_2	40.86
X_3	-185.49
X_4	140.84

a ground plane with physical dimensions of 60 cm $\times$ 60 cm. Fig. 3.5(a) shows a photograph of the three monopoles mounted on the finite ground plane. The measured self and mutual impedances of the monopole array are shown in Fig. 3.6. To minimize the impact of scattering and diffraction from the edges of the finite ground plane on the BMAA response, the edges of the ground plane are covered with thin absorbers (6.35 mm thick ECCOSORB LS-30/SS-3 absorbers manufactured by Emerson and Cuming). The external coupling network was fabricated on a 0.030" thick Rogers RO4003C substrate. A photograph of the fabricated external coupling network is shown in Fig. 3.5(b). The coupling network is implemented in microstrip technology. The inputs of the network are connected to three SMA connectors using through substrate vias. The monopole antennas are connected to the inputs of the coupling network using SMA adapters as can be observed from Fig. 3.5(c). The outputs of the BMAA are extracted from the outputs of the external coupling network shown in Figs. 3.5(b)-3.5(c).

Fig. 3.7 shows the simulated output phase responses of the BMAA as a function of the angle of incidence (between elements 1 and 3) and compares them with the phase response of a regular array with the same elements and spacing (i.e., the BMAA without the external coupling network). The simulations are performed using CST Microwave Studio to obtain the scattering parameters of the three-element array (without the external coupling network). Subsequently, the S parameters of the array were exported to ADS and used as part of a circuit simulation to calculate the response of the BMAA. The simulation results predict a phase enhancement factor of 2.5. Notice that this phase enhancement factor is

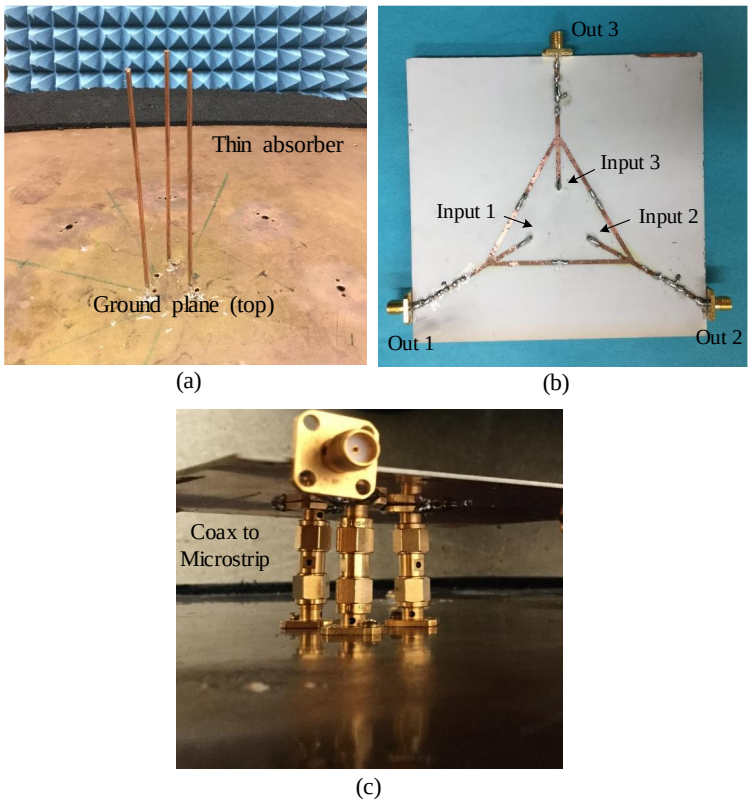

Figure 3.5: Photographs of the fabricated three-element biomimetic antenna array. (a) 3D view of the three monopoles. (b) The external coupling network. (c) The antenna array is connected to its external coupling network using SMA connectors and adapters.

different from the maximum theoretical value of 4.63 predicted from the theoretical analysis presented in Section II. This is attributed to two reasons. First, the optimization process used to obtain the element values of the external coupling network is not guaranteed to return a global optimum value for the elements of the coupling network. Secondly, the [Y] parameters of the antenna used in these experiments are different from those used in the calculations reported in Section II. Specifically, the use of the SMA connectors (for the antenna and the coupling network) and the SMA adapters used to connect the antenna and the coupling network together changes the [Y] matrix of the "effective" antenna as seen from the inputs of the external coupling network. Therefore, the maximum theoretically achievable phase enhancement factor in this case will be different from that predicted in Section II. Specifically, using the measured values of the Y-parameters of the antennas (including the

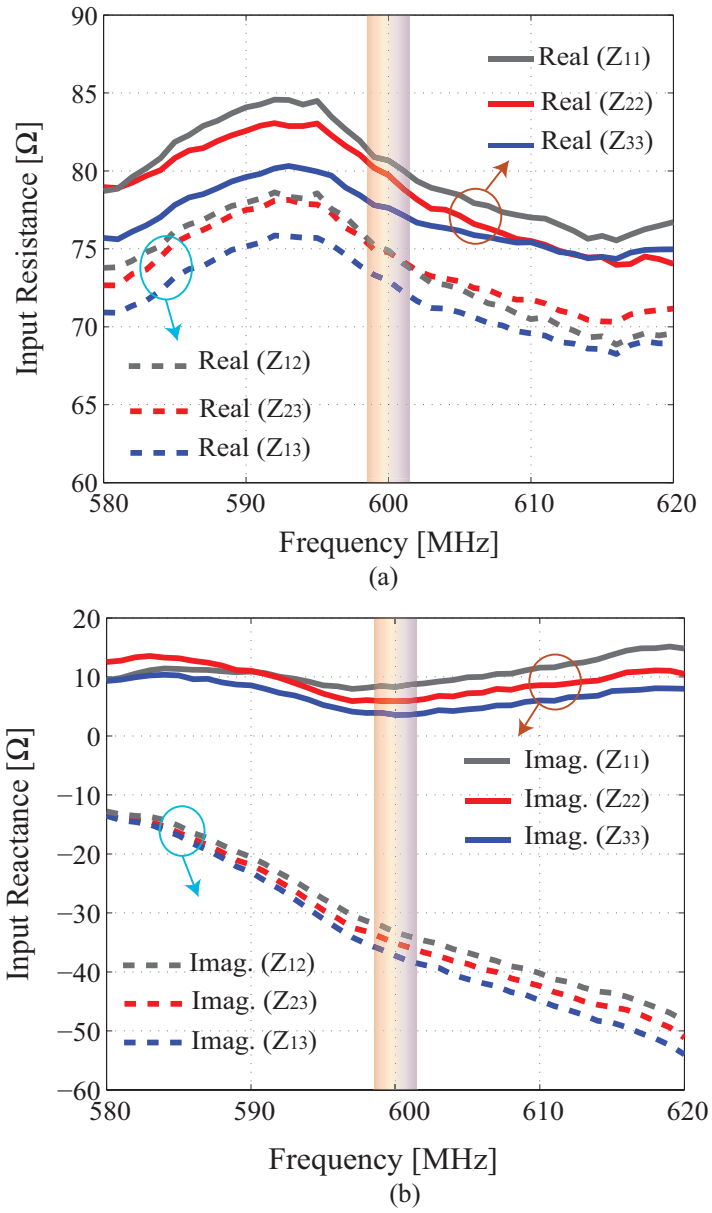

Figure 3.6: Measured input impedance of the monopole array discussed in Section III. The monopoles are approximately a quarter wavelength each, are designed to operate at 600 MHz, and are separated from one another by a distance of 2.5 cm: (a) Real part, (b) Imaginary part. The frequency band of operation of the BMAA is highlighted in the figure.

SMA connectors and adapters), the maximum phase enhancement factor achievable from this antenna is calculated as $\eta_{13max} = 2.2$[2].

[2]Notice that the phase enhancement factor of 2.5 is larger than this maximum value. This is due to the fact that the impact of the connectors and connecting transmission lines of the BMAA's external coupling network on the Y-matrix of the "effective" antenna are not taken into account there.

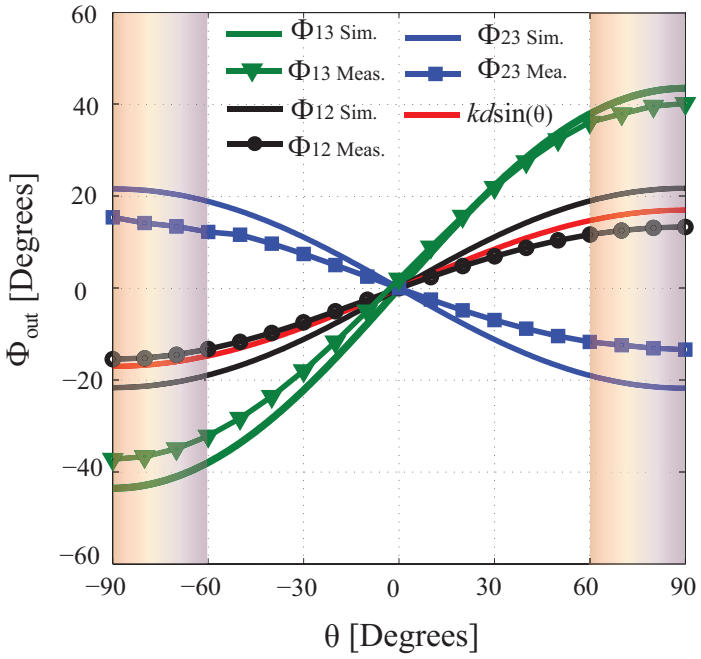

Figure 3.7: Measured and simulated output phase responses of the three-element BMAA as well as the phase response corresponding to the propagation of an electromagnetic wave over a distance of d at an angle of θ. The output phase difference of the BMAA has a higher rate of change for $|\theta| < 60°$ compared to $60° < |\theta| < 90°$ that is highlighted in the figure.

The response of the fabricated BMAA was measured using a calibrated 4-port vector network analyzer (Agilent PNA N5225A). The array is characterized by illuminating the BMAA with a vertically polarized plane wave from various incidence angles in the azimuth plane and measuring the three output signals of the BMAA. The measurement system consists of a transmitting dipole antenna and the receiving BMAA was placed in the far-field of the dipole. Fig. 3.7 shows the measured output phase difference between output ports 1 and 3 of the BMAA and compares that with the simulation results. Observe that a good agreement between the measurement and simulation results is obtained and the measured phase enhancement factor is 2.2, which is very close to the simulated phase enhancement factor of 2.5. As can be seen in Fig. 3.7, for incidence angles in the range of $-90° < \theta < 90°$, the output phase difference between the ports 1 and 3 of the BMAA (which are the desired outputs in this range) has a higher rate of change for $|\theta| < 60°$ compared to $60° < |\theta| < 90°$.

In the context of a direction finding system using only these two elements, this larger phase variation offers a better angular sensitivity for signals arriving with incidence angles less than $\pm 60^\circ$ range and this resolution decreases as the incidence angle increases. However, the rotational symmetry of the proposed BMAA and the fact that three elements are used along a triangular lattice address this problem. This scenario is shown in Fig. 3.8 where the measured and simulated output phase responses of the array are presented in the entire -180° to 180° range. Observe that in the range of -180° to -60°, the phase difference between elements 2 and 3 shows the maximum rate of change. As the incidence angle is increased, the maximum rate of change is shifted to the outputs 1 and 3 for the incidence angle range of -60° to $+60^\circ$ and the to outputs 1 and 2 for the incidence angles ranging from 60° to 180°.

Fig. 3.9 shows the measured and simulated power levels at the three outputs of the BMAA normalized to the available power level that can be achieved from a regular antenna array using the same elements and spacing (i.e., the BMAA without the coupling network). As can be observed, there is good agreement between the measured and simulated results. Moreover, the output power level of the BMAA is not sacrificed compared to that of the regular array. The minor discrepancies observed between the measurement and the simulation results can be attributed to the tolerances of the component values of the capacitors and inductors, slight asymmetries existing in the fabricated array and its external coupling network, potential measurement uncertainties, and the finite size of the ground plane, which was assumed to be infinite in the simulations.

It is noted that the proposed BMAA has a relatively narrow phase enhancement factor bandwidth. The simulated bandwidth of the BMAA presented in this work is 10 MHz. The narrowband response of the BMAA can be explained by examining the quality factor of the array for the different linearly-independent modes of excitation. Specifically for the common mode (Mode A), the array has a relatively low Q. For the non-common modes of excitation (Modes B and C), however, the out of phase excitation of the closely-spaced

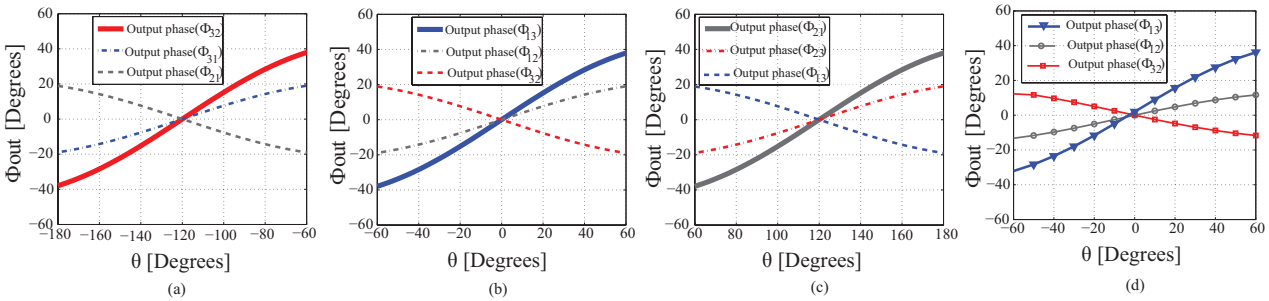

Figure 3.8: Phase responses of the proposed three-element BMAA. Output phase difference between ports 1 and 3 are similar to that of ports 1 and 2, except for a 120° phase shift. Therefore, the insensitive region of output phase difference curve for elements 1 and 3 ($60° < \theta < 90°$) overlaps the sensitive region of the phase difference curve for elements 1 and 2. (a) Simulated results for $-180° < \theta < -60°$, (b) Simulated results for $-60° < \theta < 60°$, (c) Simulated results for $60° < \theta < 180°$, and (d) Measured results for $-60° < \theta < 60°$.

antennas results in significant increase in the stored energy within the near field of the array, which results in increasing the Q of these modes. This high Q manifests itself in the form of rapid changes of the mutual coupling terms of the array (e.g., $Y_{1,2}$, $Y_{1,3}$, and $Y_{2,3}$) as a function of frequency. Following (17), this results in having a limited bandwidth over which a desired phase enhancement factor may be achieved. For a given lattice shape and element spacing, the choice of the antenna element (e.g. monopole, bow-tie, loop, etc.) does impact this achievable bandwidth to some extent. However, since the primary factor limiting this bandwidth is the electrically-small lattice spacing of the array, all of these BMAAs are expected to be narrowband having bandwidths in the range of 1%- 5%. In such BMAAs, using non-Foster coupling networks may offer a means of increasing the bandwidth of the array. A recent study in [20] has examined a non-Foster BMAA. However, in that design, phase enhancement is obtained by sacrificing the output power level of the array, which is not desirable. Theoretical studies and simulation results of a non-Foster BMAA that does not sacrifice the output power level of the array have been reported in [45] and suggest the feasibility of this idea. This structure, however, is yet to be fabricated and tested.

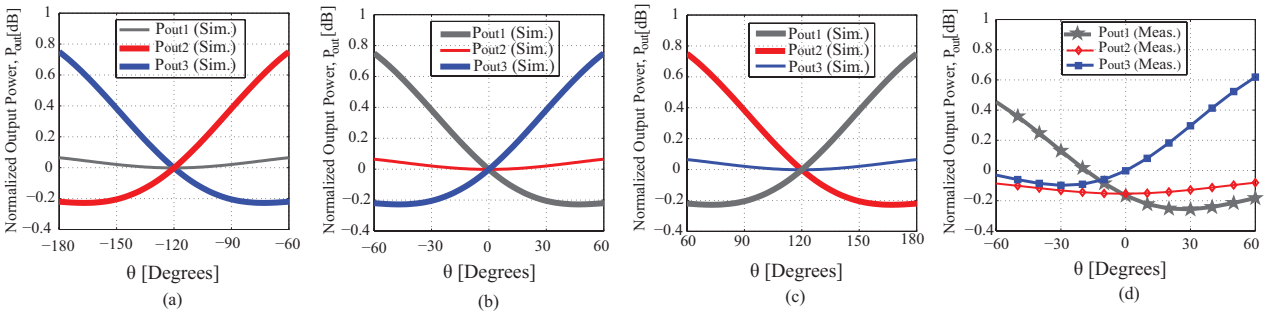

Figure 3.9: Measured and simulated amplitude responses of the proposed three-element BMAA. (a) Simulated results for $-180° < \theta < -60°$, (b) Simulated results for $-60° < \theta < 60°$, (c) Simulated results for $60° < \theta < 180°$, and (d) Measured results for $-60° < \theta < 60°$.

3.4 Conclusions

A biomimetic antenna array with three mutually-coupled elements placed on the corners of an electrically-small equilateral triangle was introduced in this work. The antenna was analyzed using its equivalent circuit model and a modal analysis technique, which examines the structure separately in each of its three linearly independent modes of operation. This three-element BMAA was designed to meet two specific goals of maximum power extraction and nearly-maximum phase enhancement factor without sacrificing the output power level of the array. Specifically, the external coupling network of the array is designed such that the array can extract the maximum available power from an incoming wave. This is similar to what is performed in conventional antenna arrays and ensures that the output power level of the array is maximized. In addition to this, the external coupling network of the BMAA was also designed to maximize the output phase difference between each two elements of the array compared to what is achievable from a conventional antenna array. This phase enhancement factor increases the sensitivity of the BMAA to changes in the direction of arrival of the electromagnetic wave compared to a conventional antenna array. A prototype of this three-element BMAA consisting of three quarter-wavelength-long monopoles separated from each other by a distance of $0.05\lambda_0$, where λ_0 is the free-space wavelength, was also designed, fabricated, and experimentally characterized. Experimental results were shown to be in good

agreement with the theoretically predicted ones. The proposed antenna addresses some of the shortcomings of the previously-reported two- [15]- [48] or three-element [19] BMAAs for applications such as small-aperture direction finding systems.

3.5 Appendix I

In Section II-B, the element values of the matrices in (3)-(5) can be calculated by analyzing the circuits shown in Figs. 3.4(a)-3.4(c). These values are obtained in terms of the parameters of the external coupling network as well as the Z parameters of the three-element monopole array:

$$G_a = \frac{Z_L}{[(jX_4 + Z_L) \parallel jX_3] + (Z_{11} + Z_{12} + Z_{13}) + (jX_2) - \dfrac{jX_3}{(Z_L + jX_4 + jX_3)}}. \tag{3.18}$$

$$G_b = \frac{Z_L}{(Z_{11} - Z_{13}) + [[(Z_L + jX_4) \parallel jX_3] + jX_2] \parallel [jX_1/2 \parallel jX_1] - \dfrac{(jX1/2 \parallel jX_1)}{(jX1/2 \parallel jX_1) + jX_2 + (jX_3 \parallel (jX_4 + Z_L))} - \dfrac{jX_3}{(Z_L + jX_4 + jX_3)}}. \tag{3.19}$$

$$G_{c11} = \frac{[(Z_{11} - A)(jX_1 + Z_{13} + 2A) - (Z_{13} - A)(2A + 2Z_{13})]}{\det \begin{pmatrix} A + Z_{13} & Z_{13} & Z_{13} \\ 2Z_{13} & Z_{13} - A & 2Z_{13} + 2A \\ Z_{13} & Z_{13} - A & jX_1 + Z_{13} + 2A \end{pmatrix} - \dfrac{Z_L\, jX_3}{jX_3 + jX_4 + Z_L}}. \tag{3.20}$$

where $A = [(Z_L + jX_4) \parallel jX_3] + jX_2$

3.6 Appendix II

Based on (13), the slope of the output phase difference between elements 1 and 3, i.e. $s_{13} = d\Phi_{out,13}/d\theta$, is defined as:

$$s_{13} = \lim_{\theta \to 0}(\frac{1}{\theta})\angle(\frac{V_o^A + V_o^B + V_o^C}{V_o^A - V_o^B + V_o^C}) \tag{3.21}$$

Since mode B is a non-common mode, for incidence angles near broadside (i.e., $\theta \to 0$), $\mathrm{Re}(V_o^B/V_o^A)$ tends to zero. Then, we have:

$$s_{13} = \lim_{\theta \to 0}(\frac{1}{\theta})\angle(\frac{1 + \mathrm{Re}(\frac{V_o^C}{V_o^A}) + j(\mathrm{Im}\,\frac{V_o^C}{V_o^A} + \mathrm{Im}\,\frac{V_o^B}{V_o^A})}{1 + \mathrm{Re}(\frac{V_o^C}{V_o^A}) + j(\mathrm{Im}\,\frac{V_o^C}{V_o^A} - \mathrm{Im}\,\frac{V_o^B}{V_o^A})}) \tag{3.22}$$

By using (23), s_{13} is simplified as:

$$\begin{aligned} s_{13} = \lim_{\theta \to 0}(\frac{1}{\theta})[\tan^{-1}(&\frac{\mathrm{Im}(\frac{V_o^C}{V_o^A}) + \mathrm{Im}(\frac{V_o^B}{V_o^A})}{1 + \mathrm{Re}(\frac{V_o^C}{V_o^A})} - \\ &\tan^{-1}(\frac{\mathrm{Im}(\frac{V_o^C}{V_o^A}) - \mathrm{Im}(\frac{V_o^B}{V_o^A})}{1 + \mathrm{Re}(\frac{V_o^C}{V_o^A})})] \end{aligned} \tag{3.23}$$

$$s_{13} = \lim_{\theta \to 0}(\frac{1}{\theta})(\frac{2\,\mathrm{Im}(\frac{V_o^B}{V_o^A})}{1 + \mathrm{Re}(\frac{V_o^C}{V_o^A})}) \tag{3.24}$$

Since mode C is a non-common mode, for incidence angles near broadside (i.e., $\theta \to 0$), $\mathrm{Re}(V_o^C/V_o^A)$ tends to zero. Then, we have:

$$s_{13} \approx \lim_{\theta \to 0}(\frac{2}{\theta})|\frac{V_o^B}{V_o^A}|\sin(\alpha) \tag{3.25}$$

where

$$\alpha = \angle V_o^B - \angle V_o^A \tag{3.26}$$

3.7 Appendix III

In Section (III), four nonlinear equations correspond to the impedance-matching of the modes A and B are listed here:

$$\mathrm{Re}[Z_{11} + Z_{12} + Z_{13}] = \mathrm{Re}[[(Z_L + jX_4) \parallel jX_3] + jX_2] \tag{3.27}$$

$$\mathrm{Im}[Z_{11} + Z_{12} + Z_{13}] = -\mathrm{Im}[[(Z_L + jX_4) \parallel jX_3] + jX_2] \tag{3.28}$$

$$\mathrm{Re}[Z_{11} - Z_{13}] = \mathrm{Re}[[(Z_L + jX_4) \parallel jX_3] + jX_2] \parallel jX_1 \parallel jX_1/2 \tag{3.29}$$

$$\mathrm{Im}[Z_{11} - Z_{13}] = -\mathrm{Im}[[(Z_L + jX_4) \parallel jX_3] + jX_2] \parallel jX_1 \parallel jX_1/2 \tag{3.30}$$

The phasors of V_o^B and V_o^A should be orthogonal to each other at boresight.

$$\angle V_o^B \perp \angle V_o^A \tag{3.31}$$

Chapter 4

Capacity-Enhancement in MIMO Systems Using Biomimetic Electrically-Small Antenna Arrays

The full manuscript was published as:

M. Ranjbar Nikkhah, M. Panahi, H. Luyen, H. R. Bahrami and N. Behdad, "Capacity-Enhancement in MIMO Systems Using Biomimetic Electrically-Small Antenna Arrays," *IET Microwaves, Antennas and Propagation*, vol. 12, no. 13, pp. 2001-2006, Oct. 2018.

4.1 Introduction

Beamforming using directional antenna arrays can improve the capacity and performance of multi-input multi-output (MIMO) communication systems by increasing the gain and reducing the cross correlation of wireless channel links. However, the performance of conventional antenna arrays is limited by the physical dimensions of the array elements, especially when the element spacing is reduced below $\lambda_0/2$, where λ_0 is the free-space wavelength. It is well known that for a beamformer to provide an acceptable spatial filtering, the antenna spacing should be in the order of $\lambda_0/2$ [22, 23]. The reliance on large antenna spacing results in large array sizes, especially at frequencies below 5 GHz where the propagation conditions are most suitable for achieving wide-area coverage that many mobile wireless communication systems rely on. Over the years, a number of studies have examined the performance of MIMO systems that use electrically-small or compact antenna arrays at the transmitter and/or the receiver [24, 25]. The impact of antenna correlation in small receiving terminals on the capacity of MIMO systems is studied theoretically and experimentally [24]. The theory of characteristic modes has been employed to design MIMO antennas that exploit the resonant modes of the platform to obtain different radiation patterns [25]. A reconfigurable antenna array based on electronically-steerable parasitic array radiator technique was used in [26] to improve the MIMO channel capacity of the conventional array. Finally, a number of theoretical studies have examined the role that superdirectivity can play in enhancing the capacity of MIMO systems employing superdirective antenna arrays [27–29].

The concept of superdirectivity in arrays with electrically-small spacing between the elements has been investigated for many years [1–3, 50]. These studies suggest that achieving superdirectivity from an electrically small array is possible in theory. However, implementing a superdirective antenna array with electrically-small aperture dimensions is extremely challenging. This is caused by the highly-oscillatory and widely-varying excitation coefficients needed to achieve superdirective radiation patterns. Important aspects of the superdirective

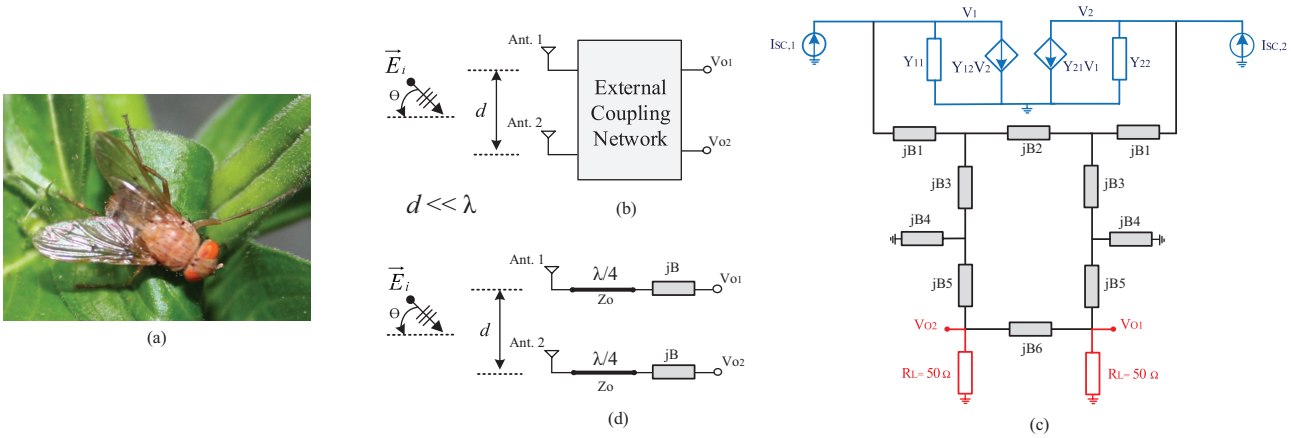

Figure 4.1: (a) Photograph of *Ormia Ochracea* courtesy of Prof. Bill Cade at the University of Lethbridge. (b) Block diagram of a two-element biomimetic antenna array. (c) Equivalent circuit model of a two-element biomimetic antenna array taking into account the mutual coupling effects between the two antennas. $I_{sc1}(\theta) = e^{j\alpha}$ and $I_{sc2}(\theta) = e^{-j\alpha}$ where $\alpha = \pi d \sin(\theta)/\lambda$. The parts of the circuit shown in gray are the elements of the external coupling network. Blue and red represent respectively the equivalent circuit of the two-element antenna array and the 50 Ω outputs. (d) Block diagram of a two-element regular antenna array using the same monopole elements and the same spacings. The regular antenna array uses an impedance matching network consisting of a quarter-wavelength transmission line and a series reactive element.

arrays have been investigated including endfire superdirective array design using parasitic elements [6], increasing the operating bandwidth by means of active elements [5] and loss issues in these types of arrays [4]. To control the strong mutual coupling in such small arrays, various techniques have been reported including the use of wideband decoupling networks using resistive elements [11], using reactively loaded dummy elements [51], inserting a slot in the ground plane [52], and mode decomposition method to diagonalize the S-parameters of coupled arrays [9]. The effects of mutual coupling in electrically-small arrays have been rigorously studied in [7, 8, 10]. Finally, the application of electrically-small antenna arrays in MIMO systems and beam forming networks have been thoroughly investigated recently [30, 31].

Electrically-small antenna arrays are also used in development of small-aperture direction finding systems [13,14]. Recently, the concept of electrically-small biomimetic antenna arrays (BMAAs) was proposed as a means of enhancing the sensitivity of direction finding systems

with small aperture dimensions [15, 16, 20, 21, 53]. In electrically-small BMAAs, a number of closely-spaced antenna elements are connected together using an appropriate external coupling network (ECN) [16]. The role of the ECN is to extract the maximum available power from all linearly-independent excitation modes of the array. Furthermore, the ECN can convert the small phase differences between the received signals at its input (antenna terminals) to larger phase differences at its outputs.

In this paper, we study the impact of employing biomimetic antenna arrays in increasing the achievable capacity of MIMO communication systems. Unlike conventional arrays, BMAAs are designed to extract the maximum available power from all linearly-independent modes of excitation of the array. This allows a small-aperture BMAA to achieve significantly larger directivity and gain values compared to its traditional array counterpart with the same aperture dimensions. When used as part of a MIMO communications system, this allows for enhancing the system capacity without increasing the antenna size or spacing. In particular, we demonstrate the capacity enhancement that can be achieved using BMAAs in comparison with conventional antenna arrays using the same two monopole elements and having the same spacing. Furthermore, we also demonstrate that the capacity of a MIMO communication system that uses an electrically-small BMAA, is comparable with that of a system that uses a conventional array with significantly larger element spacing. These studies are performed by designing prototypes of a two-element BMAA and a conventional array operating in the UHF band. The performances of these antennas as part of a MIMO system are evaluated using numerical simulations. Prototypes of these antennas are also fabricated and used to perform experiments in an emulated environment.

4.2 Comparison of a Two-Element BMAA and a Regular Two-Element Array

The parasitoid fly, *Ormia Ochracea* (shown in Fig. 4.1(a)), has hyperacute sense of directional hearing despite having an extremely-small acoustic receiving aperture [17]. Electrically-small antenna arrays based on the hearing mechanism of *O. Ochracea* have recently been reported [15,16,21]. Fig. 4.1(b) shows the simplified block diagram of a two-element BMAA. The device consists of two receiving antenna elements with an element spacing of $d << \lambda_0$ where λ_0, is the free-space wavelength of electromagnetic waves. These antennas are connected to an external coupling network and the outputs of the array (V_{o1} and V_{o2}) are extracted from the outputs of this ECN. A two-element antenna array has two linearly-independent modes of excitation. These include the common and the differential modes, where the two elements are respectively excited with excitation coefficients of $(1, 1)$ and $(1, -1)$. When the array is illuminated with a plane wave arriving from a direction other than the boresight, the voltages induced on the antenna terminals can be expressed as a superposition of the common and the differential modes of excitation. For electrically-small spacing between the elements, $d << \lambda_0$ and most of the power of the incoming wave is contained in the common-mode excitation and a small portion of the incident power is contained in the differential mode. In such arrays, however, the differential mode contains most of the information about the direction of arrival of the incoming wave. Therefore, to increase the sensitivity of the array to the direction of arrival of the EM wave, the external coupling network of the array is designed to extract the maximum available power from both the common and the differential modes of excitation [21]. Furthermore, the external coupling network is designed to create a 90° phase difference between the output voltages of the array in the common and differential modes [21]. This latter condition ensures that the output phase difference of the array $\Phi_{out} = \angle V_{o2} - \angle V_{o1}$ is enhanced compared to the input phase difference of $\frac{2\pi}{\lambda} d \sin\theta$. This is important if such arrays are to be used to perform direction

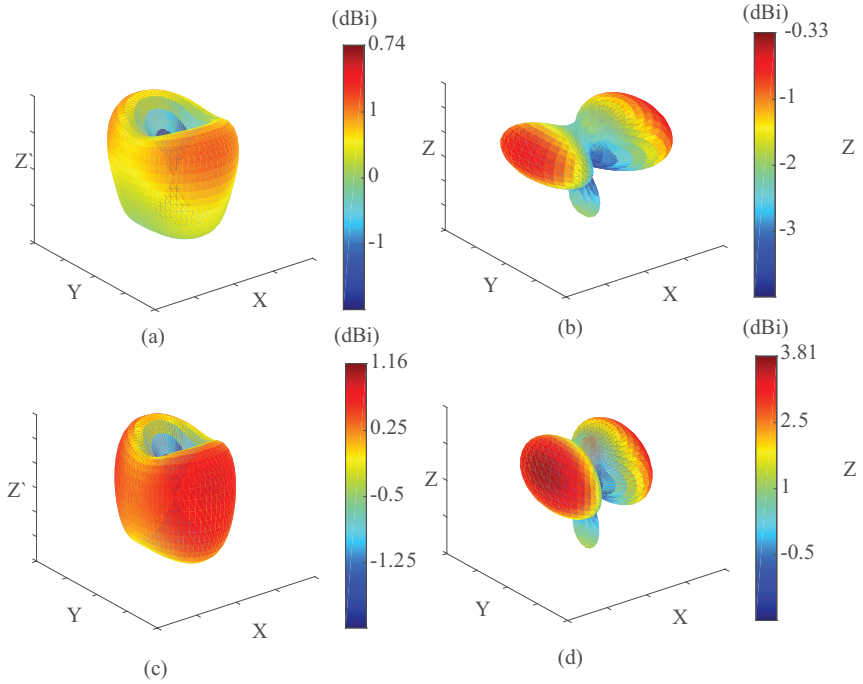

Figure 4.2: Full-wave simulated radiation patterns of the regular antenna array and those of the two-element BMAA discussed in the paper. The radiation patterns show the three-dimensional realized gains of the antenna. (a) Regular array for common-mode excitation. (b) Regular array for differential mode excitation. (c) BMAA for common-mode excitation. (d) BMAA for differential mode excitation. Observe that in both of these cases, the BMAA has a higher realized gain compared to the regular array. The enhanced realized gain value is particularly significant for the differential mode of excitation and shows an increase of approximately 4 dB.

finding using phase interferometry. For small antenna element spacing, the array presents significantly different impedances for these two excitation modes. In a conventional receiving array, each element of the array is impedance matched individually. In the receiving mode, such arrays can only extract maximum available power from the common mode of excitation for small spacing between the elements of the array. Therefore, such arrays cannot provide the same level of directional sensitivities that a two-element BMAA can offer. Fig. 4.1(c) shows the equivalent circuit model of a two-element BMAA. In this model, the antennas are modeled with their Norton equivalent circuit models and the external coupling network uses six reactive elements ($B_1 - B_6$). This BMAA architecture was reported in [21] and is adopted in this work for the subsequent investigations.

4.3 Design of a Two-Element Biomimetic Antenna Array

In this section, we design a two-element BMAA consisting of two quarter-wavelength monopole antennas, each 10 cm long, placed at a distance of 4.8 cm apart (spacing of $0.1\lambda_0$). The antennas are designed to operate at 615 MHz and are placed on a finite ground plane with dimensions of 30 cm $\times$ 30 cm. The two-port Y-parameters of the proposed small antenna array are simulated and the results are presented in Table I. To extract the maximum power from an incoming wave incident from an arbitrary direction, the array must be matched in the common and the differential modes. The orthogonality between the output voltages of the common mode and the differential mode is another design condition that must be met [21]. These conditions were defined as goals of an optimization procedure used to determine the element values of the external coupling network of the BMAA. This optimization procedure was carried out using the built-in optimization engine of the circuit simulation software Keysight Advance Design System (ADS). Three goals were defined in this optimization process. The first and second goals were defined to satisfy the common mode and differential mode impedance matching conditions. The third goal was that the phase difference between the output voltages of the common and differential mode must be equal to 90°. To ensure that the optimization process results in a practically-realizable circuit, a few limitations were set on the range of the values of the reactive elements constituting the external coupling network of the BMAA. Specifically, the element values were allowed to be either positive or negative (capacitive or inductive) and B_i range was set between (-0.05 $\mho$ < B_i < 0.05 $\mho$). The optimization procedure was a random optimization with 5000 iterations and the convergence error achieved was less than 10^{-4}. The values of the reactive elements of the external coupling network were calculated by following the procedure discussed and are listed in Table II. Following the completion of the optimization process and determining the values of the external coupling network of the BMAA, the response of the external coupling

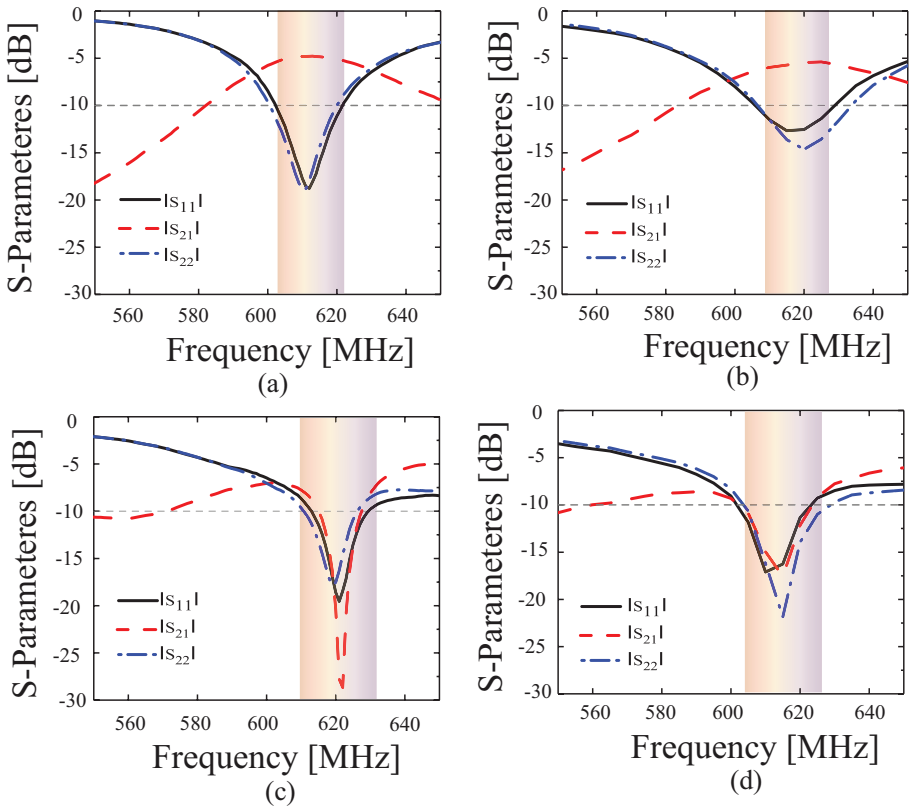

Figure 4.3: Measured and simulated S-parameters of the regular array and those of the two-element BMAA considered in this paper. (a) Regular array simulations. (b) Regular array measurements. (c) BMAA simulations. (d) BMAA measurements.

network was simulated in Keysight ADS and its four-port scattering (S) parameters were calculated. Subsequently, the calculated S-parameters of the external coupling network were exported in Touchstone format as a S4P file to CST Microwave Studio. CST Microwave Studio was used to perform full-wave electromagnetic simulation of the two monopole antennas. The overall response of the BMAA was simulated using an electromagnetic/circuit co-simulation in CST Studio using the full-wave EM simulations of the two monopole antennas and the four-port S-parameters of the external coupling network. Using this process, the S-parameters and the radiation patterns of the antenna were calculated.

Fig. 4.2 shows the comparison between the simulated radiation patterns of this antenna and those of a conventional two-element array where the same monopole elements having the same spacings are individually impedance matched as shown in Fig. 4.1(d). These

Table 4.1: The Y-parameters of the two-element array of monopole antenna used in the proposed BMAA calculated from full-wave EM simulations.

$G_{ii} = \mathrm{Re}(Y_{ii})$	28 $m\mho$
$G_{ij} = \mathrm{Re}(Y_{ij})$	7 $m\mho$
$B_{ii} = \mathrm{Im}(Y_{ii})$	-53 $m\mho$
$B_{ij} = \mathrm{Im}(Y_{ij})$	52 $m\mho$

Table 4.2: Element values of the external coupling network for the proposed BMAA.

Element	Value ($m\mho$)
B_1	38.6
B_2	11.6
B_3	-60.2
B_4	3.9
B_5	50.2
B_6	-6.2

patterns show the comparison between the realized gains of the BMAA and those of the conventional array in the common mode (Figs. 4.2(a) and 4.2(c)) and the differential mode (Figs. 4.2(b) and 4.2(d)). Observe that in both of these cases, the BMAA has higher realized gain compared to those of the regular array. The enhanced realized gain value is particularly significant for the differential mode of excitation and shows an increase of approximately 4 dB. This enhanced gain in the differential mode is a direct result of the design process in which the BMAA is designed to extract the maximum available power from all linearly-independent modes of excitation of the array. This allows for small-aperture BMAAs to achieve significantly larger directivity and gain values compared to their traditional array counterparts with the same aperture dimensions. The envelope correlation coefficient (ECC) parameter, calculated from the far-field radiation patterns over a sphere [54], at the operating frequency of 615 MHz for the BMAA was calculated as 0.35 and for the regular array was calculated as 0.57. The BMAA provides a lower ECC value, which corresponds to a larger channel capacity.

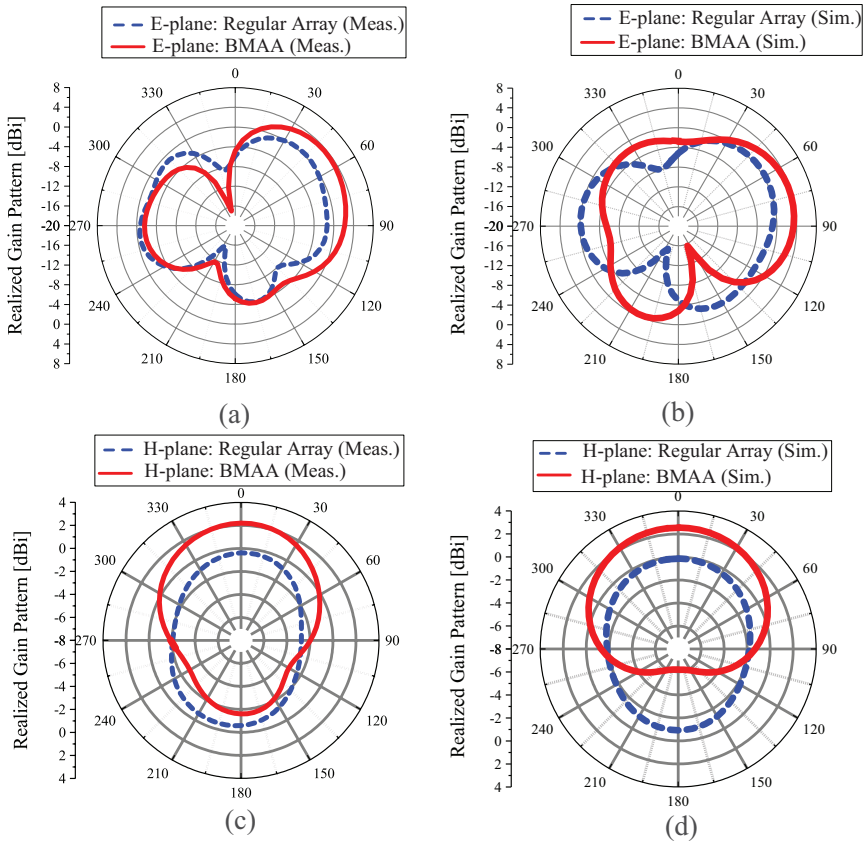

Figure 4.4: Measured and simulated E-plane and H-plane realized gains of the proposed two-element BMAA and those of the regular two-element array at 615 MHz for port 1 excitation and port 2 terminated with 50 Ω. (a) Measured E-plane patterns. (b) Simulated E-plane patterns. (c) Measured H-plane patterns. (d) Simulated H-plane patterns.

4.3.1 Measured Results

A prototype of this antenna and one of the regular array (the BMAA without the external coupling network) were fabricated and the fabricated prototypes were experimentally characterized. The external coupling network of the BMAA and the impedance matching network of the regular array are implemented in microstrip technology and were fabricated on a 0.030" thick Rogers RO4003C substrate with dielectric constant of 3.55. The two monopole antennas are made out of a copper tubes with a circular cross section radius of 3.2 mm. The monopole antennas are mounted on a finite ground plane made out of 2 mm-thick sheet of aluminium with dimensions of 30 cm × 30 cm. The elements B_1, B_2, B_3, B_4, B_5 and B_6 whose values are reported in Table II were implemented by capacitors and inductors

with values of 10 pF, 3 pF, 4.3 nH, 1 pF, 13 pF and 42 nH. The scattering parameters of the fabricated BMAA were measured using a calibrated two-port vector network analyzer (Agilent PNA N5225A) and its three-dimensional realized gain patterns were measured using the StarLab spherical near-field measurement system.

Measured and simulated S-parameters for the regular array and those of the proposed BMAA are presented in Fig. 4.3. In both cases, the element spacing is $d = \lambda/10$. The level of decoupling between the outputs of the BMAA is significantly increased compared to what is achieved from the regular array. According to [55, 56], S_{11} and S_{12} parameters of two output ports of a coupling network can be expressed as $S_{11} = (\Gamma_e + \Gamma_o)/2$ and $S_{21} = (\Gamma_e - \Gamma_o)/2$, where Γ_e and Γ_o are the output reflection coefficients for the equivalent circuits of the network in the even and odd modes. In other words, when the common-mode and differential-mode impedance matching conditions are satisfied ($\Gamma_e = \Gamma_o = 0$), the two antennas can be decoupled ($S_{12} = 0$). Fig. 4.4 shows the comparison between the measured radiation patterns of the two-element BMAA and those of the regular array. Observe that the measurement results also show that the BMAA has an enhanced gain compared to the regular array occupying the same aperture dimensions and using the same receiving elements. Fig. 4.5(a) shows a photograph of the two monopoles mounted on the finite ground plane and Fig. 4.5(b) illustrate the fabricated of the external coupling network of the proposed BMAA.

4.4 MIMO Capacity Evaluation

We studied the performance of MIMO links using the proposed two-element BMAA and compared them with the capacity of the systems using conventional two-element arrays. We assume that each transmit antenna is a half wavelength dipole with omnidirectional radiation pattern and at the receiver, either a two-element BMAA or a two-element conventional antenna array is used. In both cases, the spacing between the elements of the antennas at

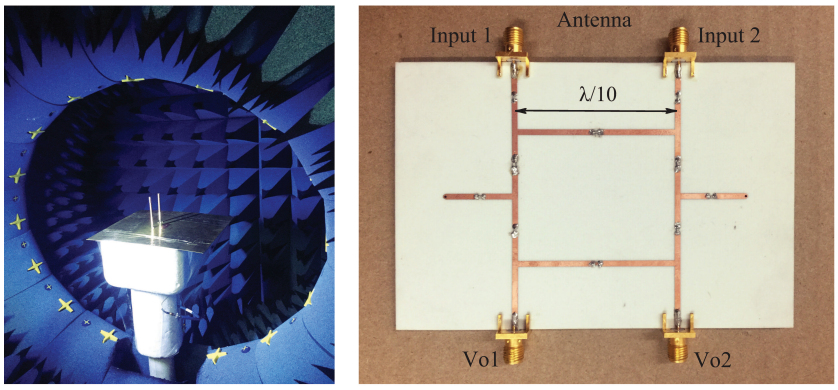

(a) (b)

Figure 4.5: Photographs of the measurement setup, the monopole array, and the fabricated external coupling network. (a) The near-field measurement setup used to measure the three-dimensional radiation patterns, gain, and efficiency of the two antennas. The two-element monopole array is shown at the center of the test chamber. (b) Photograph of the fabricated external coupling network of the two-element BMAA. Both BMAA and the regular array use two monopole antennas spaced at a distance of 48 mm (or equivalently $\lambda_0/10$). The element spacing between the elements, d, is electrically small. i.e., $d = \lambda/10$.

the receiver is $\lambda_0/10$.

MIMO system simulations were performed using a commercially-available tool (MIMObit 2.0) [57] and the channel capacity was estimated in these simulations. MIMObit software works with various propagation environments and uses plane wave decomposition to model the fields radiated from and received by the transmit and receive antennas. The S-parameters and three dimensional radiation patterns of the antenna were imported to MIMObit and used to model the receive antennas. Then, TGn-B propagation model [58] was chosen to model the propagation environment between the transmitter and the receiver. To estimate the channel capacity, the PropStats application was used from the different available solvers of MIMObit. PropStats application changes the propagation environment between the transmitter and receiver randomly each time the simulation is run. This is done up to the number of sample size parameter defined based on the chosen propagation model standards (TGn-B). In our simulations, the sample size parameter was set equal to 500. The cumulative distribution function of channel capacity was calculated by running this application for 500 samples of random instantiations of the propagation environment according to the TGnB model.

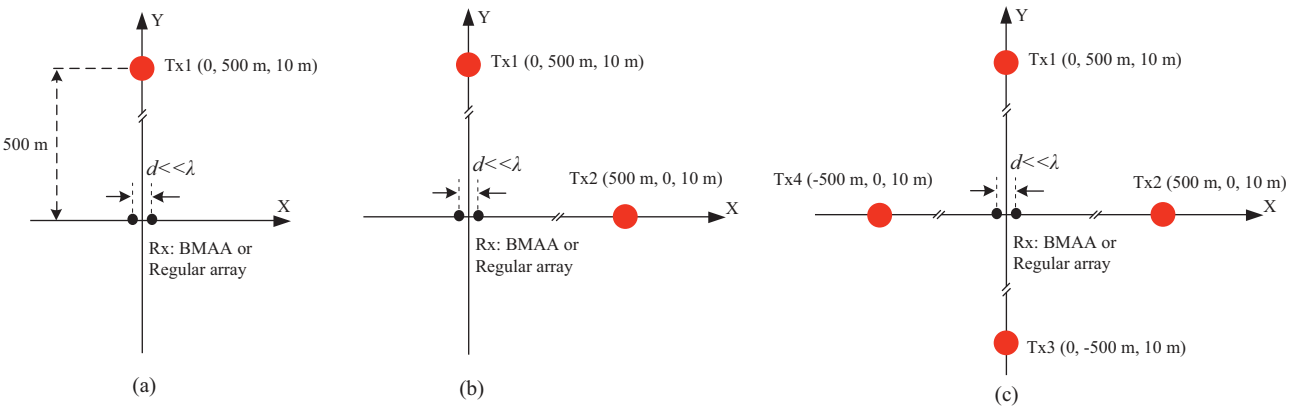

Figure 4.6: The locations of the transmitters and receiver in the MIMO systems studied in this paper. These include: (a) one, (b) two, and (c) four transmitter cases. Each transmitter has a single dipole antenna. The receiver includes the proposed BMAA or a conventional regular array. The transmit antenna is a half wavelength dipole with omnidirectional radiation pattern.

Two types of MIMO system modeling were performed. In the first case, the radiation patterns of the antenna were simulated in CST Studio and the results were exported to MIMObit to perform channel capacity estimation. In the second type of MIMO modeling, the three-dimensional field patterns of the BMAA and those of the regular array were measured using a spherical near-field system. The results were then reformatted to make the measurement data compatible with the format that MIMObit expects and they were imported in MIMObit and used to perform system level simulation to predict the channel capacity of a MIMO link using the measured antenna responses. In doing so, complete three-dimensional radiation patterns of the antennas (both magnitude and phase) were measured and used in MIMObit simulations. To include different transmit/receive antenna configurations in our comparison, three cases were studied based on the number of transmitters. The transmitter and receiver locations for three cases are shown in Fig. 4.6. In all cases, the distance between the transmitters (and receivers) from the ground is 10 m. As shown in Fig. 4.6, for all cases, the distance between the transmitter and the receiver is 500 m. To calculate the channel capacity, we assumed the transmitter power was equal to 0 dBm and the carrier frequency was 615 MHz. The capacity calculations were performed over 3% bandwidth.

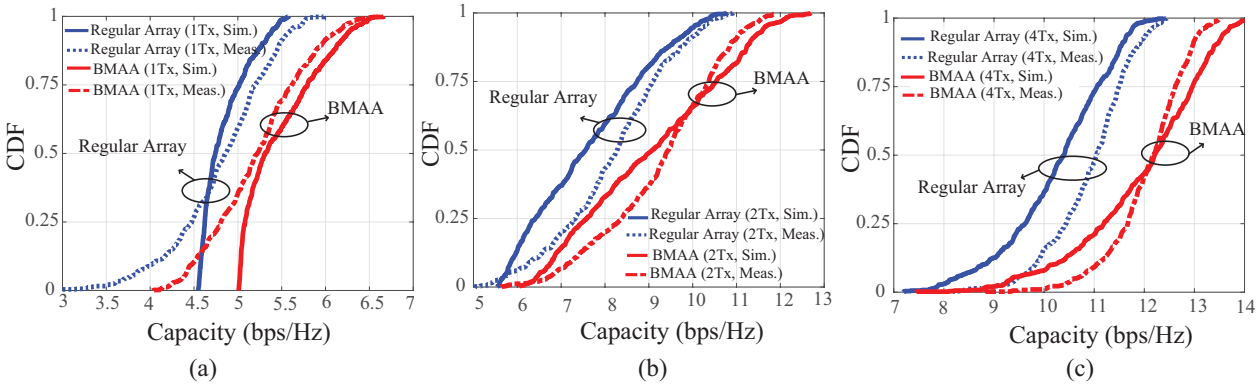

Figure 4.7: Comparison of the channel capacity of MIMO systems using BMAAs or conventional antenna arrays. (a) Simulated and measured cumulative distribution function (CDF) for one transmitter. (b) Simulated and measured CDF for two transmitters, (c) Simulated and measured CDF for four transmitters. The measurement results were obtained by measuring the complete three-dimensional realized gain patterns of the antennas and using them in MIMObit software to estimate the channel capacity as described in Section IV.

After running this application for 500 samples of random instantiations of the propagation environment according to the TGnB model, the cumulative distribution function of channel capacity over the sample of all the propagation environment instantiations were calculated for three cases and the results are shown in Fig. 4.7. By using the proposed BMAA, for the case of one transmitter, a channel capacity improvement of about 0.57 bit/s/Hz is obtained compared to the conventional regular array antenna as shown in Figs. 4.7(a). The amount of channel capacity enhancement is increased by increasing the number of transmitters. For the case of two transmitters shown in Fig. 4.6(b), channel capacity improvement about 1 bit/s/Hz is obtained in measurement and shown in Fig. 4.7(b). For the case of four transmitters shown in Fig. 4.6(c), channel capacity improvement of about 1.3 bit/s/Hz is obtained in measurement and shown in Fig. 4.7(c). The simulated and measured average channel capacity versus the transmitter power for three different cases is shown in Fig. 4.8. By increasing the transmitter power, the average channel capacity is increased for both BMAA and regular array. For all the cases shown in Fig. 4.8, however, the average channel capacity of the proposed BMAA is more than that of the regular array antenna. Furthermore, the capacity improvement becomes more significant if the number of antennas in the BMAA

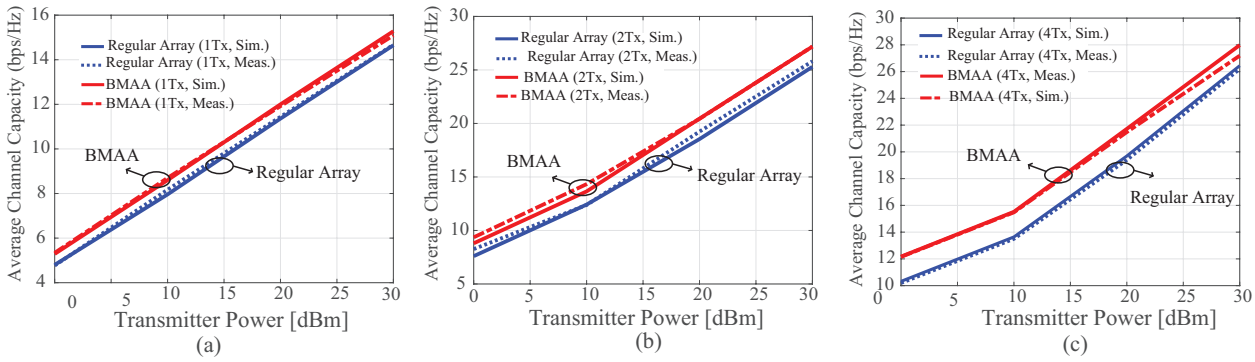

Figure 4.8: Average channel capacity of MIMO systems shown in Fig. 6 that use either the regular antenna array or the BMAA as the receiver. The results are shown as a function of the transmit power. (a) One transmitter. (b) Two transmitters (c) Four transmitters.

or if the number of antennas used in the transmit side are increased. An example of a BMAA that has more than 2 elements have been reported recently [53].

4.5 Conclusions

A two-element BMAA is designed to extract the maximum available power from all linearly-independent modes of excitation of the array. Therefore, this allows for small-aperture BMAAs to achieve significantly larger directivity and gain values compared to those of a traditional array with the same physical aperture size. We examined the use of a two-element BMAA consisting of two $\lambda/4$ monopole antennas as part of a MIMO communication system. The capacity that can be achieved from a MIMO system using the BMAA was compared with that which can be achieved from the same system using a conventional array with the same aperture dimensions. Our results demonstrate that using a two-element BMAA in a MIMO system enhances the capacity of the system compared to the capacity that can be achieved from conventional antenna arrays. To experimentally verify these results, a prototype of a two-element BMAA operating at 615 MHz with element spacing of $\lambda/10$ and a regular array prototype with similar antenna elements and dimensions were fabricated and characterized. The performances of MIMO systems using these two antennas were modeled using numerical

channel modeling using the measured antenna responses. These results are found to be in good agreement with theoretical predictions and quantify the capacity enhancements that two-element BMAAs can provide in a MIMO communication system.

Chapter 5

Electrically-Small Platform-Based Antennas for an Unmanned Ground Vehicle

The full manuscript will be published as:

M. Ranjbar Nikkhah, F. Dagefu, and N. Behdad, "Electrically-Small Platform-Based Antennas for an Unmanned Ground Vehicle," under review in *IEEE Transactions on Antennas and Propagation*.

5.1 Introduction

The very high frequency band (VHF, 30-300 MHz) is used for a wide range of applications including land mobile systems, radio broadcasting, radio navigation, and military and law-enforcement communication systems [59]- [60]. Some recent studies have also shown favorable near-ground channel characteristics of the lower VHF bands, which can be exploited for more persistent communications and geolocation applications [61]- [62]. Conventional antennas at these frequencies are often large due to the relatively long wavelength of electromagnetic waves at this band. To enable the integration of compact, low-power, and low-frequency communications systems on electrically-small platforms, it is desirable to reduce the size of the antennas mounted on such platforms while maintaining good performance in terms of the desired radiation characteristics. Due to the large wavelength of the electromagnetic waves at this band, the need for reduction of the antenna size often results in the use of electrically-small antennas. A common characteristic of an electrically-small antenna is its small radiation resistance and large reactance. These result in drastic reduction of the antenna efficiency and its bandwidth [63]- [64].

In many VHF communication systems, antennas are mounted on vehicular platforms and the platform is inevitably a part of the antenna [65]- [68]. In [69], a design approach was presented in which part of the vehicle was used as the radiating structure to realize an antenna at the high-frequency (HF) band. More recently, different research groups have investigated platform-mounted antennas and pursued a variety of techniques that exploit the presence of the large metallic platform to enhance the performances of such antennas [70]- [77]. In [70], a technique based on the characteristic-mode theory (CMT) was used to excite the desired radiating currents of the platform. In [71], electrically-small antennas were used to excite the dominant mode of a platform and achieve bandwidth enhancement at the HF band. In [72], a single electrically-small antenna was used to excite multiple significant characteristic modes of a military vehicle at VHF frequencies to obtain significant bandwidth enhancement. In

[73], by controlling the variations of the excitation coefficients of the characteristic currents, a 3-D null-scanning antenna was developed. Dual-band HF/VHF, platform-based antennas with enhanced bandwidths in each band were reported in [74]. In [75], CMT was employed to determine optimal position of the coupling elements and efficiently excite the characteristic currents, which improved the radiation efficiency of a platform-mounted radiator. In [76]- [77] the design of platform-based airborne HF antennas using CMT were reported. Furthermore, such CMT-based design techniques have also been applied to design mobile handset antennas by exciting radiating currents on mobile terminal chassis [78]- [79]. While a significant amount of work has been performed on designing platform-based antennas, virtually all of these prior works focus on platforms that are electrically large at the operating frequency (i.e., have electrical dimensions comparable to or larger than a wavelength). Little attention has been paid to designing platform-based antennas for electrically-small platforms. This, however, is an important problem as the use of small unmanned ground-based or airborne platforms that need to use HF, VHF, and UHF frequencies is on the rise.

In this paper, we investigate the design of platform-based antennas that operate on an electrically-small platform. Specifically, the platform under consideration is the Husky unmanned ground vehicle (UGV) having dimensions of 99 cm $\times$ 67 cm $\times$ 39 cm. We have chosen this UGV for this study as it has been previously utilized for various experimental research in the area of ad hoc communications and networking in the VHF range [80]- [81] by the U.S. Army Research Laboratory. However, the design concepts presented in this paper are easily adaptable to other similar sized platforms. We report on the design of platform-based antennas that operate in the lower end of the VHF band at around 40 MHz. This frequency range is chosen as it has been shown to have improved penetration and channel coherence, especially for near-ground nodes [61]- [62]. As a result, low VHF frequencies can potentially be exploited for more robust moderate rate communications and geolocation applications in physically complex environments [61]- [62]. At this frequency, the platform has electrical dimensions of $0.13\lambda_0 \times 0.09\lambda_0 \times 0.05\lambda_0$, where λ_0 is the wavelength in free space.

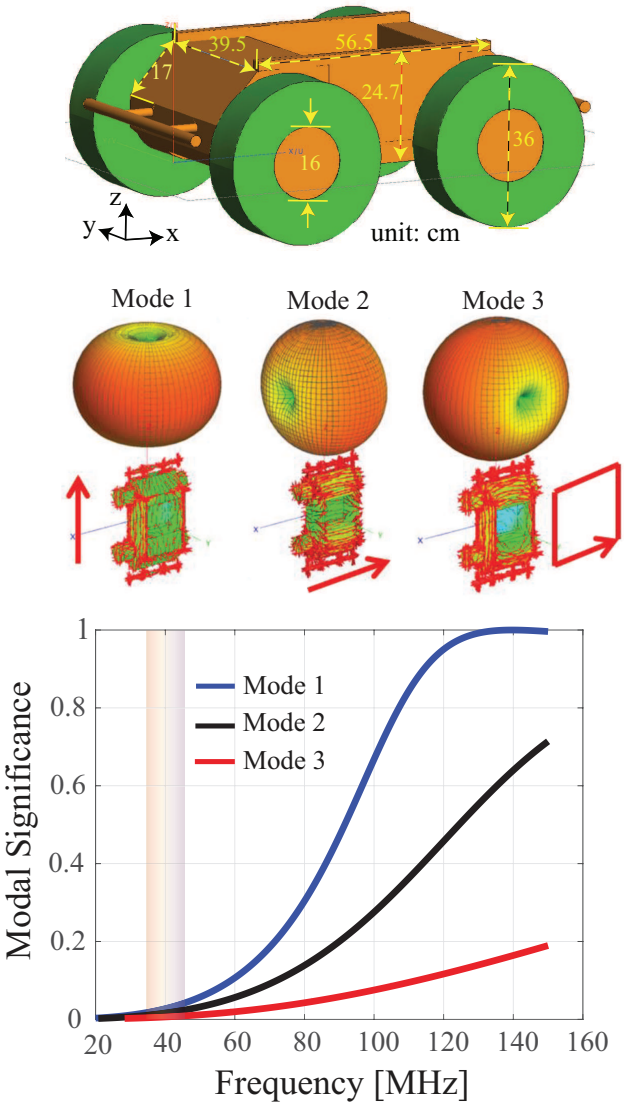

Figure 5.1: (Top) Topology of the platform considered in this work. (Middle) Radiation patterns and electric current distributions of its first three characteristic modes at 40 MHz. (Bottom) Modal significance values of the first three modes as a function of frequency.

Characteristic mode theory is used to evaluate the performance of the proposed antenna and evaluate its bandwidth potential and radiation patterns. The antenna was designed to provide vertically-polarized, monopole-like radiation characteristics. The antenna is mounted underneath the vehicle and has an extremely low profile and virtually zero visual signature. We also investigate the use of the proposed radiating element as part of a two-element, small-aperture direction finding system. Since the two antennas are closely spaced, the coupling between them is strong. Therefore, the antennas' outputs are decoupled using an external matching/decoupling network [82]. The direction-finding performance of this small-aperture antenna array was evaluated by examining its Cramer-Rao lower bound (CRLB). A full-scale prototype of the antenna mounted on the platform was fabricated and experimentally characterized.

5.2 CMT Analysis of The Unmanned Ground Vehicle

We will first investigate the characteristic modes of the platform using full-wave electromagnetic (EM) simulations in FEKO. Fig. 5.1 shows the simplified model of the platform along with the electric current distributions and radiation patterns of the first three characteristic modes of the platform. The modal significance (MS) values of these three modes, as a function of frequency, are also presented in Fig. 5.1. A mode is considered to be significant if its MS value is greater than 0.7 [83]. Since the platform is electrically small, its dominant mode does not have a high modal significance value at 40 MHz. Thus, we consider approaches to enhance the modal significance value of the antenna/platform combination for a more efficient radiation at the desired frequency.

5.2.1 Tailoring the Platform's Characteristic Modes

As seen in Fig. 5.1, the platform does not have any significant characteristic modes at around 40 MHz. Thus, any antenna placed on this platform will change the nature of the platform

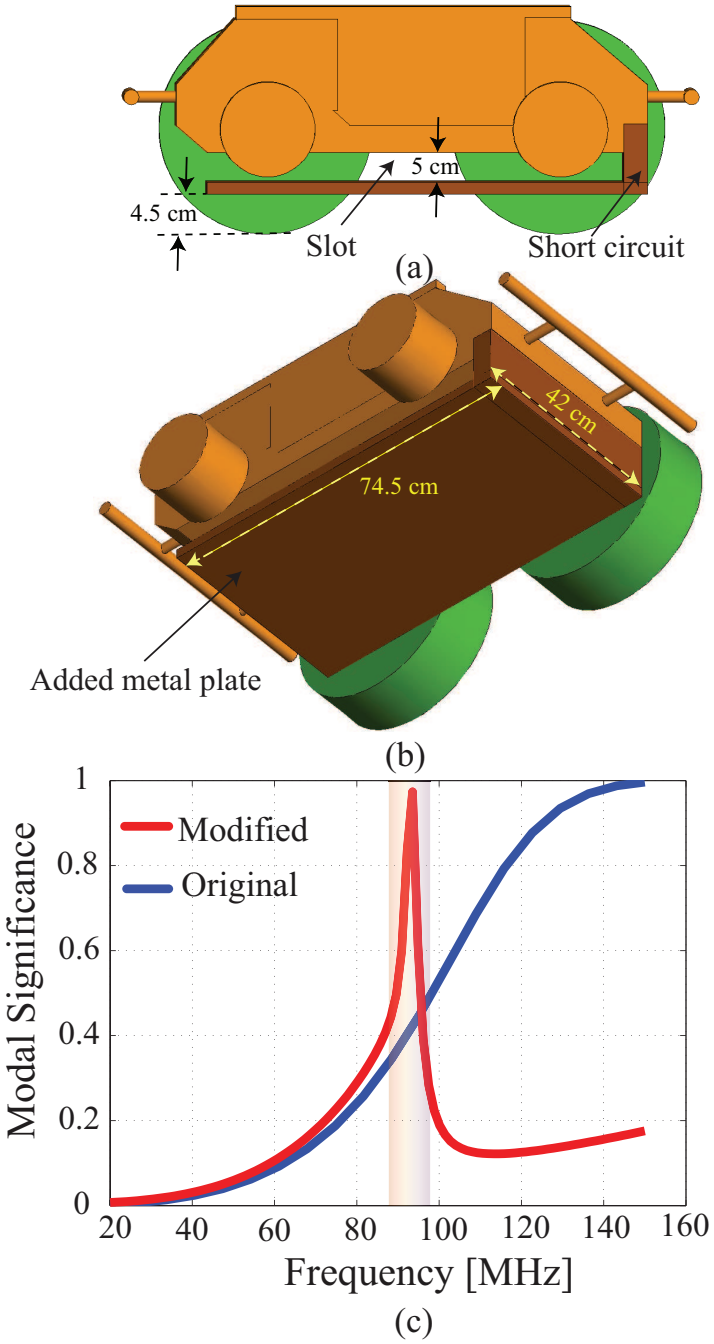

Figure 5.2: (a) Side view and (b) bottom view of the modified platform with a metal plate added underneath it. The metal plate is short circuited to the main body of the vehicle on its side. (c) Modal significance values of the dominant mode of the original and the modified platform versus frequency.

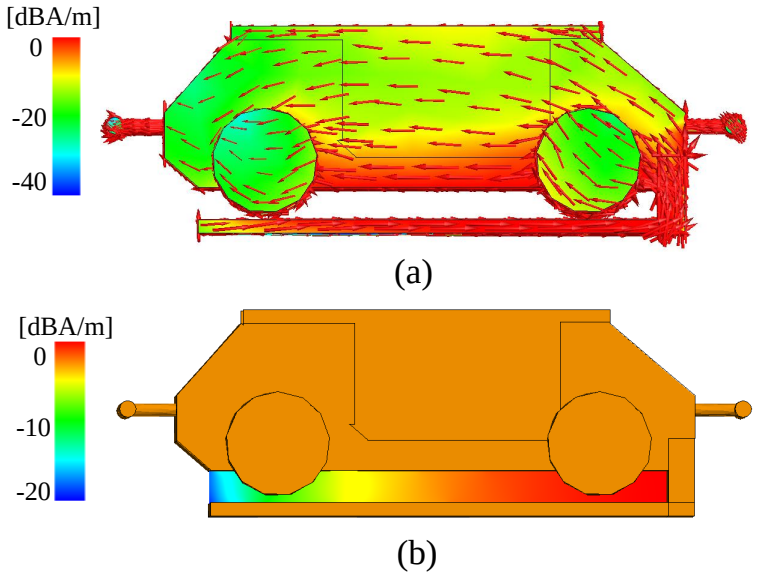

Figure 5.3: (a) Electric current distribution of the dominant characteristic mode of the modified platform shown in Fig. 5.2 at 93 MHz. (b) The magnetic field distribution in the slot area underneath the platform.

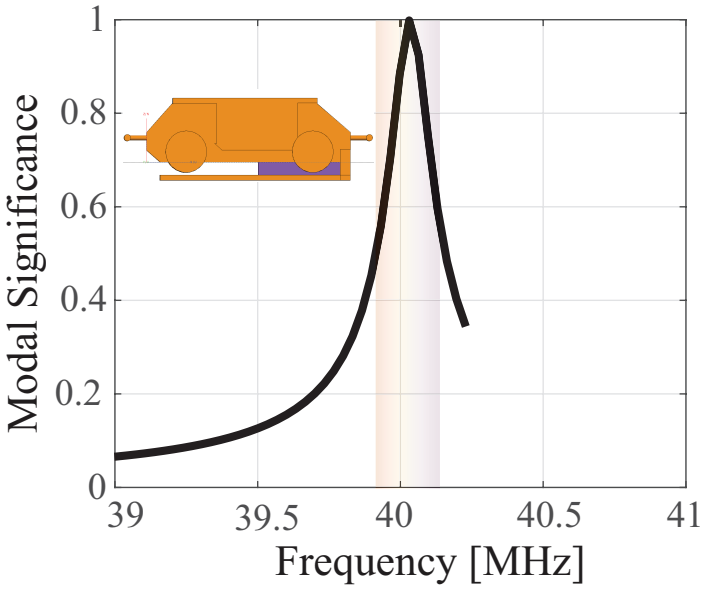

Figure 5.4: The modal significance value of the dominant mode of the modified platform shown in Fig. 5.2 when the slot is loaded with a magnetic material. The topology of the modified structure is shown in the inset of the figure.

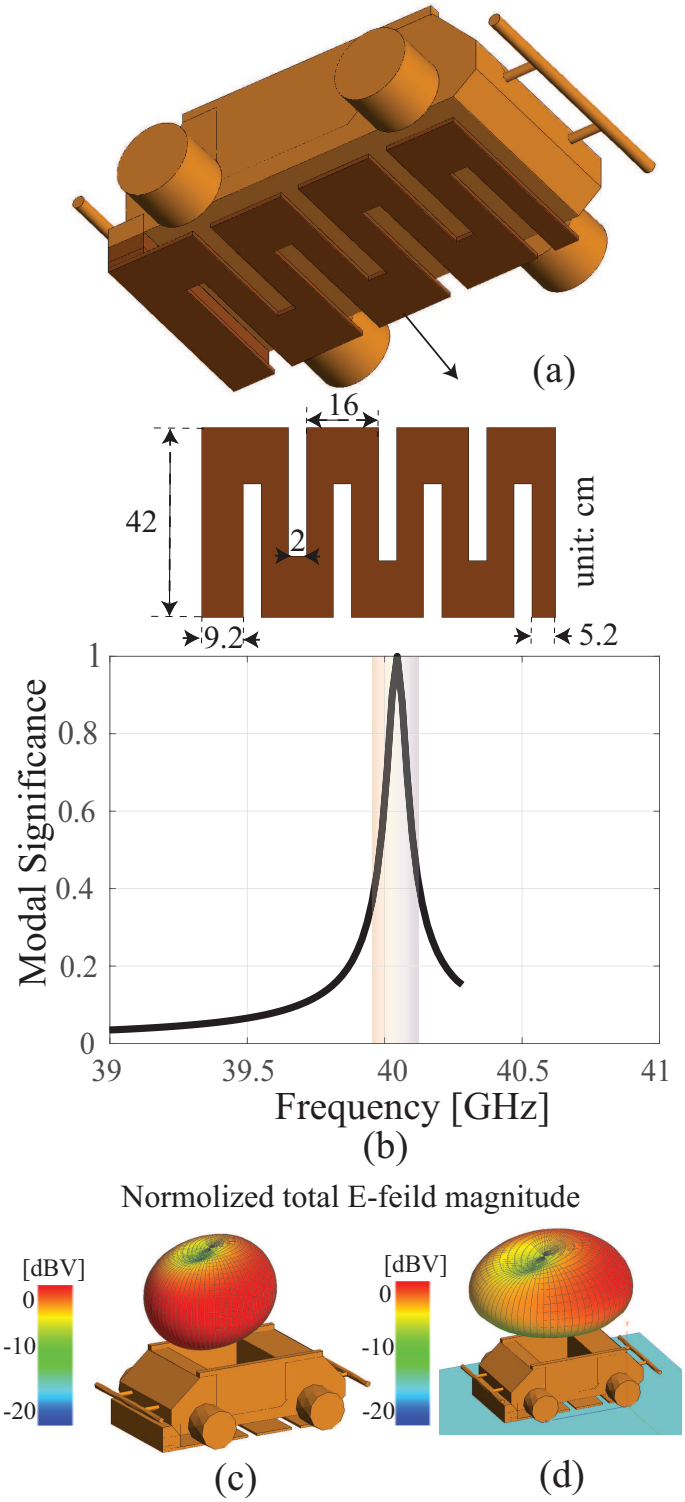

Figure 5.5: (a) Topology of the modified platform with an added metal plate having slits cut within it. The added plate is short-circuited to the platform on its side. (b) Modal significance value vs. frequency for the dominant mode of the platform shown in part (a). (c)-(d) Radiation patterns of the dominant mode when the platform is isolated in free space (c) and when it is mounted on a real ground with dielectric properties of dry earth [86] (d).

and its modes. In this section, we examine the impact of placement of such antennas on the platform using CMT analysis of the antenna/platform combination. For practical reasons, we only consider antenna structures that can be mounted on (or added to) the platform in a non-destructive fashion (i.e., structures that do not require the platform to be cut). Moreover, placing such an antenna on the bottom of the vehicle is of great interest since in practical situations of interest to the Army, the top surface of the vehicle is used to accommodate other sensors or actuators (e.g., cameras, robotic arms, etc.). Towards this aim, we start by adding a plate underneath the vehicle, which is connected to the main body of the vehicle at one end (see Figs. 5.2(a) and 5.2(b)). The volume between the bottom surface of the vehicle and the added metal plate, short circuited to one end of the vehicle, forms a half-slot antenna (i.e., a slot antenna open circuited in the middle). Subsequently, the commercial software FEKO was used to perform the characteristic mode analysis of the modified platform. The modal significance values of the first mode of the original platform and that of the modified platform are compared in Fig. 5.2(c). As seen, the frequency range where the mode is significant (i.e., $MS > 0.7$) is shifted from 150 MHz to 93 MHz. The surface current distribution and magnetic field intensity in the slot region (at 93 MHz) are respectively shown in Figs. 5.3(a) and 5.3(b). As seen, both results confirm the presence of a half-slot mode in the region between the bottom of the vehicle and the added metal plate.

To further reduce the frequency where the modal significance value becomes 1 (i.e., the resonant frequency) down to our target frequency of 40 MHz, two techniques were investigated. The first technique is to load the slot antenna with a magnetic material at a location where the intensity of the magnetic field is strong. In doing this, the realistic model of a commercially-available magnetic material was used (Soft Ferrite Component 67 Material Grade from Fair-Rite Products Corp. [84]). The constitutive parameters of this magnetic material at 40 MHz are $\mu_r = 40$, $\epsilon_r = 6.9$, $\tan \delta_m = 6.2 \times 10^{-3}$, $\tan \delta_d = 2.9 \times 10^{-3}$. Fig. 5.4 shows the topology of the magnetically-loaded slot antenna and its modal significance factor as a function of frequency. In this case, only a portion of the slot in the region where the

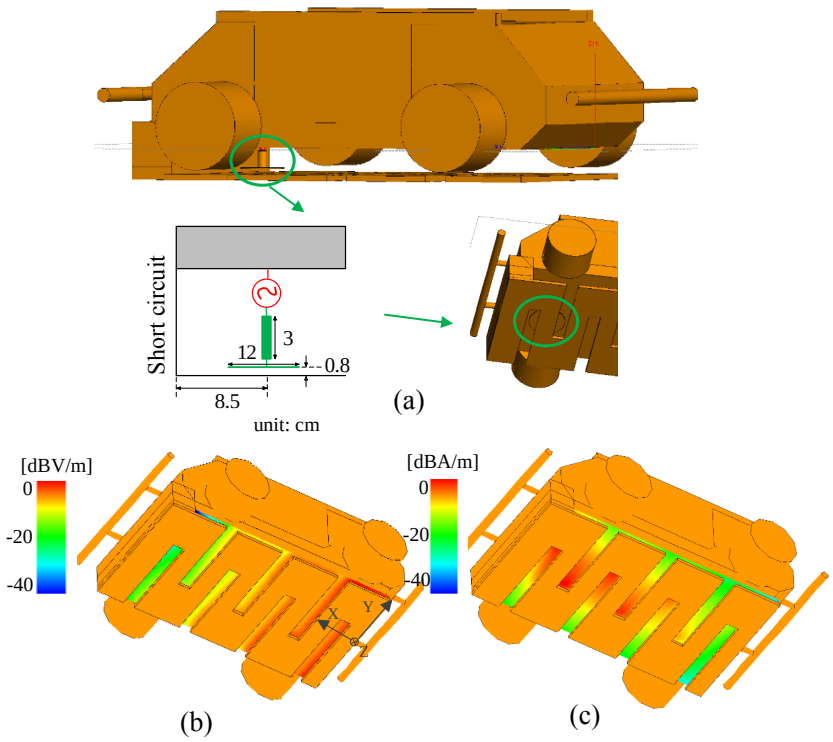

Figure 5.6: (a) Topology of the modified platform and the feed network used to excite the dominant mode of the platform. (b) Electric and (c) magnetic field distribution in the slot region formed between the bottom of the vehicle and the added meandered metal plate. The results are shown at 40 MHz.

intensity of the magnetic field is strong (the edges close to the short-circuit location as seen in Fig. 5.3(b)) is loaded with the magnetic material. The material has physical dimensions of 5 cm $\times$ 29 cm $\times$ 42 cm. Observe that the modal significance value is shifted down to 40 MHz as expected. While loading the slot with a magnetic material does reduce the frequency of operation down to 40 MHz, it comes at the expense of adding significant weight to the platform. Specifically, for the structure shown in Fig. 5.4, the added weight of the magnetic material is 55 lbs (25 kg), which is significant for this UGV.

The second technique we examined for reduction of the resonant frequency of the slot antenna shown in Fig. 5.2 was to inductively load the ground plane of the slot antenna with a series of slits following the approach discussed in [85]. Placing the slits in the added plate, which forms part of the ground plane of the slot antenna, forces the electric current flowing

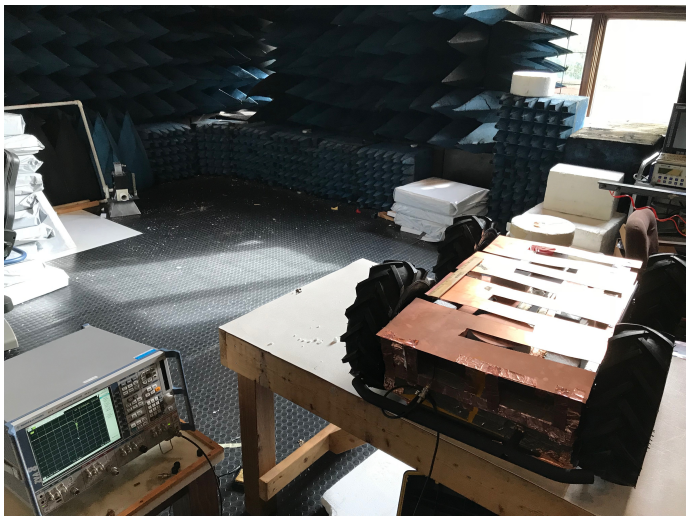

Figure 5.7: Photograph of the fabricated platform-based antenna prototype shown in Fig. 5.6.

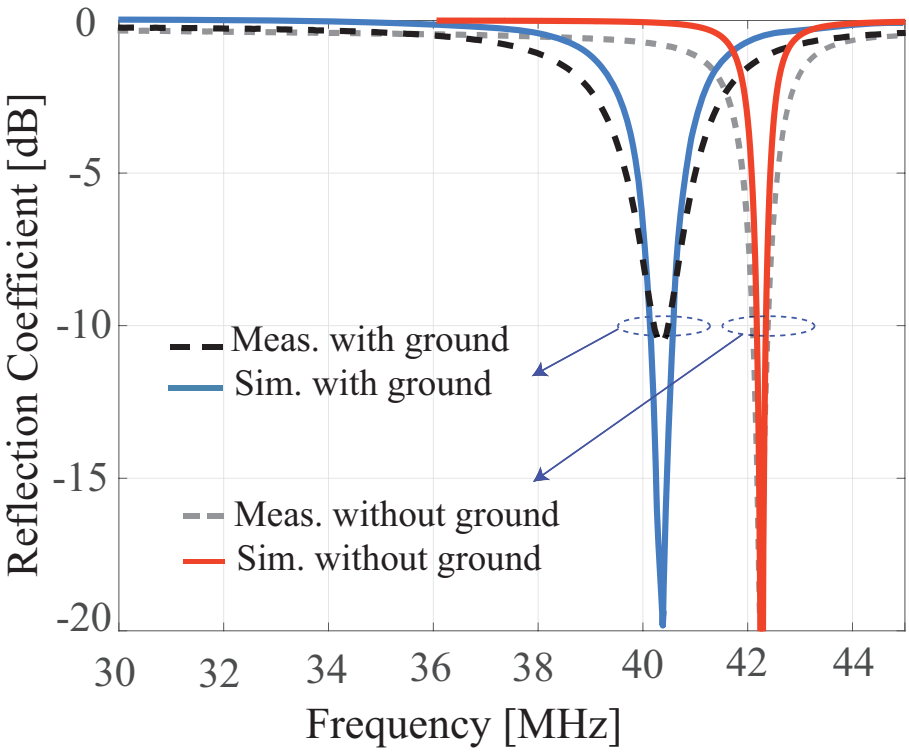

Figure 5.8: The measured and simulated input reflection coefficients of the proposed platform-based antenna shown in Figs. 5.6 and 5.7. When the UGV is placed on ground, a slight shift in resonant frequency is observed.

Figure 5.9: Photograph of the outdoor test setup used to characterize the performance of the platform-based antennas reported in this work.

in the ground plane to travel a longer path effectively increasing the electrical length of the slot. Doing this converts the ground plane to a meandered-shaped wide metallic structure as seen in Fig. 5.5(a). The length of the slits and their numbers can be controlled to reduce the resonant frequency of the antenna down to the desired frequency of 40 MHz. Fig. 5.5(b) shows the modal significance value of the platform with slit-loaded plate on the bottom. As can be observed, the resonant frequency (identified as the frequency with $MS = 1$) is reduced to around 40 MHz. Comparison of the MS curves shown in Fig. 5.5(b) and Fig. 5.4(b) reveals that the antenna exploiting magnetic materials has a wider bandwidth potential (defined as the frequency range with a $MS > 0.7$) compared to that using the meandered ground plane. This, however, comes at the expense of the added weight of the magnetic material, which is a significant drawback for many potential applications. Consequently, in the present work, we proceeded with the second design approach. Fig. 5.5(c) and Fig. 5.5(d) show the radiation patterns of the modified platform from the CM analysis for the two different cases. In the first case, the platform is placed in the free space and in the second case, the platform is placed on a realistic concrete earth plane with $\epsilon_r = 4.5$ and $\sigma = 10^{-3}$ s/m at 40 MHz [86], [87]. The realistic dry earth is modeled by Sommerfeld integrals in FEKO software.

5.2.2 Excitation Method of the Modified Platform/Antenna Configuration

The results shown in Fig. 5.5 demonstrate that the modified platform can act as an efficient antenna at around 40 MHz. To do this, however, a suitable feed mechanism must first be developed. Since the region underneath the platform acts as a half-slot antenna, one can feed it with a simple probe as shown in Fig. 5.6(a). In this case, the probe is in the form of a vertical wire capacitively loaded at its end with a circular-shaped conductor. The size of this conductor and the gap between that and the added bottom plate can be controlled to change the capacitive reactance with which the feed is terminated. Impedance matching in this antenna is performed by choosing the location of the feed probe and the value of the terminating capacitance. Figs. 5.6(b) and 5.6(c) show the electric and magnetic field distributions in the slot region. Since a standing wave pattern exist in this region, the location of the peak of the magnetic field approximately coincides with that of the null of the electric field and vice versa. Consequently, placing the probe at a location between the peak values of the magnetic and electric field results in an input impedance close to 50 Ω. The value of the capacitive patch at the end of the probe can be tuned to compensate for the inductive input impedance of the antenna and achieve a good match to 50 Ω. Using this feeding and matching technique, no additional external matching network is required.

5.2.3 Fabrication and Experimental Characterization

The proposed antenna was fabricated using a full-scale platform and a photograph of the fabricated antenna and the platform (with a view from the bottom of the platform) is shown in Fig. 5.7. The meander-line section and the feed parts were fabricated separately and assembled to the bottom of the platform. A copper sheet with thickness of 0.7 cm was used for the fabrication of the meander-line. To have a consistent alignment for the spacing between meander-line part and the back of the platform, five dielectric spacers made out of

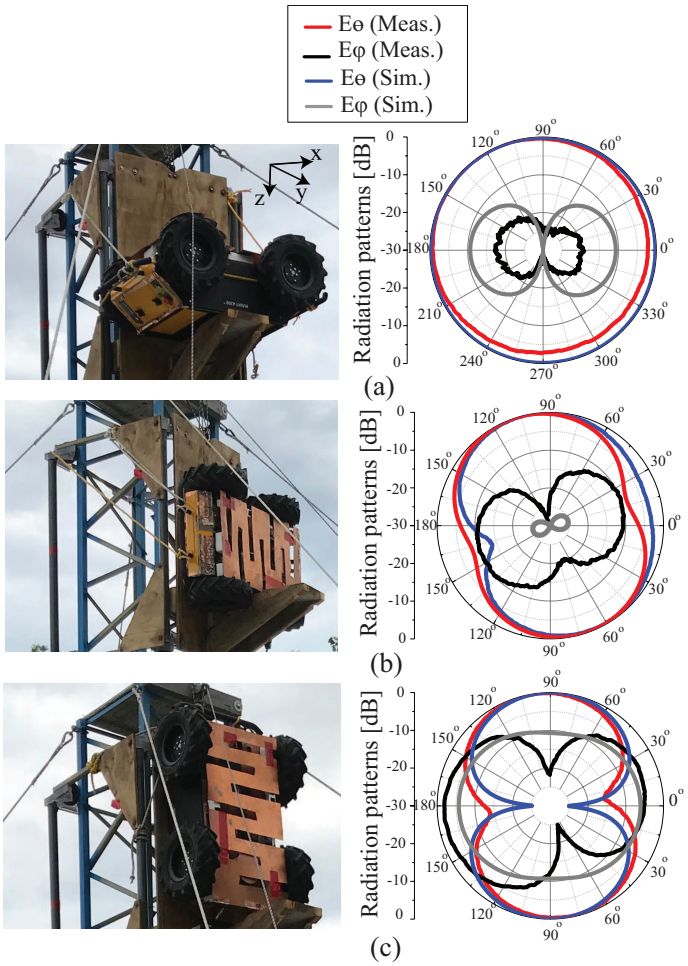

Figure 5.10: The measured and simulated radiation patterns of the platform-based antenna shown in Fig. 5.6 and Fig. 5.7 in three different cuts. (a) $x-y$ plane, (b) $x-z$ plane, and (c) $y-z$ plane. The coordinate system is shown in Fig. 5.1 and Fig. 5.6(b).

foam were placed between them. The measured and simulated reflection coefficients for the proposed platform-based antenna are shown in Fig. 5.8. The performance of the antenna when the platform is placed over a realistic ground was measured and it can be seen that the resonant frequency is slightly shifted in the presence of the ground (Fig. 5.8). We observed that this frequency shift is increased when the vehicle is driven close to a wall. Fig. 5.8 shows a difference between the measured and simulated impedance bandwidths of the antenna. This is attributed to the uncertainty in the precise values of the dielectric constant and conductivity of the ground over which the experiments were performed. In the simulations, these values were assumed to be $\epsilon_r = 3$ and $\sigma = 10^{-4}$ S/m at 40 MHz [86]. However, we

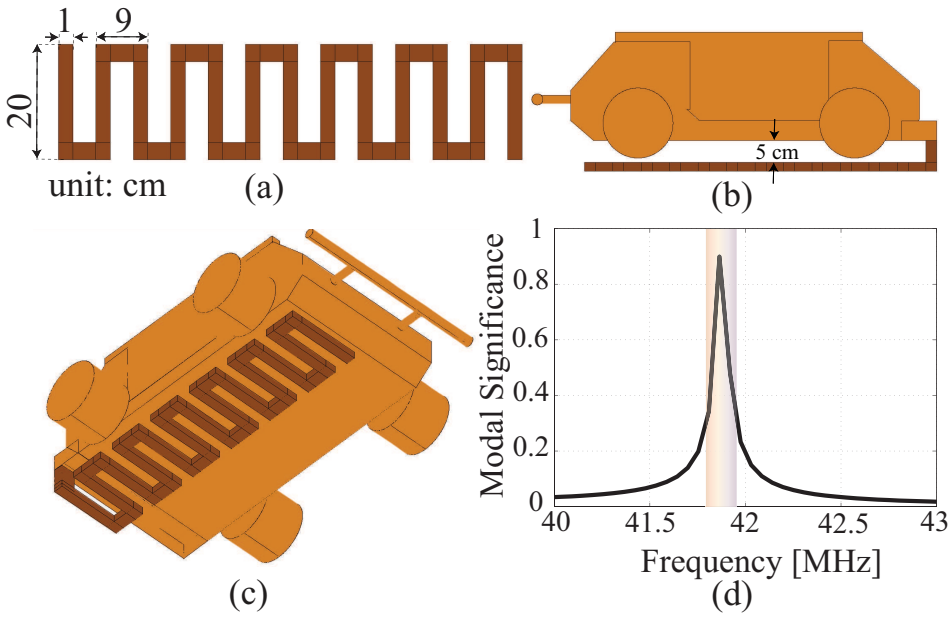

Figure 5.11: Modal significance value vs. frequency for the platform when the added, meandered metal plate only occupies half of the available area underneath the vehicle. The topology of the modified structure is shown in the inset of the figure.

were unable to measure these parameters for the surface over which the experiments were performed[1]. All other parameters, including the conductivity of all the materials used to construct the antennas, were taken into account in the simulations. In practice, because the operational environment does impact the performance of such an antenna, using a tunable impedance matching network in conjunction with this antenna is recommended.

The far-field radiation patterns of the antenna were measured in an open test range at the Willow Run Test Labs, Inc. in Brighton, MI [88]. The outdoor experimental setup for the radiation pattern measurement is shown in Fig. 5.9. The antenna under test was used as the receiver antenna and a standard dual-polarized biconical antenna was used as the transmitter antenna. The measured maximum realized gain was -10.5 dBi and during the radiation pattern measurements, ferrite beads were used to prevent sheath currents on the cable shields. The simulated and measured radiation patterns of the antenna in three different cuts of $x-y$, $x-z$, and $y-z$ planes are shown in Fig. 5.10.

[1]The measurements were tested in outdoor for several times to make sure if the results are consistent.

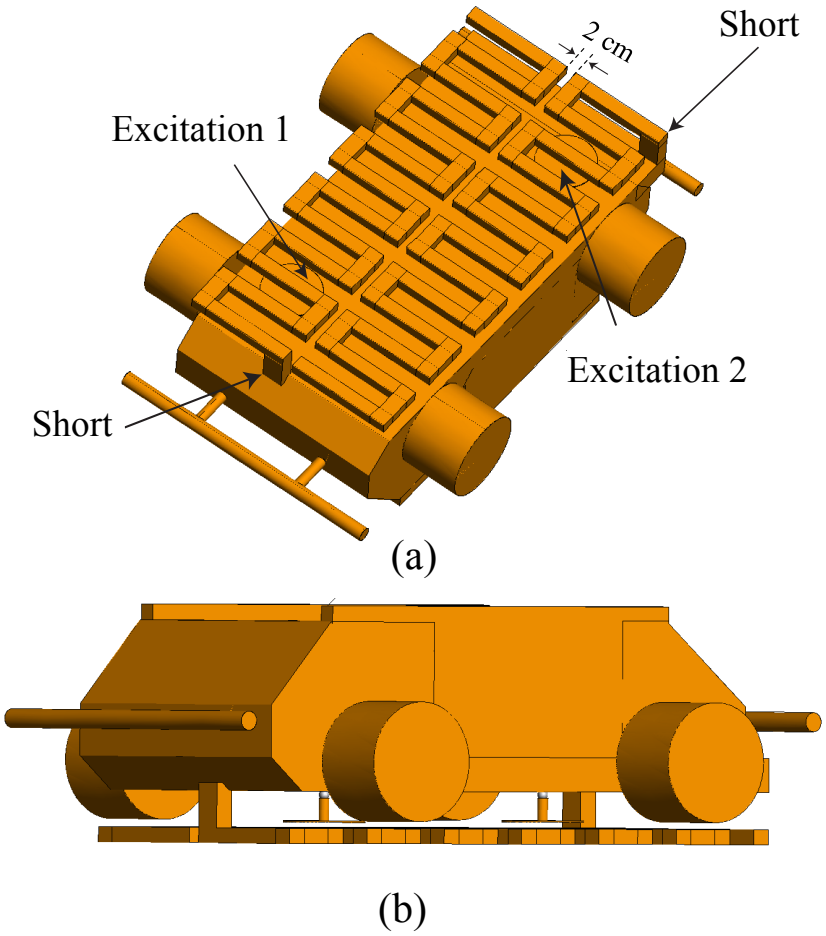

Figure 5.12: (a) Perspective view and (b) side view of the topology of the modified platform with two antennas mounted underneath the vehicle. The two antennas are excited with capacitive probes. To decrease the mutual coupling between the two antennas, they are fed from two opposite directions as shown in the figure.

5.3 Concept Expansion To A Two-Element Array

5.3.1 Design of the Two-Element Platform-Based Array

Here we describe the design of a two-element antenna array for the same UGV platform whose elements are of the type discussed in Section II. Following the same practical considerations, the two antennas were designed to be placed underneath the platform as was the case for the single-element antenna discussed in Section II. Consequently, to design a two-element antenna array, each antenna can at most use half of the available space. To do this while

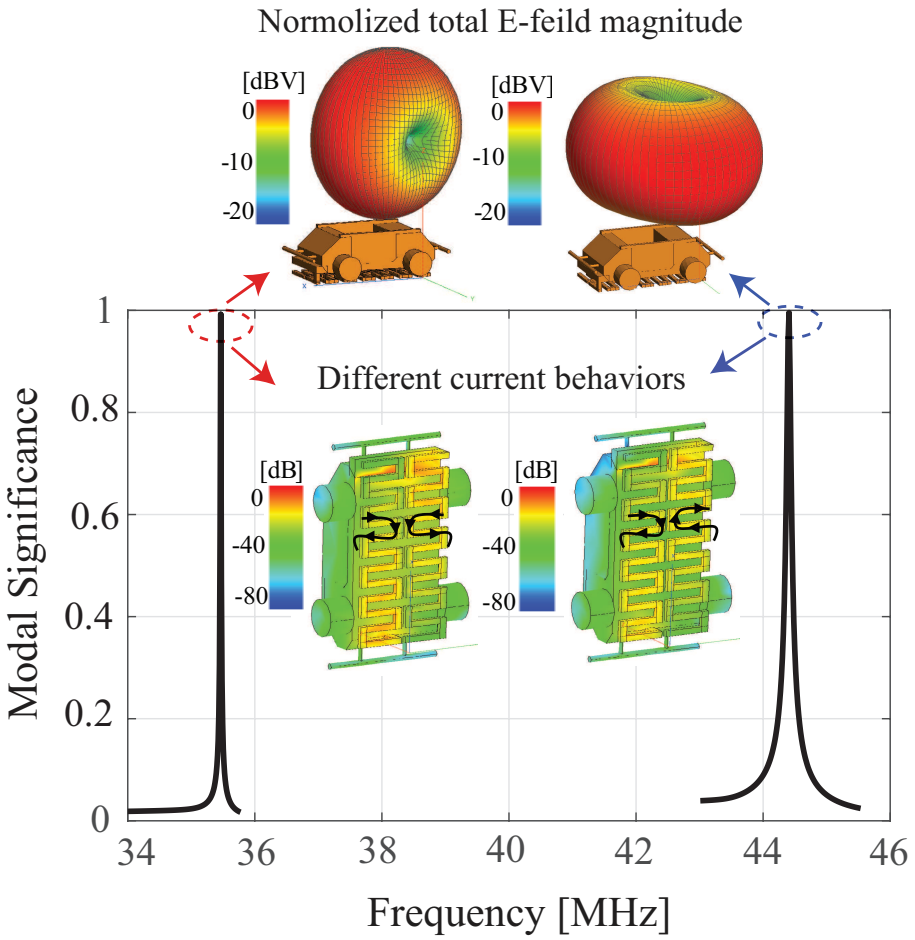

Figure 5.13: Modal significance value of the two-element array without feed probes. Observe that the structure has two significant modes with two different radiation characteristics. The current distributions and radiation patterns of the two modes, obtained from CMT analysis in FEKO, are shown in the figure.

Figure 5.14: Photograph of the fabricated two-element platform-based array.

maintaining the frequency of operation in the 40 MHz range, the number of slits used in each slot antenna was increased. Fig. 5.11 shows the topology of this modified platform and its modal significance value as a function of frequency. Observe that the structure can provide a significant mode in the desired frequency range. To feed the antenna we followed the method presented in Section II-B. The excitation probe consists of a vertical wire capacitively loaded at its end with a circular-shaped conductor. By choosing suitable dimensions for the probe's capacitive plate and the gap between the tip of the probe added the bottom plate and also the location of the feed probe, the impedance matching is realized without using any external matching network. Then, to design a two-element array, two half slot antennas are placed on the bottom of the UGV as shown in Fig. 5.12. To reduce the mutual coupling between the two antennas, the half slot antennas are placed in an asymmetric configuration on the bottom of the platform (see the excitation ports and short-circuit locations in Fig. 5.12(b)). Fig. 5.13 shows the modal significance value for the structure shown in Fig. 5.12 without the feed probes. Observe that the structure has two significant modes with different polarizations and radiation patterns. The lower band has a horizonal polarization and the upper band has a vertical polarization. For the current applications, the radiation characteristics of the higher band are of interest. Frequency splitting, which is common for coupled resonant systems, is observed in Fig. 5.13. This phenomenon is discussed through the coupled mode theory [89] in equation 1 given in [90] and also recently is explained using common and differential modes (see Fig. 8 in [91]).

5.3.2 Fabrication and Experimental Characterization

Following the same practical considerations discussed in Section II-C, the two-element array was fabricated and assembled as shown in Fig. 5.14. The antenna is excited capacitively in a similar fashion as that shown in Fig. 5.6 and discussed in Section II-B. The simulated and measured scattering parameters of this antenna are shown in Fig. 5.15. As seen, two resonances are observed from the coupled antennas shown in Fig. 5.12. The dual-mode be-

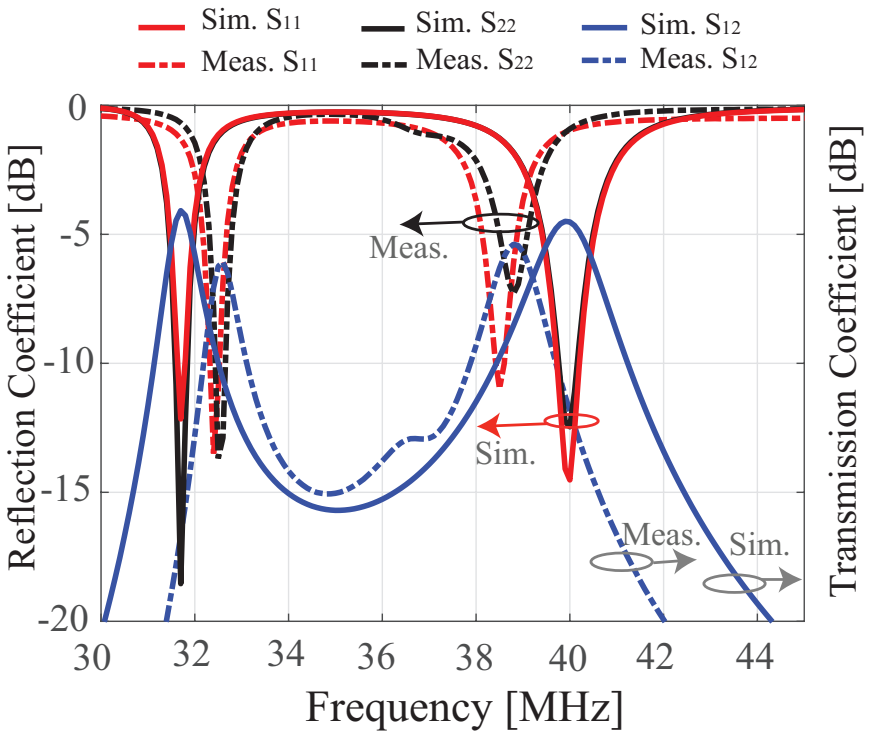

Figure 5.15: Measured and simulated reflection and transmission coefficients of the two-element, platform-based antenna array shown in Fig. 5.12.

havior of this structure was also observed through CMT analysis in Fig. 5.13. The radiation patterns of the antennas were measured in three different cuts of $x-y$, $x-z$, and $y-z$. The measurements were performed for both antennas at both resonant frequencies, corresponding to the lower (undesired) band and the higher (desired) band. For each measurement one port is excited and the other port is connected to 50 Ω load. When the radiation pattern measurements were performed, ferrite beads were used to prevent sheath currents on the cable shields. The radiation pattern results are shown in Fig. 5.16. The measured maximum realized gain for the port one and port two for the lower band were -23.5 dBi and -23 dBi, respectively. The measured gains for the two antenna at the upper frequency band for ports one and two were -14.5 dBi and -15 dBi, respectively. The reduction of the antenna gain (for the higher band) compared to the previous case is attributed to the smaller electrical dimensions of each individual antenna as well as the strong mutual coupling between them. As can be observed in Fig. 15, the transmission coefficient between the two antennas is

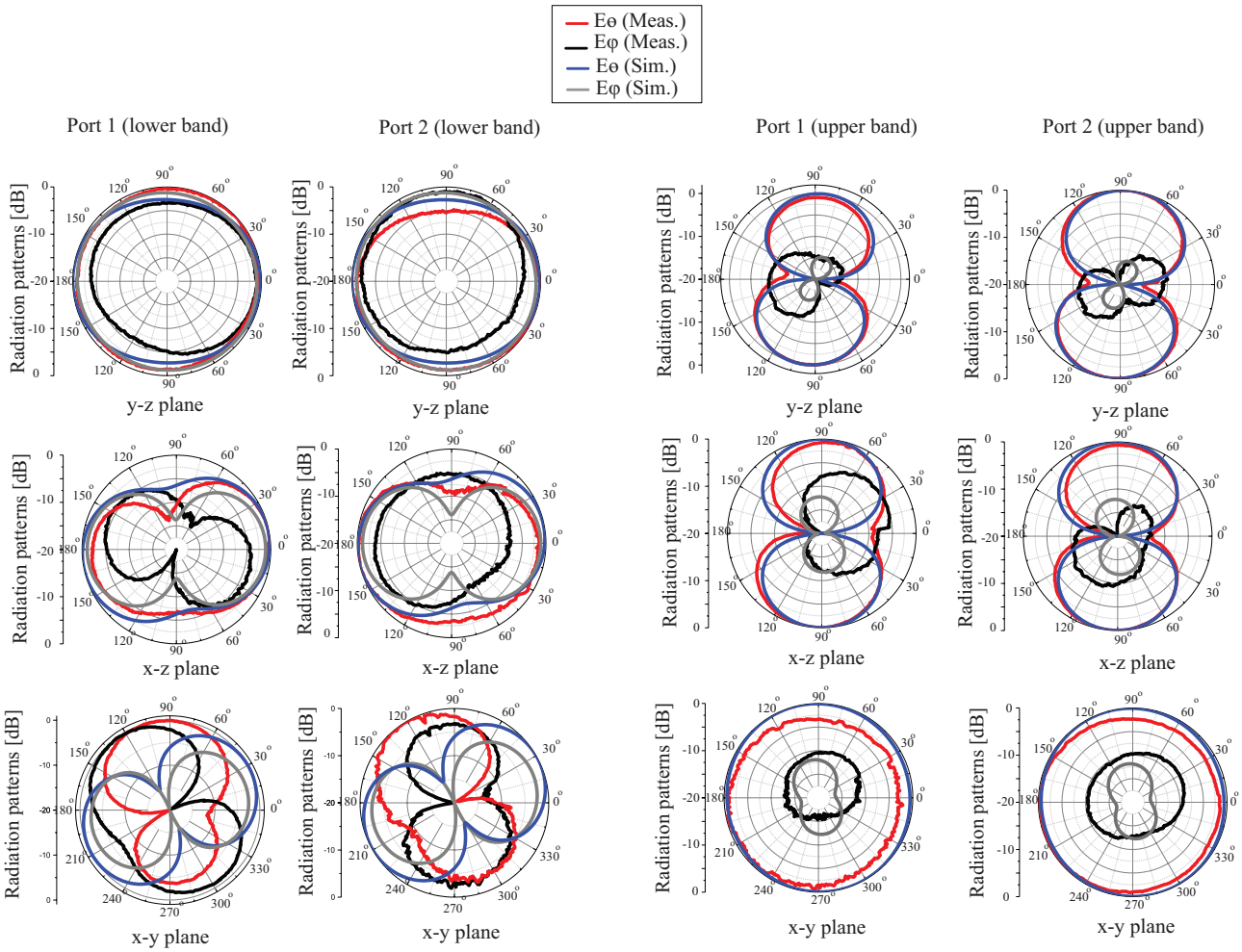

Figure 5.16: Measured and simulated radiation patterns of the two-element antenna array shown in Fig. 5.12. The results are shown for three different cut planes of $x-y$, $x-z$, and $y-z$ planes and for both antennas at the two bands. For each measurement one port is excited and the other port is terminated with 50 Ω. When the radiation pattern measurements were performed, ferrite beads were used to prevent sheath currents on the cable shields.

approximately -5 dB at 40 MHz. This reduces the efficiency of the antennas since approximately 30% of the power fed into each antenna is absorbed by the matched load connected to the other antenna as opposed to getting radiated.

5.3.3 System Behavior with a Decoupling Network

The simulation and measurement results presented in the previous section show a significant level of mutual coupling between the two closely-spaced antenna elements. This is expected

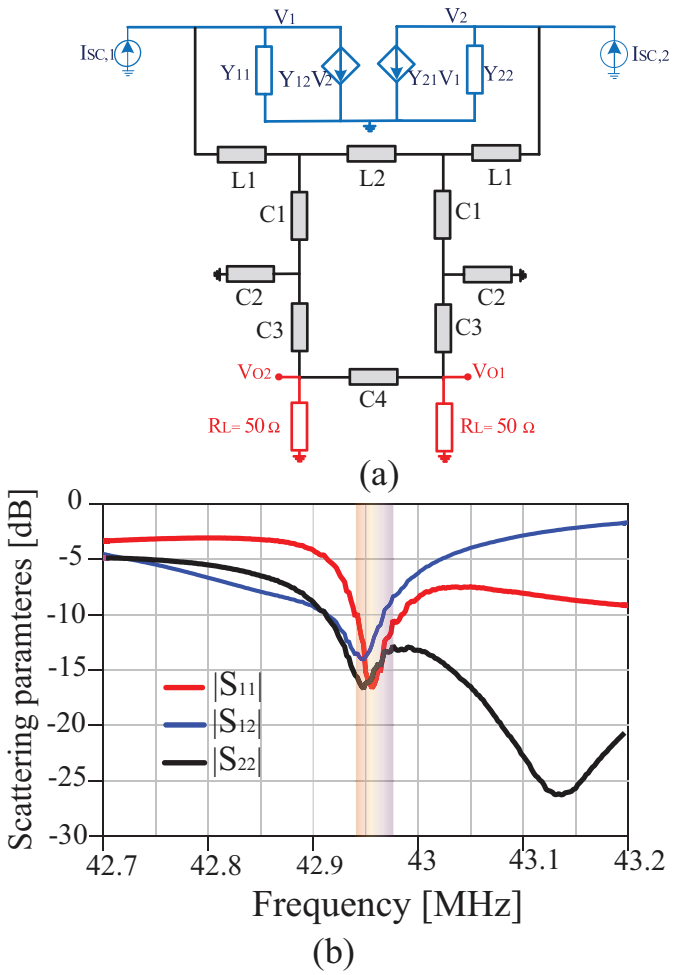

Figure 5.17: (a) Topology of the decoupling network used to obtain the results shown in part (a). Element values of the decoupling network are as follows: L_1 =21.4 nH, L_2 = 124 nH, C_1 = 0.31 nF, C_2 = 0.2 nF, C_3 = 0.41 nF, C_4 = 0.68 nF. (b) Simulated S-parameters of the two-element, platform-based array of Fig. 12 when used in conjunction with an external decoupling network.

because the two electrically-small antennas are extremely close to each other and share the same platform. However, this strong mutual coupling is undesired when this array is used as part of a direction-finding system. To circumvent this problem, the antennas can be decoupled from each other using an external matching and decoupling network [82], [92]. In this work, we use a decoupling network topology of the type reported in [92]. The symmetric decoupling network has six independent reactive elements placed between the two antennas and connected to two load impedances of 50 Ω. To extract the maximum power

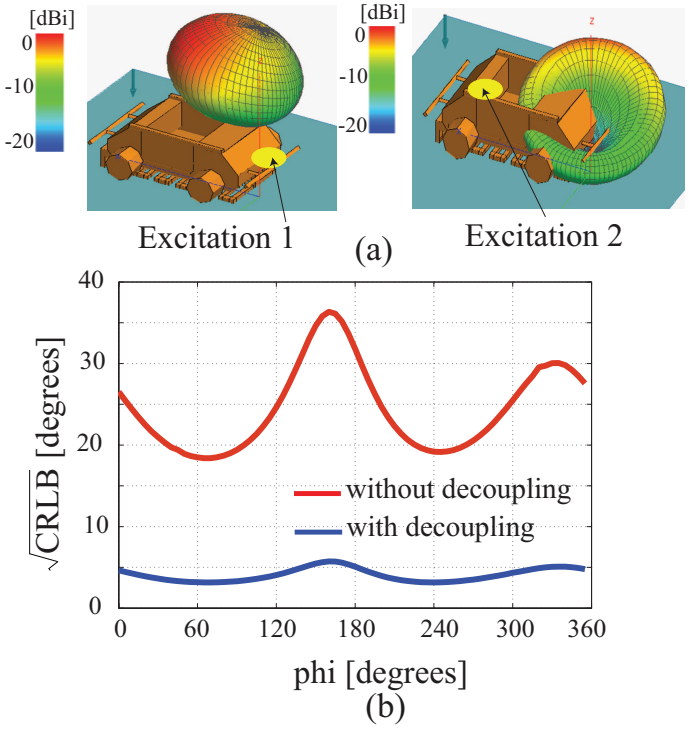

Figure 5.18: (a) Radiation patterns of the decoupled, two-element antenna array when the platform is placed on dry earth with properties of $\epsilon_r = 3$ and $\sigma = 10^{-4}$ S/m. The results are shown at 42.95 MHz. (b) Comparison of the CRLB of the two-element antenna array with operated with and without the external decoupling network. The CRLB values were computed under the assumption of having an available SNR of 25 dB and the number of snapshots of $K = 1$. Observe that the use of the decoupling network will significantly enhance the direction-finding accuracy of the system.

from an incoming wave incident from an arbitrary direction, the array must be impedance matched in the common and the differential modes. These conditions are defined as goals of an optimization procedure used to determine the element values of the external coupling network. This optimization procedure was carried out using the built-in optimization engine of the circuit simulation software Keysight Advance Design System (ADS). The platform was placed on the realistic dry ground plane [86], which was modeled by Sommerfeld integrals in FEKO. The mutual coupling between the two antennas is reduced significantly as shown in Fig. 17. The radiation patterns of the antenna, when using the external decoupling network, are shown in Fig. 18. As seen, two diverse radiation patterns with vertical polarization are achieved. Next, we calculated the Cramer-Rao lower bound values for the direction finding

accuracy of a direction-finding system that uses this antenna array as its receiving elements. To accomplish this, the procedure described in equations (3)-(7) given in [93] was used. We computed the CRLB with the simulated 3-D radiation patterns (including the magnitude and phase) of the antenna shown in Fig. 5.12. The CRLB values were computed under the assumption of having an available SNR of 25 dB[2] and the number of snapshots of $K = 1$. The direction of arrival estimation RMSE for two cases of with/without external decoupling network are shown in Fig. 5.17(b). As seen, the use of this decoupling network can improve the RMSE for the direction finding by more than 15° for all azimuth incidence angles.

5.4 Conclusions

In this paper, the design of platform-based antennas for electrically-small platforms such as small unmanned ground vehicles were reported. Specifically, we examined the design of platform-based antennas operating at the lower end of the VHF band for a small UGV with electrical dimensions of $0.13\,\lambda_0 \times 0.09\,\lambda_0 \times 0.05\,\lambda_0$. We used the characteristic mode theory to evaluate the performance of designed antennas for operation on this platform. Using CMT, performance metrics of the antennas including resonant frequency, radiation pattern, and polarization were examined. The antennas were designed to generate vertically-polarized, monopole-like radiation patterns. The performances of these antennas when operating on realistic ground models were investigated. Through this design process, a prototype which offered a good compromise between size, mounting location, and weight was chosen for further investigation and fabricated and experimentally characterized. The radiation characteristics of this antenna were examined by using a full-scale platform and performing measurements in an outdoor antenna measurement range. We also investigated the use of this radiating element as part of a two-element, small-aperture direction finding system designed for operation at the VHF frequency band. A prototype of such a two-element array mounted on

[2]The available SNR is defined as the SNR that a receiver has when the realized gain of the receiving antenna is 0 dBi.

the full-scale platform was also fabricated and experimentally characterized. Since the two antennas are closely-spaced and share the same platform, a strong level of mutual coupling between them is present, which deteriorates the direction-finding accuracy of the system. To address this issue, we proposed the use of a decoupling network between the two antennas and investigated the impact of doing so using computer simulations and calculation of the Cramer-Rao lower bound of the system with and without the decoupling network. It is demonstrated that the use of the decoupling network with this two-element platform-based array significantly improves the direction-finding accuracy of this platform-based array.

5.5 Acknowledgement

The authors would like to thank Ruyu Ma from University of Wisconsin-Madison for CRLB calculation in Section III-C.

Chapter 6

Future Work

6.1 Future Work

In this thesis, Biomimetic small aperture antenna arrays and their conjunction with electrically small platform were introduced. First in chapter 2, we presented a two-element tunable biomimetic antenna array (BMAA) that uses a single varactor to achieve tunability over a relatively wide band. In Chapter 3, we presented a three-element biomimetic antenna array (BMAA) with an electrically-small triangular lattice. It will allow for resolving ambiguities problem when such BMAAs are used in small-aperture direction finding systems. Then, in Chapter 4, we present the performance of multi-input-multi-output (MIMO) communications systems that exploit biomimetic antenna arrays (BMAAs) with electrically-small aperture dimensions. Finally in Chapter 5, we presented a design strategy for platform-based antennas operating on electrically-small platforms such as unmanned ground vehicles (UGVs) working in conjunction of biomimetic antenna array. A major areas that the present work can be extended to:

(i) Millimeter wave radar sensor based on BMAA, (ii) A machine learning strategy based method for dynamic real-time adaptive automatic impedance matching. (iii) EM Analysis of a large dynamic system from moving electrically small platforms (like UAV) for real application. (iv) Exploring remotely and real-time techniques for sensing the characteristic of the earth (environment modeling) for the real-time adaptive automatic impedance matching of the HF-VHF platform based antenna.

Bibliography

[1] S. A. Schelkunoff, "Forty years ago: Maxwell's theory invades engineering - and grows with it," *IEEE Trans. Antennas Propag.*, vol. 18, no. 3, pp. 309-322, May 1970.

[2] E. Newman, J. Richmond, and C. Walter, "Superdirective receiving arrays," *IEEE Trans. Antennas Propag.*, vol. 26, no. 5, pp. 629-635, Sep. 1978.

[3] R. C. Hansen, *Electrically Small, Superdirective, and Superconducting Antennas*, Wiley-Interscience, 2006.

[4] E. Newman and M. Schrote, "A wide-band electrically small superdirective array," *IEEE Trans. Antennas Propag.*, vol. 30, no. 6, pp. 1172-1176, Nov 1982.

[5] J. P. Daniel, "Reduction of mutual coupling between active monopoles: Application to superdirective receiving arrays," *IEEE Trans. Antennas Propag.*, vol. 25, no. 6, pp. 737-741, Nov. 1977.

[6] A. D. Yaghjian, T. H. O'Donnell, E. E. Altshuler, and S. R. Best, "Electrically small supergain end-fire arrays," *Radio Sci.*, vol. 43, pp. 1-13, 2008.

[7] O. Malyuskin and V. F. Fusco, "Ultracompact retrodirective antenna arrays with superdirective radiation patterns," *IEEE Trans. Antennas Propag.*, vol. 64, no. 7, pp. 2923-2935, July 2016.

[8] A. Haskou, A. Sharaiha, and S. Collardey, "Design of small parasitic loaded superdirective end-fire antenna arrays," *IEEE Trans. Antennas Propag.*, vol. 63, no. 12, pp. 5456-5464, Dec. 2015.

[9] J. C. Coetzee and Y. Yu, "New modal feed network for a compact monopole array with isolated ports," *IEEE Trans. Antennas Propag.*, vol. 56, no. 12, pp. 3872-3875, Dec. 2008.

[10] L. Zhao, L. K. Yeung, and K. L. Wu, "A coupled resonator decoupling network for two-element compact antenna arrays in mobile terminals," *IEEE Trans. Antennas Propag.*, vol. 62, no. 5, pp. 2767-2776, May 2014.

[11] S. N. Venkatasubramanian, L. Li, A. Lehtovuori, C. Icheln, and K. Haneda, "Impact of using resistive elements for wideband isolation improvement," *IEEE Trans. Antennas Propag.*, vol. 65, no. 1, pp. 52-62, Jan. 2017.

[12] H. Steyskal and J. S. Herd, "Mutual coupling compensation in small array antennas," *IEEE Trans. Antennas Propag.*, vol. 38, no. 12, pp. 1971-1975, Dec. 1990.

[13] H. H. Jenkins, *Small-Aperture Direction Finding*, Artech House., 1991.

[14] R. Zhou, H. Zhang, and H. Xin, "Improved two-antenna direction finding inspired by human ears," *IEEE Trans. Antennas Propag.*, vol. 59, no. 7, pp. 2691-2697, July 2011.

[15] N. Behdad, M. Al-Joumayly, and M. Li, "Biologically inspired electrically small antenna arrays with enhanced directional sensitivity," *IEEE Antennas Wireless Propag. Lett.*, vol. 10, pp. 361-364, 2011.

[16] A. R. Masoumi, Y. Yusuf, and N. Behdad, "Biomimetic antenna arrays based on the directional hearing mechanism of the parasitoid fly ormia ochracea," *IEEE Trans. Antennas Propag.*, vol. 61, no. 5, pp. 2500- 2510, May 2013.

[17] A. C. Mason, M. L. Oshinsky, and R. R. Hoy, "Hyperacute directional hearing in a microscale auditory system," *Nature*, vol. 410, no. 6829, pp. 686-690, Apr., 2001.

[18] R. N. Miles and R. R. Hoy, "The development of a biologically-inspired directional microphone for hearing aids," *Audiol. Neur.*, vol. 11, pp. 86-94, 2006.

[19] A. R. Masoumi and N. Behdad, "Architecture, design, and nonlinear optimization of three-element biomimetic antenna arrays," *IEEE Antennas Wireless Propag. Lett.*, no. 12, pp. 1416-1419, Dec. 2013.

[20] A. M. Elfrgani and R. G. Rojas, "Biomimetic antenna array using non-foster network to enhance directional sensitivity over broad frequency band," *IEEE Trans. Antennas Propag.*, vol. 64, no. 10, pp. 4297-4305, Oct. 2016.

[21] A. R. Masoumi, K. Ghaemi, and N. Behdad, "A two-element biomimetic antenna array with enhanced angular resolution and optimized power extraction," *IEEE Trans. Antennas Propag.*, vol. 63, no. 3, pp. 1059-1066, March 2015.

[22] I. Claesson and S. Nordholm, "A spatial filtering approach to robust adaptive beaming," *IEEE Trans. Antennas Propag.*, vol. 40, no. 9, pp. 1093-1096, Sep. 1992.

[23] X. H. Wu, A. A. Kishk and A. W. Glisson, "Antenna effects on a monostatic MIMO radar for direction estimation, a Cramer-Rao lower bound analysis," *IEEE Trans. Antennas Propag.*, vol. 59, no. 6, pp. 2388-2395, June 2011.

[24] B. Yanakiev, J. O. Nielsen, M. Christensen, and G. F. Pedersen, "On small terminal antenna correlation and impact on MIMO channel capacity," *IEEE Trans. Antennas Propag.*, vol. 60, no. 2, pp. 689-699, Feb. 2012.

[25] I. Szini, A. Tatomirescu, and G. F. Pedersen, "On small terminal MIMO antennas, harmonizing characteristic modes with ground plane geometry," *IEEE Trans. Antennas Propag.*, vol. 63, no. 4, pp. 1487-1497, Apr. 2015.

[26] Y. Zhou, R. S. Adve and S. V. Hum, "Design and evaluation of pattern reconfigurable antennas for MIMO applications," *IEEE Trans. Antennas Propag.*, vol. 62, no. 3, pp. 1084-1092, March 2014.

[27] M. L. Morris, M. A. Jensen, and J. W. Wallace, "Superdirectivity in MIMO systems," *IEEE Trans. Antennas Propag.*, vol. 53, no. 9, pp. 2850-2857, Sep. 2005.

[28] N. W. Bikhazi and M. A. Jensen, "The relationship between antenna loss and superdirectivity in MIMO systems," *IEEE Trans. on Wireless Communications.*, vol. 6, no. 5, pp. 1796-1802, May 2007.

[29] A. S. Y. Poon and D. N. C. Tse, "Does superdirectivity increase the degrees of freedom in wireless channels?," 2015 *IEEE International Symposium on Information Theory (ISIT)*, Hong Kong, 2015, pp. 1232-1236.

[30] T. I. Lee and Y. E. Wang, "Mode-based information channels in closely coupled dipole pairs," *IEEE Trans. Antennas Propag.*, vol. 56, no. 12, pp. 3804-3811, Dec. 2008.

[31] L. K. Yeung and Y. E. Wang, "Mode-based beamforming arrays for miniaturized platforms," *IEEE Trans. Antennas Propag.*, vol. 57, no. 1, pp. 45-52, Jan. 2009.

[32] C. Volmer, J. Weber, R. Stephan, K. Blau and M. A. Hein, "An eigen-analysis of compact antenna arrays and its application to port decoupling," *IEEE Trans. Antennas Propag.*, vol. 56, no. 2, pp. 360-370, Feb. 2008.

[33] R. P. Haviland, "Supergain antennas: possibilities and problems," *IEEE Antennas Propagat. Mag.*, vol. 37, no. 4, pp. 13-26, Aug. 1995.

[34] H. Steyskal and J. S. Herd, "Mutual coupling compensation in small array antennas," *IEEE Trans. Antennas Propag.*, vol. 38, no. 12, pp. 1971-1975, Dec. 1990.

[35] J. Andersen and H. Rasmussen, "Decoupling and descattering networks for antennas," *IEEE Trans. Antennas Propag.*, vol. 24, no. 6, pp. 841-846, Nov. 1976.

[36] S. C. Chen, Y. S. Wang and S. J. Chung, "A decoupling technique for increasing the port isolation between two strongly coupled antennas," *IEEE Trans. Antennas Propag.*, vol. 56, no. 12, pp. 3650-3658, Dec. 2008.

[37] J. C. Coetzee and Y. Yu, "Port decoupling for small arrays by means of an eigenmode feed network," *IEEE Trans. Antennas Propag.*, vol. 56, no. 6, pp. 1587-1593, Jun. 2008.

[38] B. K. Lau and J. B. Andersen, "Simple and efficient decoupling of compact arrays with parasitic scatterers," *IEEE Trans. Antennas Propag.*, vol. 60, no. 2, pp. 464-472, Feb. 2012.

[39] Y. Erhel, L. Bertel, and F. Marie, "HF radio direction finding operating on a heterogeneous array: Principles and experimental validation," *Radio Sci.*, vol. 84, no. 39, pp. 1003-1014, Feb. 2004.

[40] S. Hwang, S. Burintramart, T. K. Sarkar and S. R. Best, "Direction of arrival (DOA) estimation using electrically small tuned dipole antennas," *IEEE Trans. Antennas Propag.*, vol. 54, no. 11, pp. 3292-3301, Nov. 2006.

[41] O. G. Villard, G. H. Hagn and J. M. Lomasney, "Converting a small standard receiver into a hand-held narrow-aperture HF direction finder," *IEEE Antennas Propagat. Mag.*, vol. 36, no. 5, pp. 25-29, Oct. 1994.

[42] H. S. Lui and H. T. Hui, "Direction-of-Arrival estimation: measurement using compact antenna arrays under the influence of mutual coupling," *IEEE Antennas Propagat. Mag.*, vol. 57, no. 6, pp. 62-68, Dec. 2015.

[43] A. R. Masoumi and N. Behdad, "An improved architecture for twoelement biomimetic antenna arrays," *IEEE Trans. Antennas Propag.*, vol. 61, no. 12, pp. 6224-6228, Dec. 2013.

[44] P. Gruner, T. Chaloun and C. Waldschmidt, "Towards a mm-wave planar biomimetic antenna array with enhanced phase sensitivity," in *Proc. Eur. Conf. Antennas Propag.*, Davos, Switzerland, Apr. 2016, pp. 1-5.

[45] A. R. Masoumi, "Biologically-inspired, electrically small antenna arrays," Ph.D. dissertation, Dept. of Electrical and Computer Engineering, University of Wisconsin-Madison, Madison, WI, 2015.

[46] M. M. Jacob and D. F. Sievenpiper, "Gain and noise analysis of non-Foster matched antennas," *IEEE Trans. Antennas Propag.*, vol. 64, no. 12, pp. 4993-5004, Dec. 2016.

[47] https://product.tdk.com

[48] M. Akcakaya and A. Nehorai, "Biologically inspired coupled antenna beampattern design," *Bioinsp. Biomim.*, vol. 5, pp. 1-11, Dec. 2010.

[49] C. A. Balanis, *Antenna Theory: Analysis and Design*, 3rd ed. New York, NY, USA: Wiley, 2005.

[50] R. P. Haviland, "Supergain antennas: possibilities and problems," *IEEE Antennas Propagat. Mag.*, vol. 37, no. 4, pp. 13-26, Aug. 1995.

[51] J. Y. Deng, J. Li , and L. Guo, "Decoupling of a three-port MIMO antenna with different impedances using reactively loaded dummy elements," *IEEE Antennas Wireless Propag. Lett.*, vol. 17, no. 3, pp. 430-433, March 2018.

[52] J. Deng, J. Li, L. Zhao, and L. Guo, "A dual-band inverted-F MIMO antenna with enhanced isolation for WLAN applications," *IEEE Antennas Wireless Propag. Lett.*, vol. 16, pp. 2270-2273, June 2017.

[53] M. Ranjbar Nikkhah, K. Ghaemi, and N. Behdad, "A Three-element biomimetic antenna array with an electrically-small triangular lattice," *IEEE Trans. Antennas Propag.*, vol. 65, no. 8, pp. 4007-4016, August 2017.

[54] D. Kim, and S. Nam, "Systematic design of a multiport MIMO antenna with bilateral symmetry based on characteristic mode analysis," *IEEE Trans. Antennas Propag.*, vol. 66, no. 3, pp. 1076-1085, March 2018.

[55] D. M. Pozar, *Microwave Engineering*, 3nd ed. New York: Wiley, 2005.

[56] X. Tang, K. Mouthaan, and J. C. Coetzee, "Tunable decoupling and matching network for diversity enhancement of closely spaced antennas," *IEEE Antennas Wireless Propag. Lett.*, vol. 11, pp. 268-271, Feb. 2012.

[57] http://www.nebens.com/

[58] EEE 802.11-03/940r4: TGn Channel Models. IEEE. [Online]. Available: IEEE.

[59] P. J. Baldwin, A. G. P. Boswell, D. C. Brewster, and J. S. Allwright, "Iterative calculation of ship-borne HF antenna performance," *IEE Proc. H Microw. Antennas Propag.*, vol. 138, no. 2, pp. 151158, Apr. 1991.

[60] S. Best, "On the use of scale brass models in HF shipboard communication antenna design," *IEEE Antennas Propag. Mag.*, vol. 44, no. 2, pp. 1223, Apr. 2002.

[61] F. T. Dagefu, G. Verma, C. R. Rao, P. l. Yu, J. R. Fink, B. M. Sadler, and K. Sarbanaid, "Short-Range Low-VHF Channel Characterization in Cluttered Environments," *IEEE Trans Antennas Propag.*, vol. 63, no. 6, pp. 2719-2727, June 2015.

[62] F. T. Dagefu. J. Choi, M. Sheikhsofla, B. M. Sadler, and K. Sarabandi, "Performance assessment of lower VHF band for short-range communication and geolocation applications," *Radio Science*, vol. 50, no. 5, pp. 443-452, May 2015.

[63] H. Wheeler, "Fundamental limitations of small antennas," *Proc. IRE.*, vol. 35, no. 12, pp. 14791484, Dec. 1947.

[64] L. J. Chu, "Physical limitations of omni-directional antennas," *J. Appl. Phys.*, vol. 19, no. 12, pp. 11631175, Dec. 1948.

[65] B. A. Austin and K. P. Murray, "The application of characteristicmode techniques to vehicle-mounted NVIS antennas," *IEEE Antennas Propag. Mag.*, vol. 40, no. 1, pp. 721, Feb. 1998.

[66] Y. Chen, and C. Wang, "Electrically small UAV antenna design using characteristic modes," *IEEE Trans. Antennas Propag.*, vol. 62, no. 2, pp. 535-545, Feb. 2014.

[67] M. Ignatenko, and D. S. Filipovic, "On the design of vehicular electrically small antennas for NVIS communications," *IEEE Trans. Antennas Propag.*, vol. 64, no. 6, pp. 2136-2145, June 2016.

[68] N. Barani, J. F. Harvey, and K. Sarabandi, "Fragmented antenna realization using coupled small radiating elements," *IEEE Trans. Antennas Propag.*, vol. 66, no. 4, pp. 1725-1735, April 2018.

[69] G. Marrocco and L. Mattioni, "Naval structural antenna systems for broadband HF communications," *IEEE Trans. Antennas Propag.*, vol. 54, no. 4, pp. 1065-1073, Apr. 2006.

[70] Y. Chen, and C. Wang, "HF band shipboard antenna design using characteristic modes," *IEEE Trans. Antennas Propag.*, vol. 63, no. 3, pp. 1004-1013, March 2015.

[71] T. Shih, and N. Behdad, "Bandwidth enhancement of platform-mounted HF antennas using the characteristic mode theory," *IEEE Trans. Antennas Propag.*, vol. 64, no. 7, pp. 2136-2145, July 2016.

[72] R. Ma, T. Shih, R. Lian and N. Behdad, "Design of Bandwidth-Enhanced Platform-Mounted Electrically Small VHF Antennas Using the Characteristic-Mode Theory," *IEEE Antennas Wireless Propag. Lett.*, vol. 17, no. 12, pp. 2384-2388, Dec. 2018.

[73] F. A. Dicandia, S. Genovesi,and A. Monorchio, "Advantageous exploitation of characteristic modes analysis for the design of 3-D null-scanning antennas," *IEEE Trans. Antennas Propag.*, vol. 65, no. 8, pp. 3924-3934, Aug. 2017.

[74] M. Li, and N. Behdad, "Dual-band platform-mounted HF/VHF antenna design using the characteristic mode theory," *IET Microwaves Antennas Propag.*, vol. 12, no. 4, pp. 452-458, March 2018.

[75] F. A. Dicandia, S. Genovesi,and A. Monorchio, "Efficient excitation of characteristic modes for radiation pattern control by Using a novel balanced inductive coupling element," *IEEE Trans. Antennas Propag.*, vol. 66, no. 3, pp. 1102-1113, March 2018.

[76] F. A. Dicandia, S. Genovesi,and A. Monorchio, "Application of characteristic mode theory in HF band aircraft-integrated multi-antenna system designs," *IEEE Trans. Antennas Propag.*, vol. pp, no. n, pp. 1-10, Oct. 2018.

[77] R. Ma, and N. Behdad, "Design of Platform-Based HF Direction-Finding Antennas Using the Characteristic Mode Theory," *IEEE Trans. Antennas Propag.*, vol. 67, no. 3, pp. 1417-1427, March 2019.

[78] K. K. Kishor and S. V. Hum, "A two-port chassis-mode MIMO antenna," *IEEE Antennas Wireless Propag. Lett.*, vol. 12, pp. 690-693, Jun. 2013.

[79] K. K. Kishor and S. V. Hum, "A pattern reconfigurable chassis-mode MIMO antenna," *IEEE Trans. Antennas Propag.*, vol. 62, no. 6, pp. 3290-3298, Jun. 2014.

[80] J. Choi, F. T. Dagefu, B. M. Sadler, K. Sarabandi,"Low-Power Low-VHF Ad-Hoc Networking in Complex Environments," *IEEE Access*, vol. 5, pp. 24120 - 24127, Nov. 2017.

[81] J. Choi, C. R. Rao, and F. T. Dagefu, "Real-time Video Streaming at Low-VHF for Compact Autonomous Agents in Complex Scenes," *IEEE 89th Vehicular Technology Conference (VTC2019-Spring).*, pp. 1-5, Kuala Lumpur, Malaysia, April 2019.

[82] M. G. Pralon, G. D. Galdo, M. Landmann, M. A. Hein, and R. S. Thom, "Suitability of compact antenna arrays for direction-of-arrival estimation," *IEEE Trans. Antennas Propag.*, vol. 65, no. 12, pp. 7244-7256, Dec. 2017.

[83] M. Cabedo-Fabres, E. Antonino-Daviu, A. Valero-Nogueira, and M. F. Batalle, "The theory of characteristic modes revisited: A contribution to the design of antennas for modern applications," *IEEE Antennas Propag. Mag.*, vol. 49, no. 5, pp. 5268, Oct. 2007.

[84] http://www.fair-rite.com/67-material-data-sheet/

[85] N. Behdad and K. Sarabandi, "Bandwidth enhancement and further size reduction of a class of miniaturized slot antennas," *IEEE Trans. Antennas Propag.*, vol. 52, no. 8, pp. 19281935, 2004.

[86] International Telecommunication Union. (1992). Electrical characteristics of the surface of the Earth, Rec. ITU-R P.527-3.

[87] O. Buyukozturk, "Electromagnetic properties of concrete and their significance in non-destructive testing," *Transportation research record.*, vol. 1574, no. 1, pp.10-17, 1997.

[88] https://www.wrtest.com/

[89] H. A. Haus and W. Huang, "Coupled-mode theory," *Proc. IEEE.*, vol. 79, no. 10, pp. 1505-1518, 1991.

[90] T. Youndo, P. Jongmin, and N. Sangwook, "Mode-based analysis of resonant characteristics for near-field coupled small antennas," *IEEE Antennas Wireless Propag. Lett.*, vol. 8, pp. 1238-1241, Nov. 2009.

[91] F. Middelstaedt, S. V. Tkachenko, and R. Vick, "Natural frequencies of long symmetric multiconductor transmission lines," *IEEE Trans. Antennas Propag.*, vol. 67, no. 6, pp. 3881-3888, June 2019.

[92] M. Ranjbar-Nikkhah, M. A. Panahi, H. Luyen, H. Bahrami, and N. Behdad, "Capacity-enhancement in MIMO systems using biomimetic electrically small antenna arrays," *IET Microwaves, Antennas Propag.*, vol. 12, no. 13, pp. 2001-2006, July 2018.

[93] R. Ma and N. Behdad, "Design of platform-based HF direction-finding antennas using the characteristic mode theory," *IEEE Trans. Antennas Propag.*, vol. 67, no. 3, pp. 14171427, Mar. 2019.